DEVELOPMENT
OF
A PARYLENE BONDING BASED FABRICATION METHOD
FOR
MEMS GRAVIMETRIC RESONANT BASED MASS SENSORS

A THESIS SUBMITTED TO
THE GRADUATE SCHOOL OF NATURAL AND APPLIED SCIENCES
OF
MIDDLE EAST TECHNICAL UNIVERSITY

BY

FURKAN GÖKÇE

IN PARTIAL FULFILLMENT OF THE REQUIREMENTS
FOR
THE DEGREE OF MASTER OF SCIENCE
IN
ELECTRICAL AND ELECTRONICS ENGINEERING

SEPTEMBER 2017

Approval of the thesis:

**DEVELOPMENT
OF
A PARYLENE BONDING BASED FABRICATION METHOD
FOR
MEMS GRAVIMETRIC RESONANT BASED MASS SENSORS**

Submitted by **FURKAN GÖKÇE** in partial fulfillment of the requirements for the degree of **Master of Science in Electrical and Electronics Engineering, Middle East Technical University** by,

Prof. Dr. Gülbin Dural-Ünver
Director, **Graduate School of Natural and Applied Sciences** _____

Prof. Dr. Tolga Çiloğlu
Head of Department, **Electrical and Electronics Engineering** _____

Prof. Dr. Haluk Külah
Supervisor, **Electrical and Electronics Eng. Dept., METU** _____

Examining Committee Members:

Prof. Dr. Tayfun Akın
Electrical and Electronics Eng. Dept., METU _____

Prof. Dr. Haluk Külah
Electrical and Electronics Eng. Dept., METU _____

Asst. Prof. Dr. Kıvanç Azgın
Mechanical Eng. Dept., METU _____

Asst. Prof. Dr. Serdar Kocaman
Electrical and Electronics Eng. Dept., METU _____

Asst. Prof. Dr. Ender Yıldırım
Mechanical Eng. Dept. Çankaya University _____

Date: _____

I hereby declare that all information in this document has been obtained and presented in accordance with academic rules and ethical conduct. I also declare that, as required by these rules and conduct, I have fully cited and referenced all material and results that are not original to this work.

Name, Surname: Furkan, Gökçe

Signature: _____

ABSTRACT

DEVELOPMENT

OF

A PARYLENE BONDING BASED FABRICATION METHOD

FOR

MEMS GRAVIMETRIC RESONANT BASED MASS SENSORS

Gökçe, Furkan

M.Sc., Department of Electrical and Electronics Engineering

Supervisor: Prof. Dr. Haluk Külah

September 2017, 98 pages

This thesis reports development of a parylene bonding based fabrication method for MEMS gravimetric resonant based mass sensors that are integrated with microfluidics for real-time detection when there is a liquid flow through the microfluidic channels.

Parylene bonding has been optimized by conducting several bare bonding experiments. The optimized bonding takes place at 250ºC, in vacuum (1 mTorr) and with 2000 N of vertical piston force for 1 hour. The average shear bonding strength is 15.58 MPa for the optimized bonding recipe. Based on the optimized recipe, a novel method for fabricating lateral gravimetric resonators located on top of a microfluidic channel has been proposed.

A previous resonator design has been selected as benchmark, and has been fabricated using the method. The measurements show close agreement with the analytical and FEM results, proving the applicability of the fabrication method. The mass sensitivity of one of the fabricated resonators has been calculated as 5.89 pg/Hz. Attachment of a

μ-bead has caused a shift of 150 Hz in the resonance frequency. The mass of the attached μ-bead has been measured as 883.5 pg.

Liquid flow tests has shown that there is no liquid leakage neither around the bonding interface nor through the resonator gaps. However, the liquid inside the microfluidic channel has introduced additional feedthrough suppressing the sensing current of the sensor. The resonance characteristics when there is liquid inside the channel could not be extracted by using the differential characterization technique.

The models and experimental results prove the potential of the proposed fabrication method for fabricating gravimetric resonant based mass sensors and low temperature integration with microfluidics.

Keywords: Gravimetric Resonant Based Mass Sensor, Parylene Bonding, Lateral Resonator, Microfluidics Integration, Low Temperature Wafer Bonding

ÖZ

MEMS GRAVİMETRİK TINLAŞIM ESASLI KÜTLE ALGILAYICILARIN ÜRETİMİ İÇİN PARYLENE PUL BAĞLAMA YÖNTEMİNİ ESAS ALAN YENİ BİR ÜRETİM AKIŞININ GELİŞTİRİLMESİ

Gökçe, Furkan

Yüksek Lisans, Elektrik ve Elektronik Mühendisliği Bölümü

Tez Yöneticisi: Prof. Dr. Haluk Külah

Eylül 2017, 98 sayfa

Bu tez, mikroakışkan kanallarda sıvı akışı varken, gerçek zamanlı saptama için mikro-akışkanlarla bütünleşmiş MEMS gravimetrik tınlaşım esaslı kütle algılayıcılar için parylene ara tabakaların termal olarak bağlanmasını esas alan yeni bir üretim yönteminin geliştirilmesini bildirmektedir.

Parylene pul bağlama yöntemi, işlem görmemiş boş silisyum ve camlarla, çeşitli bağlanma deneyleri yapılarak optimize edilmiştir. Optimize edilmiş bağlanma 250ºC sıcaklıkta, vakum ortamında (1 mTorr) ve 1 saat boyunca 2000 N dikey piston kuvveti uygulanarak gerçekleşir. Optimum yapışma reçetesi için ortalama yanal dayanımı gücü 15,58 MPa olarak ölçülmüştür. Optimize edilmiş reçeteye dayanarak, gravimetrik kütle algılayıcıları için yeni bir fabrikasyon yöntem önerilmiştir.

Bir önceki rezonatör tasarımı esas alınmış ve sunulan yöntem kullanılarak imal edilmiştir. Ölçümler ve testler, analitik hesaplar ve FEM sonuçları ile iyi bir uyum gösterir; imalat yönteminin uygulanabilirliğini kanıtlar. Üretilen rezonatörlerden birinin kütle duyarlılığı 5,89 pg / Hz olarak hesaplanmıştır. Bir µ-boncuğun tutunması,

tınlaşım frekansında 150 Hz bir kaymaya neden olmuştur. μ-boncuk kütlesi 883,5 pg olarak ölçülmüştür.

Sıvı akış testleri, ne bağlama ara yüzeyinde ne de rezonatör boşluklarında herhangi bir sıvı sızıntısı olmadığını göstermiştir. Bununla birlikte, mikroakışkan kanal içindeki sıvı, algılayıcının çıkış akımını bastırarak ek kaçak akımına neden olmuştur. Bu yüzden, kanalın içinde sıvı bulunduğunda tınlaşım özellikleri (çıkış akımı) diferansiyel karakterizasyon tekniği kullanılarak çıkarılamamıştır.

Modeller ve deney sonuçları gravimetrik tınlaşım esaslı kütle algılayıcıların imalatı için önerilen yöntemin potansiyelini ve mikro akışkanlarla düşük sıcaklıkta bütünleşik sistemlerin üretiminin kolaylığını kanıtlamaktadır.

Anahtar Sözcükler: Gravimetrik Tınlaşım Bazlı Kütle Algılayıcı, Parylene Pul Bağlama Yöntemi, Yanal Rezonatör, Mikroakışkan Entegrasyonu, Düşük Sıcaklıkta Pul Bağlama

To my parents...

ACKNOWLEDGEMENTS

TABLE OF CONTENTS

LIST OF TABLES

LIST OF FIGURES

CHAPTER 1

INTRODUCTION

The diameter of the observable universe is 93 billion light-years, which is equal to 8.8×10^{26} meters [1, Ch. 2]. The average diameter of the Earth is 12742 kilometers [2]. The tallest man living is 251 centimeters tall [3]. A red blood cell has an approximate diameter of 6 micrometers [4, Pt. 2]. The smallest physical length which is called the Planck length is equal to 1.616×10^{-35} meters [5]. By comparing these lengths, it is obvious how precisely Richard Feynman was right saying "I… a universe of atoms, and atom in the universe." There *really* is plenty of room at the bottom [6]. *Mr. Feynman was not joking.*

Thoughts like his have been inspiring many people, both scientists and artists. The desire to discover the rooms at the bottom has led to the research activities in microscopy, microelectronics and microfabrication. Micro electromechanical systems (MEMS) is one of the fruits of these activities, combining microelectronics with mechanical devices.

Today, MEMS devices are available in the market having an expected value of 25+ billion US dollars in 2022 [7]. Commercial applications of MEMS include inkjet printers, accelerometer and gyroscopes, displays, integrated photonic switches, microscale power harvesters, point-of-care biomedical diagnosis and analysis tools, and gas sensors; all for a variety of fields and industries.

BioMEMS is one of the application areas of MEMS, with a growing research interest and developing a dedicated literature and expertise during past decades. It includes all the systems developed with the microfabrication technologies, which are used for analysis, diagnosis, manipulation, stimulation or transportation of biological and chemical subjects. Miniaturization in microelectronics (and micromechanics) and

microscopy in biomedicine have been developing in parallel from the beginning. Although they have huge differences between, as explained in [8, Ch. 1], miniaturization in biomedical devices connects the two and provides various benefits as shown in Figure 1.1:

- The smaller the devices become, the better the detection capabilities get. The response and recovery times become faster, and the power efficiency increases as the devices get smaller. The need for reagents (for analysis or diagnosis) also decreases with the size, which has additional advantages.

- With miniaturization, fabrication of similar small devices in large numbers for a similar price as one unit is possible. The fabrication cost per unit decreases significantly in parallel as in microelectronics. In addition to the fabrication costs, the operation and maintenance costs drop. Automation of fabrication is possible with microfabrication technologies as in IC fabrication.

- It is possible to predict the performance and behavior of MEMS devices even before the fabrication thanks to computational methods and quantitative design. Liquids flow in microfluidic channels in a deterministic way, for example. The movement of particles and forces between the particles with the devices (such as damping, fluid-structure interaction, Van der Waals forces) can be simulated and estimated both in frequency domain and in time domain.

Cell detection is one of the hottest research subjects of medicine and biology. Separating and detecting a *single* cell among millions promises diagnosis of diseases like cancer and HIV. Although there are several macroscale tools for diagnosis and analysis such as flow cytometry, some of these tools have been implemented using BioMEMS, with increased detectivity, mobility, and decrease in fabrication and operation costs. This technology is known as microscale rare cell detection.

This thesis reports a microscale rare cell detection system based on gravimetric resonant based mass sensors, in order to capture and count circulating tumor cells (CTCs) from an enriched blood sample. A novel fabrication method has been developed and is presented for the lateral resonators that have been used for similar

2

applications. The aim is to solve previously encountered problems mostly related to specific fabrication steps and due to high damping effects of the flowing liquid inside a microfluidic channel, under the lateral resonators. The ultimate goal is to propose a device that can selectively capture CTCs from the flowing fluid, and weigh and count them in real time for fast and easy diagnosis of cancer in its metastasis phase.
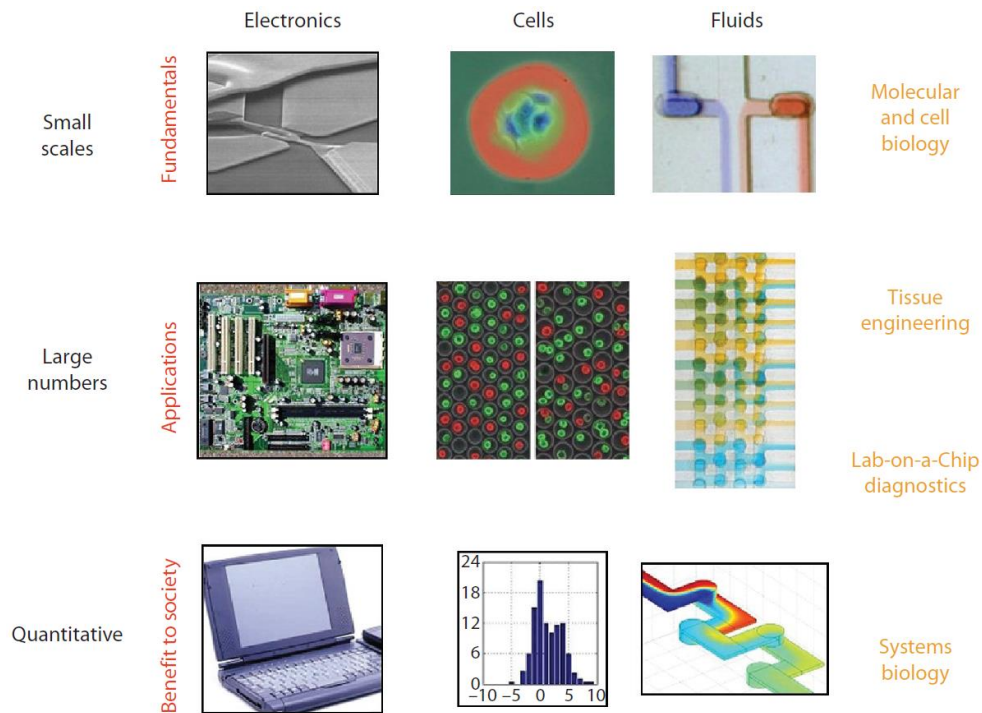
Figure 1.1 Benefits of microfabrication [8].

This chapter summarizes the important background information with a number of examples from the literature on the cell detection techniques. Importance of cell detection is explained in Section 1.1 with the relevant data on metastasis and CTCs. Macroscale and microscale detection techniques are briefly discussed in Section 1.2. Gravimetric detection is examined in detail in Section 1.3 with examples from the literature. Finally, research objectives and thesis organization are given in Section 1.4.

1.1. Importance of Cell Detection

Cancer is abnormal tumor growth with the potential of invasion and spread to other tissues of the body [9]–[12]. It is challenging to diagnose cancer at early stages, as it stays asymptomatic. In addition, in advanced stages, treatment is difficult or not

possible because the tumor grows and spreads in various organs and tissues. Metastasis is the invasion and spread of cancer, which occurs when CTCs detached from a solid tumor enter the peripheral blood system and causes tumor growth when they immobilize in other tissues [9], [13]. It is responsible for more than 90% of cancer-related deaths, and early detection of CTCs could save thousands of patients [11]. A schematic representation of metastasis is shown in Figure 1.2.
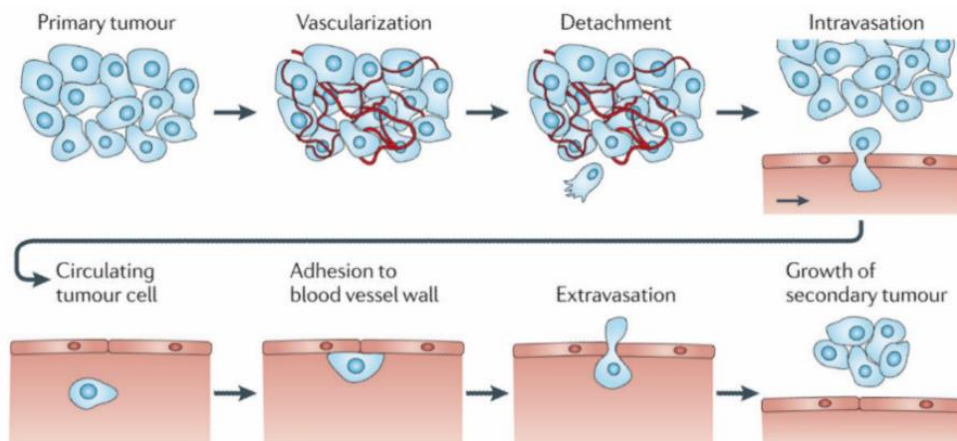
Figure 1.2 The metastatic process starting from the primary tumor to growth of secondary tumor [12].

CTCs circulate in the peripheral blood system, and after adhesion to and extravasation from blood vessel wall; they cause a new tumor growth [12]. Although they exist in the peripheral system even in early stages of cancer, because of their rarity in number, it is very difficult to detect them and diagnose metastasis. To give an idea, there exists 5-50 CTCs in a teaspoon of blood in early stages of cancer [9]. Detection of CTCs not only can prevent further worsening in patients' conditions but also can help us develop suitable medical treatment. They reveal disease condition, insights on stage of cancer and treatment predictions for specific types of cancer.

1.2. Cell Detection Systems

Detection of CTCs has extensively being studied because of the information they carry. However, no efficient means of isolation or detection have been reported yet. There are density based, antibody based, size based methods, microfluidics approaches and other techniques for isolation and analysis of CTCs [9]. Some of these detection techniques are discussed in this section.

1.2.1. Conventional Systems

Conventional detection techniques are based on a number of methods such as biological markers and protocols specifically activated for target cells. The most widely used ones include flow cytometry, fluorescence microscopy, and immunologic techniques [14].

Flow cytometry is based on the measurements of cell parameters using a laser light focused on a fluidic channel in which the cells flow [15]. It uses detectors and a processing unit (electronics and computer system) to track the intensities of scattered light in different wavelengths and outputs a spectrum response. The forward transmission provides information about the cell size, and the scattered light gives insight on surface structure of cells and internal complexity [14]. Fluorescence data can also be tracked and processed if the target cells are marked with fluorescent proteins. The structure of a flow cytometer system is given in Figure 1.3. It is the most powerful and efficient technique in cell detection; however, it is not only bulky and expensive but also requires human operation.
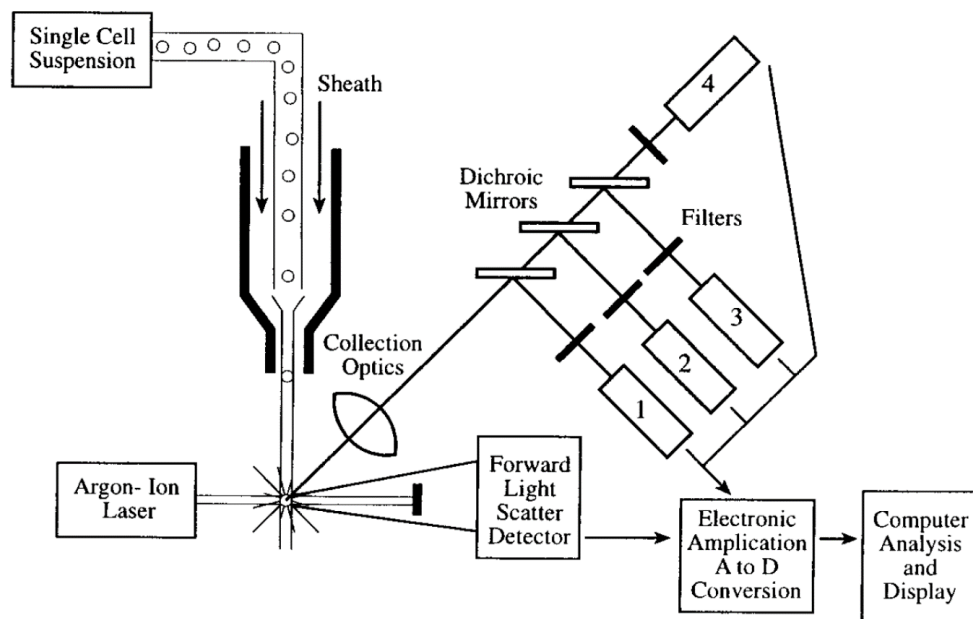
Figure 1.3 Schematic of flow cytometry [15]. The scattering from the hydrodynamic focused single cell suspension is collected by detectors, processed and analyzed by a computer.

Luminescence detection is commonly used, as it is selective and easy to practice. Luminescence is the emission of light without any heat stimulation and has the forms

of bioluminescence, chemiluminescence and fluorescence [16]. Both for luminescence detection and for fluorescence microscopy, fluorophores (or luminescent atoms) are excited to higher energy states and then relaxed. During relaxation, they return to the lower states by emitting photons at specific wavelengths (that are dependent on the type of fluorophore). For fluorescence, the exciting mechanism is the absorption of photon. Because the energy release during the relaxation is less than that of the excitation, the excitation light and the emitted light have different spectra. On the other hand, a chemical reaction can excite chemiluminescence or bioluminescence (if it takes place inside a living organism). By using selective fluorescence markers and certain filters for excitation and emission in microscopes, the target cells can be imaged and then be further analyzed [17].

Immunologic techniques make use of the surface markers on the cells such as antigens on the membranes of CTCs [9], [14]. Antibodies are used for selective binding with the antigens as different antibodies match with different antigens. The bond between them is distinct and detectable among millions of possible combinations. A marker such as a fluorescent protein or colorizing enzyme is chained with the antibody for detection of the cells. If the marker is a magnetic particle, then the technique is called immunomagnetic [9]. Figure 1.4 represents the bond between an antigen on the cell and an antibody with a marker chained with it. A widely available example is enzyme-linked immunosorbent assay (ELISA) where a sandwiched attachment protocol is used [18]. An example of one of the mostly used markers for CTCs is epithelial cell adhesion molecule (EpCAM) [19]. Immunologic techniques are also used as immobilization protocols in several microscale mechanical and optical detection systems.
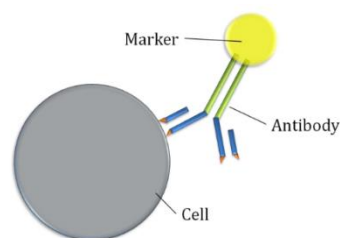
Figure 1.4 Representation of immunologic (or immunomagnetic) binding where the marker is bound to cell via an antibody [14].

Although the conventional methods provide relevant on rare cells data both quantitative and qualitative, they mostly involve labeling of the cells, which requires preliminary processing. The immunologic protocols must be known and applicable to label the cells, which is usually not the case. Moreover, most of these techniques require bulky and expensive processing and analysis tools such as optics and computers, requiring an educated person or complex automated controllers for operation and maintenance.
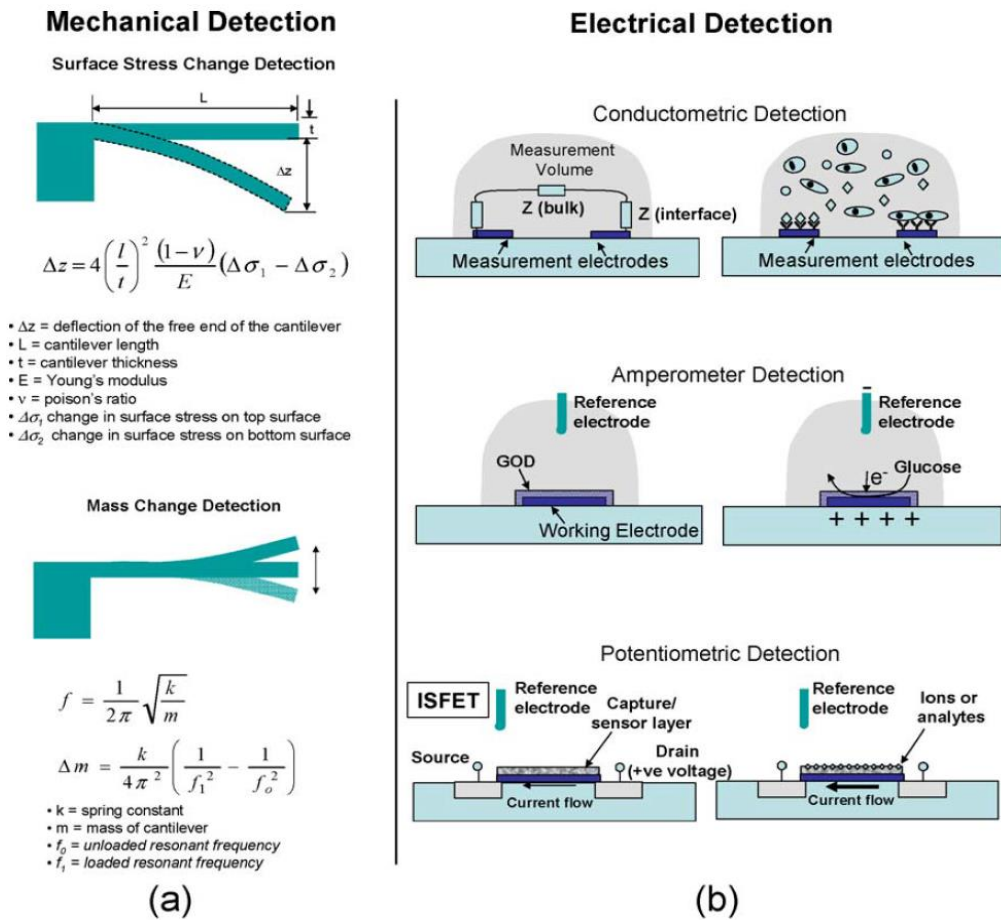
Figure 1.5 Some of the (a) mechanical and (b) electrical microscale detection modalities used in bioMEMS and biochip sensors [20]. Mechanical detection can be based on surface stress change detection (as in piezoelectric systems) or on mass change detection (as in gravimetric systems).

On the other hand, microfabrication techniques combined with interface electronics offer cheap, fast and efficient solutions for cell separation and detection. There have been a number of reported cell detection and separation systems, which constitute optical, mechanical, electrical, magnetic and chemical techniques. Some of these techniques are explained in Section 1.2.2 with application examples from the literature.

7

1.2.2. Microscale Systems

Microscale detection systems have some advantages when compared with the conventional and macroscale detection systems. They can be summarized as decreased reagent consumption, enhanced sensitivity, faster analysis, point-of-care operation, portability, in-vivo or in-vitro detection and biocompatibility [17, Ch. 7], [20]. The microscale systems can be categorized under three main titles: Optical, electrical (electrochemical) and mechanical. Small sensor size means smaller sample volumes and this decreases the number of the target cells to detect in the volume [8, Ch. 1]. This makes the cell detection even more challenging in microscale systems. However, there are various studies in the literature, showing the possibility and applicability of the techniques. Some of the key detection modalities that are widely utilized in bioMEMS and biochip sensors are illustrated in Figure 1.5. Note that, it is even possible to combine these modalities to develop detectors that are more sensitive.

a) Optical Microscale Cell Detection

As in the conventional systems, optical properties can also be detected with microscale units. Reflectance, transmission, fluorescence and/or absorption are identified with microscale optical detectors or lens-less portable microscopes. In addition, label-free detection schemes can also be possible with micro-optical systems. Because the size is reduced, the effects of ambient noise reduce and the sensitivity gets better in microscale optics. Furthermore, expensive and bulky optical equipment such as lenses and polarizers can be eliminated. This also removes the optical alignment problem.
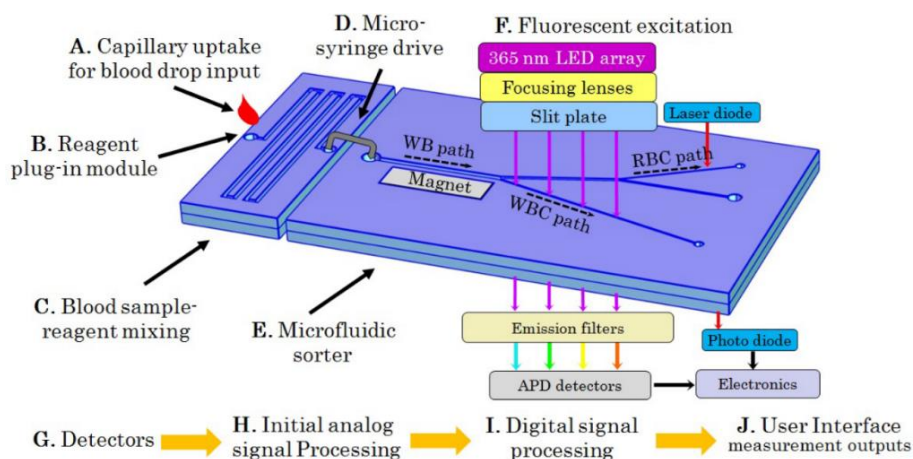
Figure 1.6 Schematic of the handheld flow cytometer with explanations of the subcomponents and processes (A-J) establishing an integrated micro total analysis system [21].

As an example of miniaturization of the conventional systems, a flow cytometric and spectroscopic cell counting system; i.e. a handheld flow cytometer, has recently been reported in the literature [21]. Avalanche breakdown photodiodes are utilized to detect fluorescently labelled target cells in the system with integrated microfluidics and magnetophoresis for separation of target cells from whole blood. In the output channel, the labelled and separated cells are counted on-chip by using the diodes. Figure 1.6 shows the subcomponents and processes of the designed handheld on-chip flow cytometer.

Labelled and label free detection of the target cells are also possible with high-resolution imaging techniques [22]. Direct counting requires no preliminary preparations as labelling or curing through post-processing may be necessary in some cases. Shadow imaging, holography or refraction can be used to get the images. Because of diffraction limit, which is a physical limit for resolving two neighboring objects at a minimum distance, reconstruction is needed. Lens-less imaging reduces the cost and accelerates the analyses.
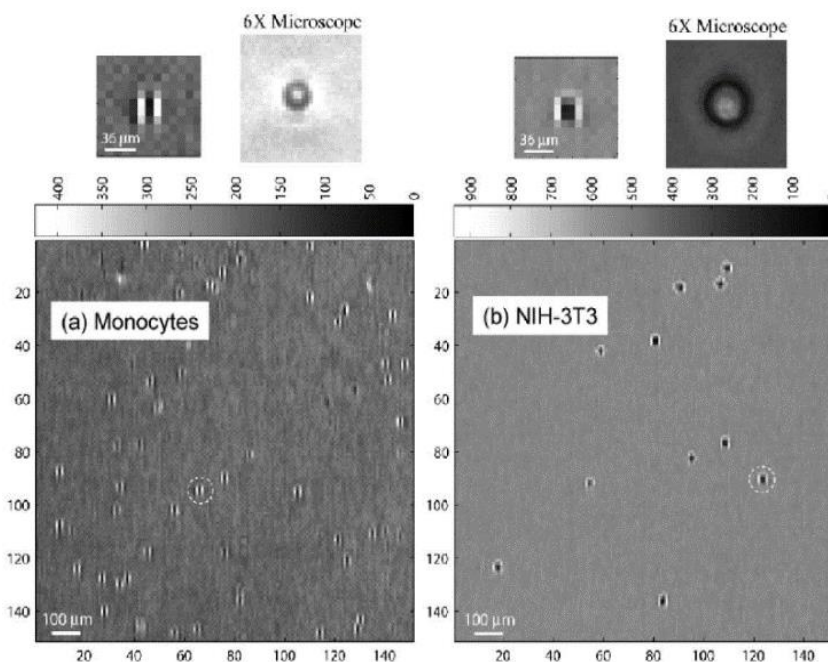
Figure 1.7 LUCAS images for (a) monocytes and (b) NIH-3T3 fibroblasts. The comparison between the captured images and the conventional microscope images are given for each cell type [23].

A lens-less cell detection system named LUCAS (lens-less, ultra-wide-field cell monitoring array platform based on shadow imaging) which utilizes a sensor array to

track and quantify the target cell [20], [23]. Monocytes, fibroblasts and red blood cells (RBCs) were imaged using the constructed detector and quantification was completed with a computer aided automated processing unit. The captured images with the constructed model is shown in Figure 1.7 with the comparison with a conventional low-NA microscope system.

b) Electrical and Electrochemical Microscale Cell Detection

Electrical and electrochemical detection are preferred because of their ease of application [14]. Impedance change can be directly measuring from phase or amplitude responses, conductivity, current, capacitance change, etc. The electrical and dielectric properties of target cell itself may be used for implementation of separation or detection as in electrophoresis, dielectrophoresis or magnetophoresis.

Amperometric sensors track the change in electrical current while potentiometric sensors track the change in electrical potential [17, Ch. 7], [20]. The ones tracking the conductivity change are conductometric [20]. All three kind of sensors are sensitive to ion concentration changes in electrochemical detection techniques. A well-known example of electrical cell detecting is the Coulter counter named after Wallace H. Coulter, which uses two parallel electrodes inside two electrolyte-filled chamber [24]. If a cell passes from a narrow aperture between the chambers, the impedance between the Coulter counter's electrodes changes and the cells are quantified.

It is even possible to utilize well-known electrical encoding/decoding protocols for real-time multi detection and analysis of the target cells. A code-division multiplexed resistive cell detector has recently been reported in the literature where the researchers combined the electrical cell detection techniques with a telecommunications approach [25]. Micromachined resistive electrodes with distinct code sequences are employed under several microfluidic channels. Once a cell passes from one of the channel, it creates a distinguishable signal in the output. If several cells pass from different channels at the same time, as each channel has distinct output waveforms, it is possible to solve and decode the superposed output signal with the known channel codes. The schematic of a 4-channel cell detector utilizing the discussed method is shown in Figure 1.8.
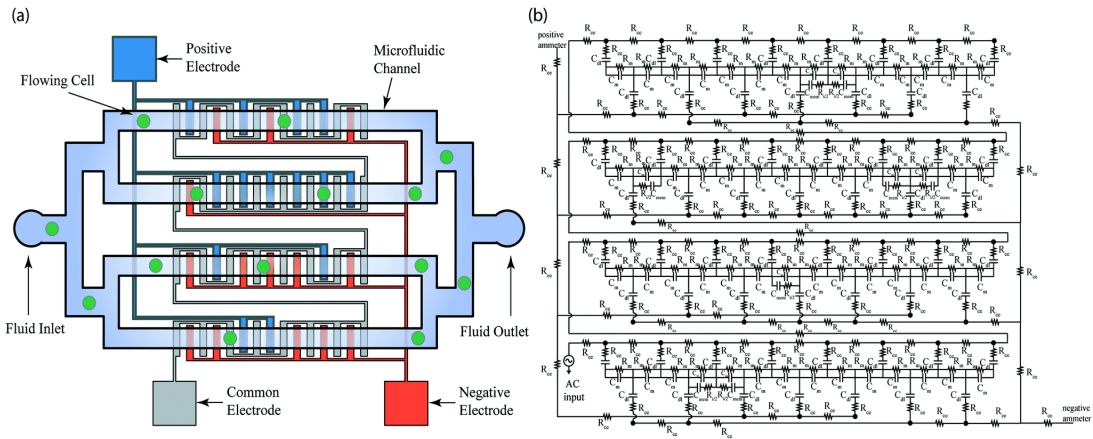
Figure 1.8 (a) A schematic and (b) corresponding equivalent circuit model of the proposed code-division multiplexed resistive pulse sensor for a hypothetical case when 5 cells are detected meanwhile [25].

c) *Mechanical Microscale Cell Detection*

For mechanical cell detection, either mechanical cell properties such as size and elasticity or micromachined mechanical micro devices such as resonators can be employed. CTCs are typically bigger in size compared to other blood cells [9]. This characteristic can be used even with very small sample volumes as all the sample is filtered out using a size based mechanical filter. The filter is designed such that all the cells other than CTCs can pass through them. In the end, all the trapped CTCs can be collected and further analyzed.
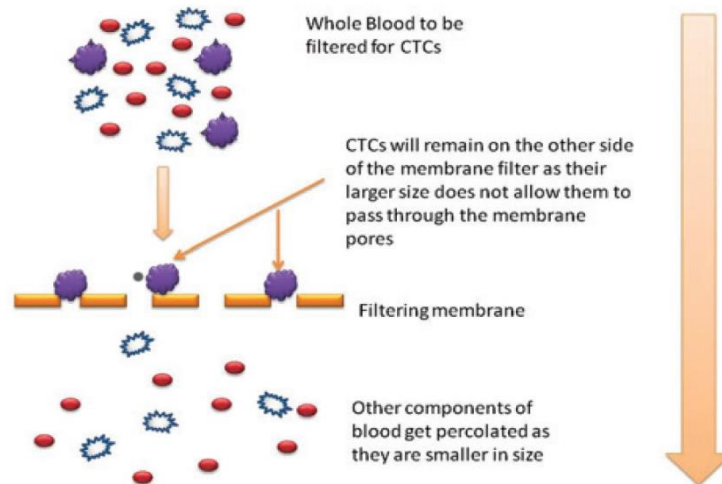
Figure 1.9 Separation of CTCs from whole blood based on their sizes using porous membranes [9].

The filtering mechanism is illustrated in Figure 1.9. ISET (isolation by size of epithelial tumor cells) is an assay based on the size difference and can detect the target

cells from blood samples as small as 1 ml [26]. Additional immunologic bio-activation protocols can be used to improve the filtering performance of such systems as in [27].

Gravimetric resonant based detectors are widely used to detect and quantify the target cells. Gravimetric detection is based on the change of resonating mass, which is manipulated with the target cell binding (or immobilization). Any attachment of additional mass on the resonating structure increases the total mass and induces a change in the resonance frequency. The amount of the change in the frequency is proportional with the total mass change. By using this information, it is possible to count the number of the captured (immobilized) cells. There are many reported gravimetric detectors utilizing cantilever type resonators [28], [29], suspended microchannel resonators [30] and lateral resonators [31]–[34]. Some of these gravimetric detectors are explained in Section 1.3.

In addition to the gravimetric detection, cantilever type resonators can also utilize the deflection information for cell detection [35]. With the addition of a mass (cell), the cantilever beam deflects. The amount of deflection (both the height and angle) is proportional with the number of cells attached. The mechanical characteristics of the cantilever beam are also affected with an attachment. In fact, this is the reason why the resonance frequency of cantilever beams changes with the attachment of target cells.

1.3. Gravimetric Resonant Based Detection

Gravimetric resonant based detection is based on the change of the resonance frequency as briefly discussed in the previous section. Attachment of target cells adds up to the total oscillating mass; thus, the resonance frequency decreases as it is inversely proportional with the mass. There are a number of examples in the literature, mostly employing cantilever type resonators due to their simplistic fabrication and operation schemes [28]–[30]. There are two main disadvantages of a cantilever type resonator [14]. First, because of their out-of-plane motion, the squeeze film damping decreases the quality factor in case of a liquid flow existence. Second, the frequency shift per attached cell depends on the location of the attachment on the cantilever beam. In other words, the mass sensitivity is not spatially uniform. Because of the damping

12

problems, some utilize a dip-dry method where the cells are attached on the cantilever during a liquid flow, and then the cantilever is dried. Then, the dry mass is measured and the target reagents are quantified. Despite the damping and linearity problems, there are some studies in the literature employing cantilever beams for in-liquid cell detection.

Suspended microchannel resonator (SMR) is a successful example of realization of cantilever type resonators for real time in fluid cell detection [30], [36], [37]. They fabricated a microfluidic channel in a hollow suspended cantilever beam, and operated the resonator in vacuum. The reported mass sensitivity was 0.85 attograms in 1 kHz bandwidth [37]. Optical actuation and sensing used to excite and track the SMRs. The major problem with this design is the channel size. It allows only small sized particles and cells. Furthermore, increasing the size harms the quality factor and sensitivity of the structure [38]. The suspended microchannel resonator and specific detection of bound species are illustrated in Figure 1.10.
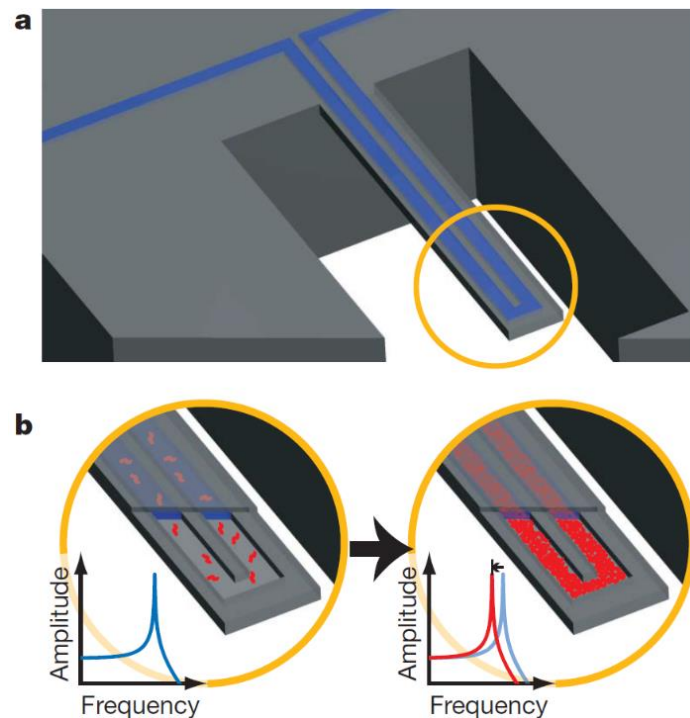
Figure 1.10 The illustration of (a) suspended microchannel and (b) specific detection of bound species [30].

In another study, a waterproof micro-diving suit has been utilized on a cantilever type resonator for in-liquid high-Q resonance detection [39]. The diving suit was realized

13

by using hydrophobic parylene thin film. It prevents liquid leakage to resonator gaps and decreases the damping effects. They measured a quality factor of 23 in water for more than 20 hours of operation in liquid. Figure 1.11 shows the micro-diving suit and the hydrophobic slit preventing the liquid leakage.
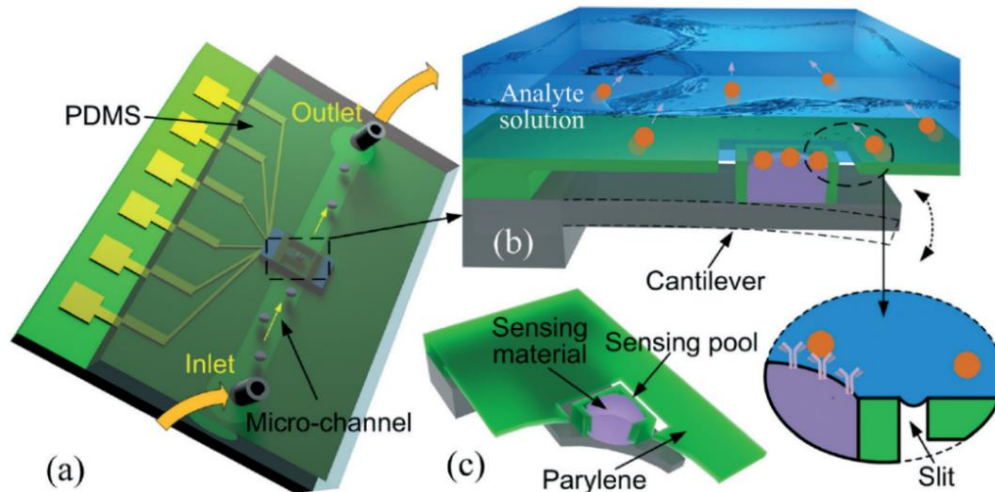
Figure 1.11 (a) Schematic of the proposed micro-diving suit on a cantilever type resonator. (b) and (c) cross section of the diving suite and parylene anti-leakage slit [39].

Compared to the cantilever type detection, lateral resonators promise spatially uniform mass sensitivity. In addition, the effect of squeeze film damping due to the liquid is decreased. Previously reported lateral gravimetric resonators have achieved a mass sensitivity of 5.91 fg/Hz after measuring the mass of a 3 µm diameter microbead [33]. Similar to the micro-diving suit, hydrophobic parylene thin film is used to prevent the liquid leakage to the resonator gaps. This anti-leakage gaps decreases the squeeze film damping significantly and enables in-liquid measurements [34].

The lateral resonators utilize electrostatic actuation and sensing even for in-liquid applications; hence, the cost is significantly reduced compared to optical sensing. They promise a linear mass sensitivity and integration with microfluidics. However, they have several design and characterization issues, making the real-time detection challenging. The quality factor is further reduced due to the capacitive talk between actuation and sensing electrodes. Existence of liquid in the microchannel can introduce additional crosstalk, which worsens the situation. Because there is a figure of merit while designing the resonators, to have an appropriate mass sensitivity, the gain reduces. With the crosstalk, this low gain prevents real-time detection [31], [38].

In this chapter, the importance of cell detection and several cell detection techniques (both macroscale and microscale) are introduced with examples from the literature. Some of the stated design and characterization issues can be solved by utilizing a novel fabrication method based on parylene intermediate layers, even without changing the resonator designs. As a proof of concept, the discussed lateral type resonator is studied in this thesis.

1.3.1. *Fabrication of Lateral Gravimetric Resonators*

Previous generations of the resonators studied in METU, BioMEMS Research Group had been fabricated by using anodic bonding. Ata Tuna Çiftlik was the first to propose a process flow for fabricating lateral gravimetric resonators integrated with microfluidics [14]. The proposed flow was complex, including anodic bonding steps.

In the earliest fabrication studies by Ekrem Bayraktar [40] and Deniz Eroğlu [41], the resonators were fabricated on a SOI and the microfluidic channels were structured by using PDMS. In those theses, In order to release the resonators, a recessed glass wafer was being *anodic bonded* to the structured SOI before dissolving the SOI's Si handle layer. Taylan Berkin Töral was the first to report a robust and high-yield fabrication of the resonators [42]. The microfluidics and recesses were etched on a glass wafer while the resonators were structured on a SOI wafer. Then the wafers were being *anodic bonded* to integrate the resonators with the microfluidics and complete the electrical signal routing. Finally, the SOI handle layer was being dissolved using dry etching methods (DRIE). The following studies by Mustafa Kangül [38] and Eren Aydın were also based on the fabrication method proposed by T.B. Töral with small modifications.

M. Kangül was the first researcher stating that *parylene bonding could be an alternative to anodic bonding* in the conclusion of his thesis as a future work [38]. The two main problems with the anodic bonding stated in his thesis are:

- Patterning and selective etching of the thin parylene layer is not possible because it is coated after the bonding step.

- Gravimetric detection system cannot be integrated with cell separation systems because anodic bonding is not suitable for fabrication of such systems.

1.3.2. Parylene Bonding

Parylene (poly-para-xylylene) is a biocompatible, chemically inert and hydrophobic polymer [43]. It is widely used in fabrication of biosensors as structural layer or protective coating. Parylene is a crystalline polymer and prevents any permanent bonding or attachment to any surface with its stable and inert nature [43], [44]. However, it becomes a soft and adhesive thermoplastic above its glass transition temperatures. This characteristic feature enables low temperature adhesive wafer bonding if parylene is coated as intermediate layers between the wafers to-be-bonded [43]–[49]. The hypothetical chain entanglements during parylene bonding are illustrated in Figure 1.12.

There are a number of types of parylene, including varieties C, N, F, D and AF-4. Each has different mechanical, chemical and physical properties [50]. Because it is conformal and it can be coated easily at the room temperature, parylene-C is studied throughout this thesis. Moreover, the examples in the literature also utilize parylene-C as the bonding polymer probably because of the same reasons.
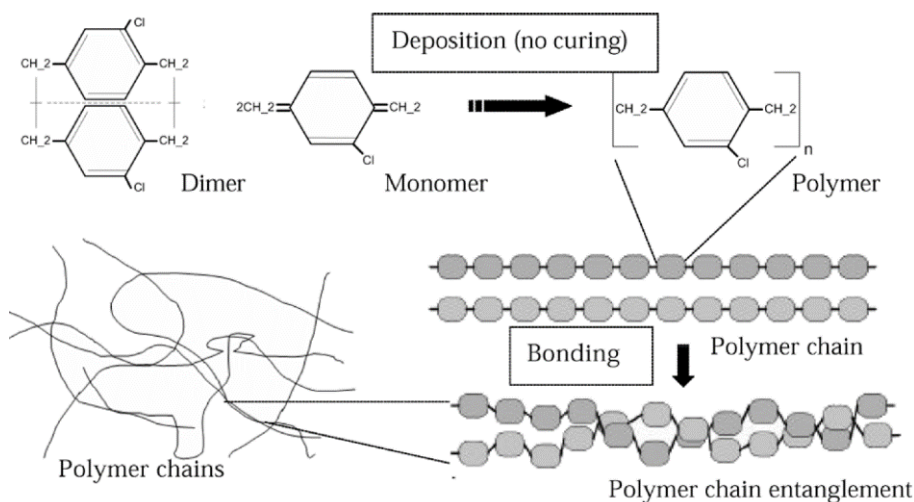
Figure 1.12 Hypothetical parylene chain re-entanglements of intermediate layers during a bonding [44].

There are several studies in the literature using parylene for its hydrophobicity [32], [34], [39], [51]. Coating resonators with a hydrophobic thin film significantly reduces the viscous damping due to liquids significantly and increases the performance. However, there is no reported lateral resonator, which can operate under a liquid flow. There are two cantilever based resonant detection systems reported in the literature for

real time detection. The first one employs a microfluidic channel inside a cantilever beam [30]. The other uses a parylene micro-diving suit to prevent liquid leakage through the resonator gaps [39]. Both sacrifices from the sensing area (volume). In order to decrease the damping effects and to increase the mass sensitivity, they had to design a small sensing area (volume). Previous researchers of METU BioMEMS Research Group had reported resonators for under-liquid-flow operation [32], [34]. Unfortunately, patterning and selective etching of the hydrophobic parylene coating is not possible because the sensing areas are located inside a microchannel as also stated in Section 1.3.1. In addition, there were no reported real time detection with those resonators.

Throughout this thesis, parylene bonding is studied as the fabrication method because it promises several advantages over anodic bonding as stated. The details of parylene bonding is explained in Chapter 4 with relevant examples and statistics from the literature. Dielectric characteristics of parylene are also studied as they can be affected by the phase change of the polymer during bonding. A novel fabrication method utilizing parylene bonding is proposed and several resonators are fabricated with the proposed method.

1.4. Research Objectives and Thesis Organization

The aim of this study is to solve the important design and characterization issues by using a fabrication method utilizing a parylene bonding. Therefore, the objectives are:

- Investigation of parylene thin film as an intermediate bonding layer

  - Replication of previously reported parylene bonding studies

  - Analysis of electrical and mechanical properties of parylene

- Integrating parylene bonding in the fabrication procedure of the resonators

- Fabricating the lateral resonators with the developed fabrication scheme

- Characterization of the parylene-bonded lateral resonators & mass sensing

This thesis is organized as follows:

Chapter 2 is dedicated to the theory of gravimetric detection and background information of the resonance characterization and feedthrough elimination. After a coarse discussion on resonance mechanics, capacitive actuation and sensing are introduced. The resonance frequency, the quality factor, the force acting on the oscillating mass and the output current are derived. Then, the feedthrough effect is explained and an equivalent electrical model including the feedthrough capacitance is presented. Damping effects acting on the lateral type resonators are briefly explained. Referring to the damping effects, mechanical noise is introduced and the theoretical mass sensitivity is calculated.

Chapter 3 is on designs and simulations of the lateral resonators studied. The previously reported designs (to-be-fabricated with parylene bonding) are explained in detail and the characteristics are calculated analytically and by using COMSOL Multiphysics.

Chapter 4 spreads out the details of fabrication of the lateral resonators. Previously used fabrication methods, with a detailed analysis on the last generation method, are presented with their advantages and disadvantages. The parylene thin film is investigated for the proposed fabrication method. Thermal and electrical properties of parylene are discussed with relevant data from literature and experimental results. Parylene bonding is introduced with previously reported examples from the literature. A novel method utilizing parylene bonding is proposed addressing all the advantageous characteristics of the technique.

In Chapter 5, all the fabricated devices are characterized in air using the characterization techniques studied in Chapter 2. Measured resonance characteristics and mass sensitivities are reported and compared. Problems encountered during characterization of the fabricated resonators are discussed and possible solutions are stated for future studies.

Finally, Chapter 6 concludes the thesis with an evaluation of the findings and possible future works related to this study.

CHAPTER 2

THEORY & BACKGROUND

As introduced in the first chapter, the main objective of this thesis is to develop a gravimetric resonant based mass sensor by eliminating the drawbacks of the previous generation fabrication techniques. Before going further into the fabrication, as lateral resonators are used throughout this study, it is better to analyze the theory of micro electromechanical resonators and gravimetric detection in detail. In addition, general characterization methods as well as the feedthrough current problem are revisited.

This chapter summarizes the general theory of the micro electromechanical resonators by discussing the mechanics of resonance and the characterization of the fabricated devices. Section 2.1 examines the basics of resonance mechanics, and capacitive actuation and sensing. In this section, the transfer function is derived with the aid of an equivalent electrical model. The damping and noise effects are introduced. Furthermore, the mass sensitivity of the system is discussed. Section 2.2 introduces the interface electronics and the fundamentals of self-oscillation. Moreover, the feedthrough current and its effects on the sensitivity is discussed in detail. Two different feedthrough current elimination techniques based on differential sensing and second harmonic characterization are also presented in this section. Finally, the chapter is summarized in Section 2.3.

2.1. Theory of Micro Electromechanical Resonators

A micro electromechanical resonator consists of a mechanical band-pass filter, electrical drive and sense, and a feedback mechanism. The mechanical filter is a single-degree-of-freedom damped oscillator, and can be modelled as a mass, spring and damper system [52, Ch. 1]. The mass is capacitively actuated by an AC voltage, and the motion is sensed capacitively at the sense port. In the open-loop operation, the

system is a band-pass filter [38]. In the closed-loop operation, when the conditions are satisfied, the output current and the mass oscillate at the mechanical resonant frequency unless an external distortion is applied. The transfer function of such a mechanical system can be derived with the aid of an equivalent electrical model. Including nonlinearity and damping effects, the noise and sensitivity can be calculated because the mechanical noise determines the limits of sensitivity and quality factor. Besides, damping decreases the quality factor. The following subsections discuss resonance mechanics, capacitive actuation and sensing, derivation of the transfer function, nonlinearity and damping effects, and noise and frequency resolution.

2.2.1. Resonance Mechanics

A micro electromechanical resonator can be modelled as an oscillator with a mass, m involving elastic and dissipative forces, which are a spring with stiffness, k and a dashpot with damping, b. The mass is also called proof mass. Figure 2.1 represents the single-degree-of-freedom oscillator model along with the displacement and force vectors.
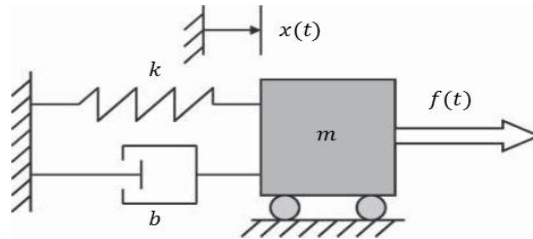
Figure 2.1 Schematic representation of the equivalent single-degree-of-freedom oscillator model [52].

In the constructed model, damping mechanisms cause energy dissipation. This results in a decrease in the quality factor of the oscillation and the detection sensitivity. Damping force is proportional to velocity of the mass. None of the mass, spring stiffness and the damping constant depends on time or on the oscillation frequency. Performing a force balance on the equivalent oscillator model:

$$m\ddot{x}(t) + b\dot{x}(t) + kx(t) = f(t) \tag{2-1}$$

where $x(t)$ is the displacement in meters, m is the mass of the oscillator in kg, k is the spring constant of the flexible folded beams in kg/s^2, b is the damping of the dashpot in kg/s, and $f(t)$ is the total force applied on the mass. The dot notation represents

20

differentiation with respect to time t. Both the force and the displacement are harmonics with the same frequencies; i.e. the solution of this second order differential equation is sinusoidal.

If there is no net force on the mass; i.e. $f(t) = 0$, the force balance become

$$m\ddot{x}(t) + b\dot{x}(t) + kx(t) = 0 \qquad (2\text{-}2)$$

from which the undamped natural frequency, ω_0 and the damping ratio, ξ are defined as

$$\omega_0 \triangleq \sqrt{\frac{k}{m}} \qquad (2\text{-}3)$$

$$\xi \triangleq \frac{b}{2\sqrt{km}} \qquad (2\text{-}4)$$

Because of the energy dissipation due to the damping mechanisms, the system oscillates at damped natural frequency, ω_d, which slightly differs from ω_0.

$$\omega_d = \omega_0\sqrt{1 - \xi^2} \qquad (2\text{-}5)$$

If ξ is larger than one, the oscillation frequency is imaginary, which means that the system is overdamped. In overdamped systems, the mass does not oscillate. Hence, the damping ratio should be less than one for proper operation of the resonators. Throughout this chapter, ξ is assumed less than one. The response of an underdamped system ($\xi < 1$) can be written as:

$$x(t) = e^{-\xi\omega_0 t}(\alpha cos\omega_d t + \beta sin\omega_d t) \qquad (2\text{-}6)$$

where α and β are constants and depend on the initial system conditions.

In order to find the transfer function of the system, Laplace transformation can be used. Transforming (2.1-1), the following relation is obtained:

$$H(s) = \frac{X(S)}{F(s)} = \frac{1}{ms^2 + bs + k} \qquad (2\text{-}7)$$

21

where $F(s)$ and $X(s)$ are the Laplace transformations of $f(t)$ and $x(t)$, respectively. $H(s)$ is the transfer function of the single-degree-of-freedom oscillating system relating force and displacement.

Quality factor, Q, is defined as the maximum gain of the transfer function; i.e. the maximum of its modulus, $|H(s)|$, can get. If the system is undamped with $\xi = 0$, then the quality factor is infinite. In practice, this is not the case because of energy dissipation. Damping determines the maximum gain over the whole frequency spectrum. Maximizing $|H(s)|$, resonant frequency where the maximum displacement occurs can be calculated as:

$$\omega_{res} = \omega_0\sqrt{1 - 2\xi^2} \tag{2-8}$$

The resonance frequency of the system is different (and less) than the undamped and damped natural frequencies. However, if Q is high, these differences can be ignored.

The quality factor measures the rate of energy dissipation with respect to the stored energy of the resonator. The higher it gets, the less the energy loss becomes. It can be defined as:

$$Q = \frac{1}{2\xi\sqrt{1 - \xi^2}} \tag{2-9}$$

If the damping ratio is sufficiently small, the damped resonant frequency can be assumed equal to the undamped natural frequency of the system. In this case, Q can be simplified:

$$Q \cong \frac{1}{2\xi} = \frac{\sqrt{km}}{b} \tag{2-10}$$

2.2.2. *Capacitive Actuation and Sensing*

For proper operation of the resonators, the proof mass is kept oscillating by means of an actuation force. The major mechanism of this actuation force is to excite the movable proof mass. The energy flows and the necessary vibration amplitudes are achieved due to the first excitation. During the operation, this actuation force compensates the energy loss caused by the damping mechanisms and guarantees

22

continuous oscillation. For the resonators proposed throughout this thesis, as it is cheaper and easy to integrate with the interface electronics, capacitive actuation is used.

In order to track the resonance, a sensing mechanism is needed. Similar to the actuation, capacitive means are also preferred for sensing. However, for both actuation and sensing, other options exist depending on the technological availability of the applications.

Capacitive sensing and actuation introduces several advantages for the application. First, as silicon is a conductive material, it works as a capacitive electrode itself. Second, both varying gap and varying overlap capacitances can easily be built in the resonator structures. Third, the flexible folded beam suspensions, which are the springs of the system, limit the direction of oscillation and eases the actuation and sensing mechanisms. Forth, the output current being capacitive makes it easier to sense the resonance.

Capacitance relates the potential difference to the charge stored. It depends on the geometry of the structure and the relative permittivity of the medium, ε_r. For a capacitive structure storing a charge $\pm q$ with a voltage V between them, the capacitance is equal to:

$$C = \frac{q}{V} \tag{2.1-11}$$

For a MEMS resonator, the capacitance is a parallel plate capacitor which has three degree-of-freedoms in x, y, and z directions. The schematic of such a capacitor is shown in Figure 2.2. The capacitance (with a small arbitrary displacement) can be written as:

$$C = \frac{\varepsilon_0 \varepsilon_r (y_0 + y)(z_0 + z)}{x_0 + x} \tag{2.1-12}$$

where $A = (y_0 + y)(z_0 + z)$ is the overlap area between the capacitive electrodes and ε_0 is the permittivity of vacuum.
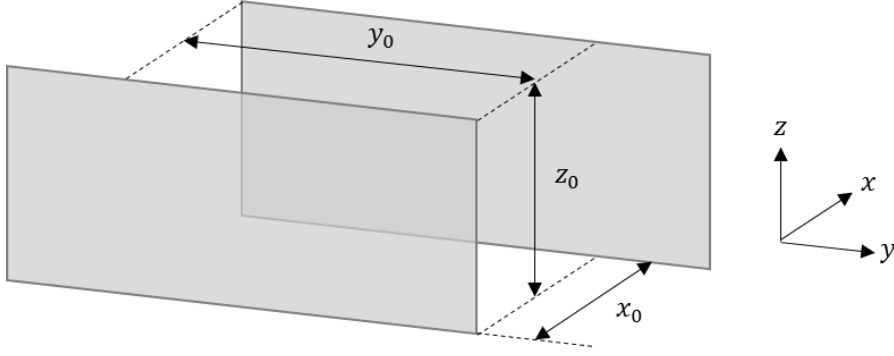
Figure 2.2 Two conducting plates forming a parallel plate capacitor, which is free to move in three orthogonal directions. Initial overlap area and gap distance is shown with $y_0 \cdot z_0$ and x_0 respectively.

Because the oscillation direction is limited in x direction for the lateral mode resonators, the movement in y and z directions are ignored for the derivation of the actuation force. The stored electrostatic energy is written as:

$$E = \frac{1}{2} C V^2 \qquad (2.1\text{-}13)$$

Force is the gradient of the stored energy:

$$F = |\nabla E| = \frac{\partial E}{\partial x} = \frac{1}{2} \frac{\partial C}{\partial x} V^2 \qquad (2.1\text{-}14)$$

Substituting $V = V_{DC} + v_{ac}\sin(\omega t)$ into Eq. (2.1-14), the actuation force takes the following form:

$$F(t) = \frac{1}{2}\frac{\partial C}{\partial x}\left[\left(V_{DC}{}^2 + \frac{v_{ac}{}^2}{2}\right) + 2V_{DC}v_{ac}\sin(\omega t) - v_{ac}{}^2\cos(2\omega t)\right] \qquad (2.1\text{-}15)$$

The AC term in the applied voltage introduces higher frequencies in the excitation motion as stated in Eq. (2.1-15). When $V_{DC} \gg v_{ac}$, the second harmonic term can be ignored. Notice that the resonator acts as a band-pass mechanical filter around the resonance frequency and eliminates higher frequency components. As a result, neglecting the higher order component, the actuation force written in Eq. (2.1-15) takes the form:

$$F(t) = \frac{1}{2}\frac{\partial C}{\partial x}\left[V_{DC}{}^2 + 2V_{DC}v_{ac}\sin(\omega t)\right] \qquad (2.1\text{-}16)$$

24

The lateral mode resonators discussed throughout this thesis have symmetrical and fixed (stationary) actuation and sensing electrodes on the axis of free oscillation. DC voltage is applied to the oscillating proof mass whereas AC voltage is applied to the stationary actuation electrode. Therefore, the force due to V_{DC}^2 is cancelled out. The net force on the suspended proof mass is:

$$F(t) = \frac{\partial C}{\partial x} V_{DC} v_{ac} \sin(\omega t) \qquad (2.1\text{-}17)$$

The transfer function relating the force and the applied voltage can be written as

$$F(s) = \frac{\partial C}{\partial x} V_{DC} V(s) \qquad (2.1\text{-}18)$$

where $V(s)$ is the Laplace transform of the AC voltage applied to the actuation electrode.

The actuation force is based on changing the stored energy on the capacitive electrodes. Because of the actuation, the suspended proof mass moves and the capacitance changes forcing the stored charge to flow through the sensing electrode. The current injection to the capacitor through the sensing electrode can be written as the rate of change of the change in the stored charge by differentiating Eq. (2.1-11):

$$I(t) = \frac{\partial q}{\partial t} = \frac{\partial C}{\partial t} V + C \frac{\partial V}{\partial t} \qquad (2.1\text{-}19)$$

If $V_{DC} \gg v_{ac}$, as in Eq. (2.1-16), the rate of change in the applied voltage can be ignored:

$$I(t) \cong \frac{\partial C}{\partial t} V_{DC} \qquad (2.1\text{-}20)$$

As the capacitance is a function of $x(t)$ for a lateral mode resonator, $\frac{\partial y}{\partial t} = \frac{\partial z}{\partial t} = 0$. Substituting $\frac{\partial C}{\partial t} = \frac{\partial C}{\partial x} \frac{\partial x}{\partial t}$ into Eq. (2.1-19), the sensing current takes the form:

$$I(t) \cong V_{DC} \frac{\partial C}{\partial x} \frac{\partial x}{\partial t} \qquad (2.1\text{-}21)$$

Laplace transform of the sensing current is as follows:

$$I(s) = \frac{\partial C}{\partial x} sX(s)V_{DC} \tag{2.1-22}$$

In summary, the applied actuation voltage changes the stored energy. The change in stored energy induces an initial movement to the suspended proof mass. The movement changes the capacitance and causes a flow of charges. This current is the output of the system.

The change in capacitance can be induced by two distinct methods: varying the overlap area and varying the gap distance. However, the proposed resonators induce the change by varying the gap distance, and it is sufficient to analyze the varying gap distance method.

For the proposed lateral mode resonators, the movement of the suspended proof mass is in the direction normal to the capacitive electrodes, changing the capacitive gap distance. Figure 2.3 represents the capacitance change schematically for the varying gap distance method. The rate of change of the capacitance with respect to x can be written as:

$$\frac{\partial C}{\partial x} = \frac{\partial \left(\varepsilon_0 \varepsilon_r \frac{A}{x_0 - x} \right)}{\partial x} = -\varepsilon_0 \varepsilon_r \frac{A}{(x_0 - x)^2} \tag{2.1-23}$$
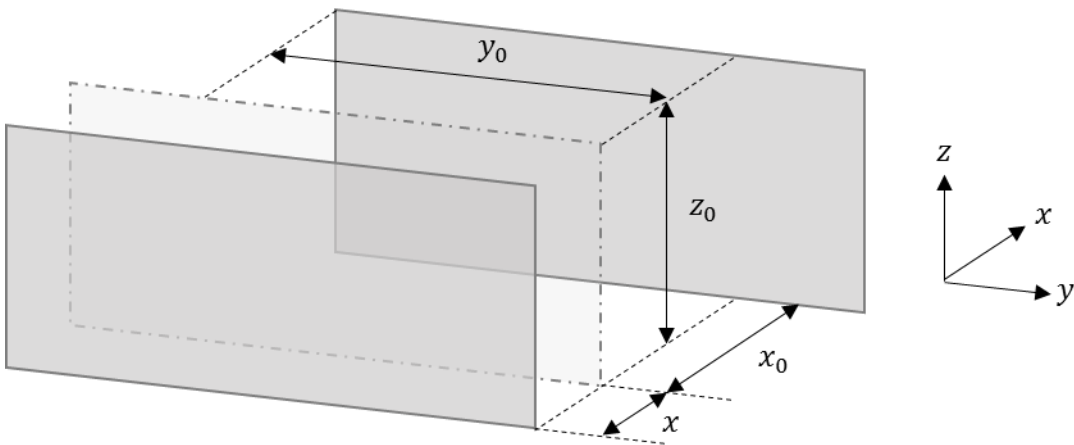
Figure 2.3 Schematic representation of change in the capacitance due to varying gap distance. The change in the gap distance is shown with x. The movement is one directional and only in x direction.

26

Overall transfer function of the system in Laplace domain ($H_\Sigma(s)$) can be written as:

$$H_\Sigma(s) = \frac{I(s)}{V(s)} = \frac{X(s)}{F(s)}\frac{F(s)}{V(s)}\frac{I(s)}{X(s)} = \frac{s\left(\frac{\partial c}{\partial x}V_{DC}\right)^2}{ms^2 + bs + k} \qquad (2.1\text{-}24)$$

As seen in Eq. (2.1-22), the system has two poles and a zero, implying that it has a band-passing nature as previously stated. Moreover, the gain is a function of the applied DC voltage and the rate of change of the capacitance.

Although the resonator is modelled as a single-degree-of-freedom oscillating mass, there may also exist out-of-plane oscillations. The movements in y and z are strongly suppressed by the flexible folded beam suspensions as shown in Section 3 in detail. The out-of-plane motion in the z direction has different natural frequency and damping. Since the lateral resonance mode along x is actuated, the assumptions are still valid.

2.2.3. Feedthrough Current

Although the governing transfer function is derived assuming the actuation and sensing electrodes do not couple, there exist a capacitive coupling causing a leakage current. This leakage current, i.e. the feedthrough current, suppresses the high-pass characteristics of the output current stated in Eq. (2.1-22). The magnitude of the feedthrough current increases with the frequency as the capacitive impedance decreases. The leakage current in the fundamental frequency adds with the sensing current at the sensing electrode, which makes the characterization more difficult.

The direct coupling capacitance between the actuation and sense electrodes can be included in the overall transfer function to analyze its effects further in detail:

$$H_\Sigma^f(s) = \frac{s\left(\frac{\partial c}{\partial x}V_{DC}\right)^2}{ms^2 + bs + k} + sC_{ft} \qquad (2.1\text{-}25)$$

At the mechanical resonant frequency of the resonators, the imaginary feedthrough current suppresses the resonance peak in the magnitude response, and changes the phase change.

2.2.4. Equivalent Electrical Model

In order to reduce the problem into the electrical domain, it is reasonable to develop an equivalent electrical model of the oscillating system. The single-degree-of-freedom oscillating model shown in Figure 2.1 is mathematically identical to a second order electrical circuit composed of resistance, capacitance and inductances. Notice that while deriving the model, only the oscillation in the lateral x direction is considered. The model is linear, and does not capture the nonlinear behaviors such as second harmonic.

With a DC polarization voltage (to the proof mass) V_{DC}, and an AC actuation voltage (to the actuation electrode), v_{ac}, the corresponding linearized current and force equations are:

$$I \cong C_0 \frac{\partial(v_{ac}\sin(\omega t))}{\partial t} + V_{DC}\frac{\partial C}{\partial x}\frac{\partial x}{\partial t} \tag{2.1-26}$$

$$F \cong V_{DC}\frac{\partial C}{\partial x}v_{ac}\sin(\omega t) \tag{2.1-27}$$

where C_0 is the capacitance when $x = 0$. The equivalent electrical model is composed of an electromechanical transformer and a fix capacitor. The transformer ratio is:

$$\eta = V_{DC}\frac{\partial C}{\partial x} \tag{2.1-28}$$

The feedthrough capacitance is a result of the coupling between the actuation and sensing electrodes. Hence, it should be parallel to the resonator's equivalent electrical model. Figure 2.4 shows the equivalent electrical circuit for an oscillation towards x.
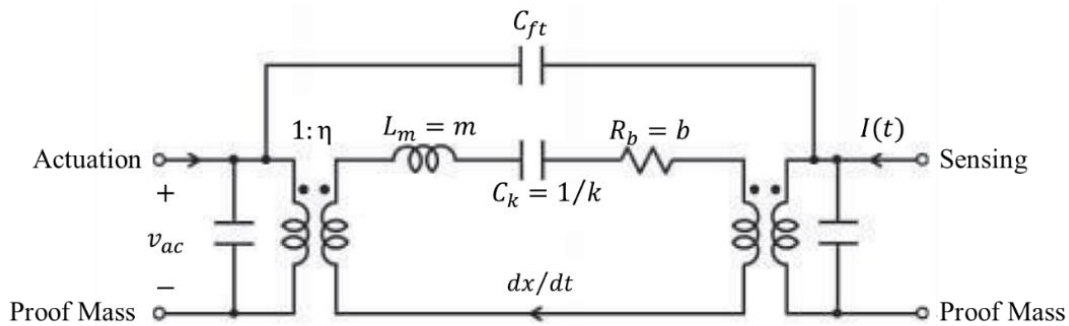
Figure 2.4 Linear capacitive equivalent circuit model for a lateral resonator oscillating only towards x.

28

The electromechanical transformer ratios may be different for the actuation and sensing capacitances. The R-L-C circuit represents the required second order linear equivalent model. The series resistance, inductance and capacitance are electrical equivalents of damping, mass and spring, and physically represent dissipated, stored kinetic and stored potential energies, respectively.

$$R_b = b, \qquad L_m = m, \qquad C_k = {}^1\!/_k \qquad\qquad (2.1\text{-}29)$$

The transformed damping resistance R_m, is the motional resistance. The lower the damping is, with a higher DC polarization voltage and higher sensitivity, the lower the motional resistance is.

$$R_m = \frac{b}{\eta^2} \qquad\qquad (2.1\text{-}30)$$

2.2.5. Damping

There are several damping mechanisms in a resonant micro electromechanical system. They depend on the geometry of the moving and fixed bodies, the mode of resonance, the medium and the structural materials. However, for a laterally resonating (varying gap) micro electromechanical system, squeeze film damping and slide film damping are dominant among others unless the system is vacuumed. The liquid (air or water) between the resonator gaps in perpendicular and parallel to direction of movement damps the oscillation and decreases Q.

Each damping mechanism individually contributes to the total quality factor that is Q:

$$\frac{1}{Q} = \sum \frac{1}{Q_{individual}} \qquad\qquad (2.1\text{-}31)$$

Related literature [52, Ch. 3], [53]–[56] includes more detailed analyses and derivations on damping mechanisms acting on resonant micro electromechanical systems and calculation of the quality factor.

2.2.6. Mechanical Noise and Sensitivity

Energy dissipation in micro electromechanical systems results in generation of noise. As the operation involves interaction between multiple physical domains resulting in

new dissipation and energy sources, noise analysis is important [14]. For a gravimetric resonant based sensor, noise determines the mass sensitivity; i.e. the minimum detectable mass.

The main mechanical noise source is the Brownian motion, which is the random motion and vibration of structural atoms. The resulting noise is a thermal white noise; i.e. Brownian noise. The noise force on a unit mass is given in Eq. (2.1-32) where k_B is the Boltzmann constant, T is the temperature and b is the effective damping.

$$F_{Brownian\ noise} = \sqrt{4k_B T b} \tag{2.1-32}$$

Mechanical noise has an important role in self-resonant systems. For closed loop operation, it is the start-up mechanism. The system does not oscillate if there is no noise. However, by causing an indefinite current at the sensing electrodes, it widens the bandwidth of the resonance and lowers the minimum detectible frequency shifts.

Theoretical limit for gravimetric detection can be given with the minimum detectable frequency shift and minimum detectable mass as written in Eq. (2.1-33) and (2.1-34).

$$(\Delta\omega)_{min} = \frac{2}{x_0}\sqrt{\omega_0 \omega_{bw}\frac{k_B T}{kQ}} \tag{2.1-33}$$

$$(\Delta m)_{min} = \frac{4m}{x_0}\sqrt{\frac{k_B T}{kQ}\frac{\omega_{bw}}{\omega_0}} \tag{2.1-34}$$

This limit only considers mechanical thermal noise while electrical noise coming from the interface electronics dominates the mechanical noise most of the time. Hence, in general the practical mass sensitivity is determined by the electrical noise. More analyses on noise and mass sensitivity can be found in [57].

2.2. Resonance Characterization

Interface and control electronics are compulsory to have a robust and self-oscillatory micro electromechanical system. They not only sense the output current of the sensor but also satisfy necessary conditions for self-oscillation of the proof mass. The

electronics determines the output quality factor, bandwidth and mass sensitivity by dominating the mechanical noise sources. This section summarizes the fundamentals of the interface electronics, self-oscillation theory and two feedthrough elimination methods.

2.2.1. Interface Electronics and Self-Oscillation

In order to measure the motional current through the sensing electrode, a transimpedance amplifier (TIA) is used. It converts the motional current of the resonator to voltage and keeps the sensing electrode at electrical ground. By forcing the output electrode to ground potential, TIA fixes the DC bias across the resonator capacitance and the parasitic capacitance to ground does not affect the detection sensitivity.

Figure 2.5 shows the conceptual implementation of TIA for a single ended configuration. For open loop characterization, a TIA with low input noise is sufficient with the use of an appropriate network/spectrum analyzer. The magnitude and phase responses of the system extracts information on the resonance characteristics. The shift in the resonance frequency corresponds to a change in total oscillating mass. By tracking the resonance characteristics, it is possible to weigh and count the attached mass and number of objects.
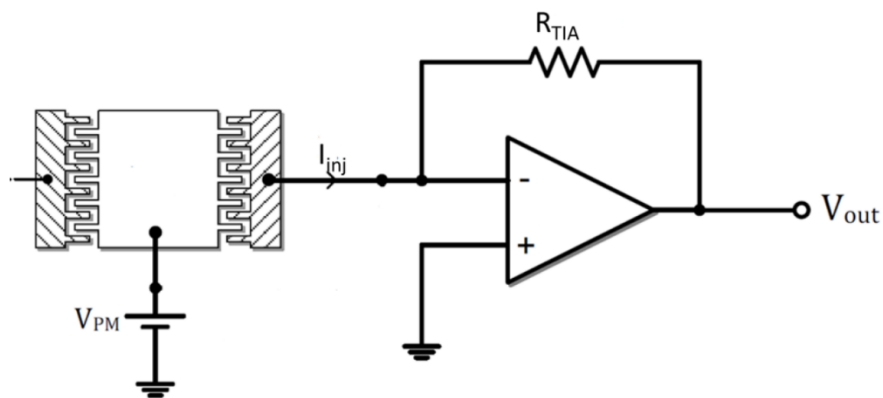
Figure 2.5 A transimpedance amplifier architecture. Connections with a sample resonator is shown [38].

Closed loop operation by employing self-oscillation is another method for the resonance characterization. The output current is converted to voltage with proper gain and phase, and fed back to the sensor as the actuation signal. For the self-oscillation,

Barkhausen criteria should also be satisfied in addition to conversion of the output current to voltage. It states that for a feedback loop, the magnitude of the loop transfer function (the loop gain) should be unity with a phase of zero at the oscillation frequency. The feedback loop is introduced within TIA with the feedback resistance, which is also inversely proportional to the input noise of the amplifier. Because of the feedthrough current, unlike an ideal resonator, the phase change at the resonance is not equal to 180º. Hence, a phase shifter can be used to change the phase response of the system to have the necessary zero phase at the resonance frequency.

2.2.2. Differential Characterization of the Resonators

As discussed in the previous sections, electrostatic actuation and capacitive interfaces are used to drive the resonators and to sense the output resonance characteristics. Although actuation and sensing mechanisms are easy to implement, the feedthrough current makes it harder to detect. The feedthrough current is the leakage current caused by the direct capacitive coupling between the actuation and the sensing ports. The packaging and wiring can also increase this leakage current.

The overall transfer function including the effect of the feedthrough capacitance is shown in Eq. (2.1-25). Resonance frequency of the system expressed by Eq. (2.1-25) is equal to $\sqrt{k/m}$. If there is no parasitic capacitance, the transfer function is purely real and maximum peak in the magnitude response is observed at the resonance frequency. Because the feedthrough current adds an imaginary term to the transfer function, both the magnitude and phase response of the system are affected. Magnitude of the leakage current increases with the frequency, which may dominate the resonance peak. Thus, existence of the feedthrough may prevent proper sensor operation.

In order to eliminate the feedthrough current, two differential methods can be used. The first method is to use an additional identical resonator with out-of-phase input signal to cancel out the feedthrough current at the output. The second method is based on resonators having differential output ports. By adding the output currents through these ports of the same resonator, the feedthrough current can directly be eliminated. Compared to the first one, having a single resonator with differential output ports eliminates the negative effects of mismatches between two separate resonators.

Using the equivalent electrical model of the resonator in Figure 2.4, the transfer function can be rewritten as:

$$Y_{\Sigma}(s) = \frac{sR_m C_f + s^2 L_m C_f + \frac{C_f}{C_k} + 1}{R_m + sL_m + \frac{1}{sC_k}} \tag{2.2-1}$$

At the resonance frequency ($s = j\omega_0 = j\,1\big/\sqrt{L_m C_k}$), Eq. (2.2-1) can be simplified as:

$$Y_{\Sigma}(j\omega_0) = \frac{1}{R_m} + j\omega_0 C_f \tag{2.2-2}$$

As seen in Eq. (2.2-2), if the feedthrough impedance, $\omega_0 C_f$, is much smaller than the motional conductance at the resonance frequency, then the feedthrough effect can be neglected.

2.2.3. 2nd Harmonic Reading at the Output

The actuation force acting on the proof mass is given in Eq. (2.1-16). The derived sensing current is given in Eq. (2.1-21). Substituting the rate of change of capacitance written in Eq. (2.1-23) into Eq. (2.1-21), the sensing current can be written as:

$$I \cong V_{DC}\varepsilon_0\varepsilon_r \frac{A}{x_0^2}\left(1 - \frac{2x}{x_0} + \frac{3x^2}{x_0^2}\right)\frac{dx}{dt} \tag{2.2-3}$$

Substituting a linear movement ($x = x_i \sin \omega t$) in to Eq. (2.2-3):

$$I \cong V_{DC}\varepsilon_0\varepsilon_r \frac{A}{x_0^2} x_i\omega\left(\left(\left(1 + \frac{3x_i^2}{4x_0^2}\right)\cos \omega t\right) - \left(\frac{2x_i}{x_0}\sin 2\omega t\right) - \left(\frac{3x_i^2}{4x_0^2}\cos 3\omega t\right)\right) \tag{2.2-4}$$

As seen in Eq. (2.2-4), the second harmonic term is proportional with the square of the displacement of the proof mass. Note that the feedthrough current is at the fundamental frequency so that the second harmonic term does not have a feedthrough term. Then, it is reasonable to detect the second harmonic term to eliminate the feedthrough effects. Although the gain decreases, the quality factor is higher when compared to the fundamental tone at the output (sensing) port.

In order to detect the resonance characteristics, a mixer can be placed after TIA to multiply the output voltage with the actuation signal. By doing so, the second harmonic term is carried to the fundamental tone and the third harmonic. Figure 2.6 shows the schematic representation of the resonance characterization and the frequency components at the sensing node and after the mixer.
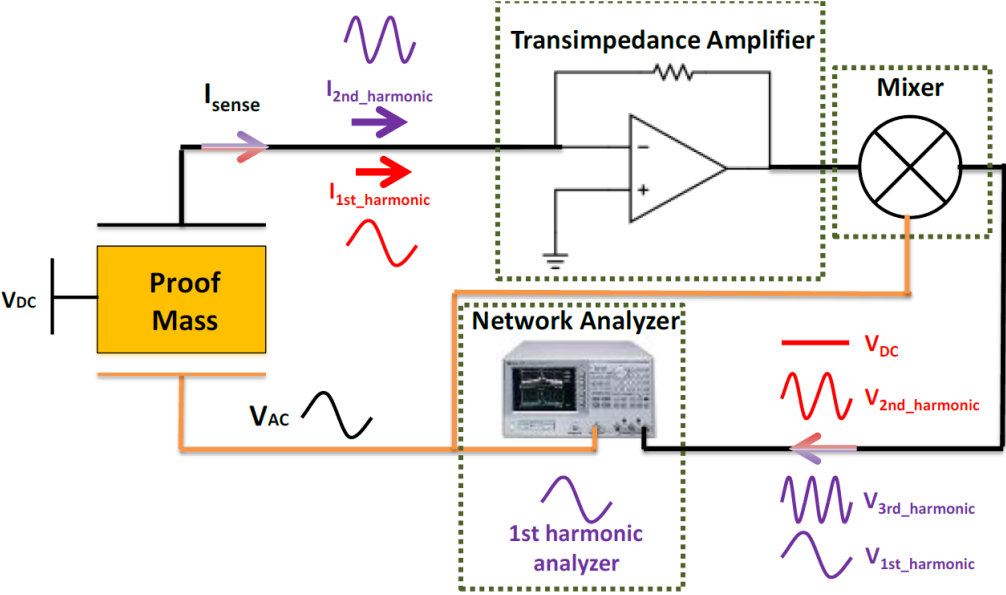
Figure 2.6 The test setup designed for second harmonic resonance characterization of the resonators [31].

2.3. Summary

In this chapter, theory of micro electromechanical resonators, actuation and interfacing mechanisms, and gravimetric detection is introduced. First, the theory of micro electromechanical resonators has been examined with appropriate mechanical and equivalent electrical models. Resonance frequency and quality factors are defined and derived. In addition to mechanical analyses, electrostatic actuation and capacitive sensing have also been examined in detail. Damping, noise and mass sensitivity have been discussed briefly before going further into the resonance characterization and the feedthrough elimination methods. Finally, the differential and second harmonic based resonance characterization methods have been summarized, and the necessary equations showing the applicability of the methods have been derived.

CHAPTER 3

DESIGN & SIMULATIONS

The structural design of the lateral gravimetric resonators is presented and discussed in Chapter 3. Section 3.1 qualitatively summarizes the structural design of the resonators. In Section 3.2, finite element method (FEM) simulations of the lateral resonators are presented. First, the expected resonance modes are simulated by solving the models for the Eigen frequencies. Then, the damping forces acting on the oscillating body are included in the model and quality factors for several configurations are solved. Finally, this chapter is summarized and concluded in Section 3.3.

3.1. Mechanical Structure of the Resonators

There are two important parameters for designing the resonators. The first one is the mass sensitivity, which is proportional to the total mass of the oscillating body. The second one is the bioactive surface on which the target cells will be caught and immobilized for quantification. The sensitivity of the resonator is inversely proportional with its total mass. Thus, the more sensitive is the resonator, the smaller the bioactive surface becomes. As a result, it is important to determine the device size including the thickness of the resonators.

Lateral oscillation is aimed for the operation as explained in the previous chapters. The micromechanical system consists of four spring beams at the corners of an oscillating proof mass. The folded beams are designed such that the motion in y direction is limited. The actuation and sensing electrodes and the proof mass are isolated from each other in order to prevent any short circuits. Bio-activation metals are patterned on the proof mass surface facing the microfluidic channels. The channel thickness is chosen comparable with the size of the target cells. By doing so, the probability of

35

attachment increases. An illustration of the structure for a varying overlap resonator is given in Figure 3.1.
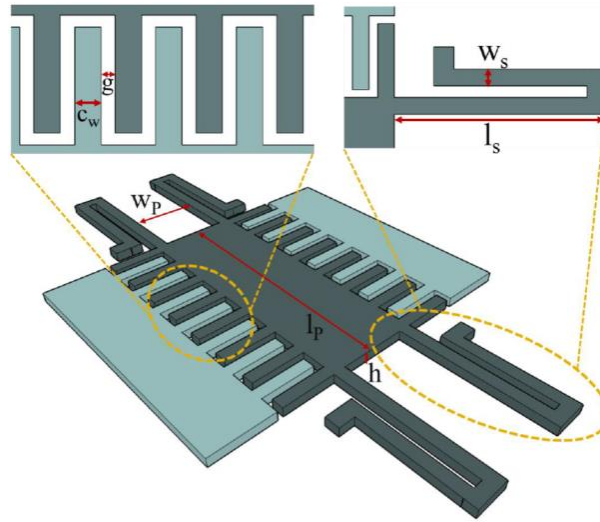
Figure 3.1 The mechanical structure of a varying overlap, lateral gravimetric resonator showing the folded spring beams and comb drives [41].

In his thesis, Kangül compared the capacitive sensitivity vs. proof mass displacement for the varying overlap and varying gap excitations and showed that the forces due to varying gap capacitance is dominant [38]. As a result, he designed and fabricated fingerless resonators. The proposed resonator design is easier to fabricate and simulate, as there exist no comb structures. The tests and measurements revealed that it is as good as the other designs in terms of mass sensitivity although it lacks a bit of current gain. Therefore, it was preferred as a benchmark design throughout this thesis. RCGS#2 in [38] is studied in the following subsections, and the results and the simulations are compared in Section 3.3.

3.1.1. The Folded Spring Beams

Stiffness of the springs in the directions other than the lateral direction must be large enough to prevent undesired oscillations disturbing the lateral resonance [40]. Hence, the spring must be stiffer in y and z direction when compared with the x direction; i.e. $k_y, k_z \gg k_x$. In addition to the direction of oscillation, the spring stiffness also determines the frequency of oscillation. The mass sensitivity is a function of the frequency of oscillation, too. Thus, one should be careful while designing the spring beams.

Folded flexures have been used for implementing the lateral gravimetric resonators by the previous researchers on the application [38], [40]–[42]. The folding prevents bucking by releasing the stress. The structure behaves linearly during the deflection. The spring constants along x, y, and z directions are given in Eq. (3.1-1), Eq. (3.1-2) and Eq. (3.1-3):

$$k_x = \frac{1}{2} E_x \frac{t w_b^3}{l_b^3} \tag{3.1-1}$$

$$k_y = \frac{1}{2} E_y \frac{t w_b}{l_b} \tag{3.1-2}$$

$$k_z = \frac{1}{2} E_z \frac{w_b t^3}{l_b^3} \tag{3.1-3}$$

where l_b and w_b are the length and width of the folded beam and t is the thickness.

3.1.2. RCGS#2 as the Benchmark Design
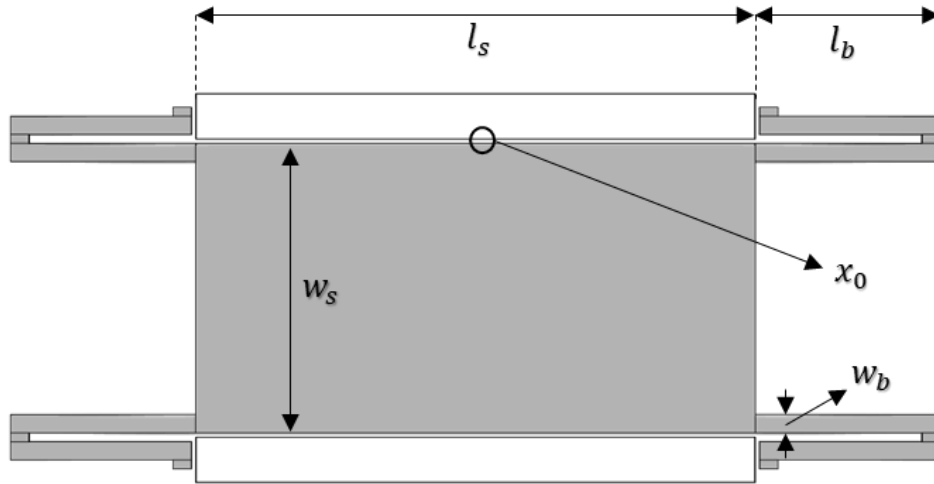
Figure 3.2 Schematic representation of the studied fingerless resonator RCGS#2. The length and width of the beams and the proof mass are shown on the schematic.

The schematic representation and design parameters of the fingerless lateral resonator are shown in Figure 3.2. l_s and w_s are the length and width of the proof mass. l_b and w_b are the length and width of the folded spring beams. The gap distance between the oscillating proof mass and the actuation and sensing electrodes is shown with x_0. The thickness of the resonator (including the spring beams and the proof mass) and the

electrodes is determined by the thickness of the active Si layer of the SOI. In this thesis, two different device thicknesses are studied. The calculated characteristics are summarized in Table 3.1.

Table 3.1 Design parameters and calculated resonance characteristics of RCGS#2.

ID	t	l_s	w_s	l_b	w_b	x_0	f_0
R#1	35 μm	248 μm	128 μm	80 μm	8 μm	2 μm	285.8 kHz
R#2	10 μm						265.5 kHz

3.2. FEM Simulations

The resonators are modelled and simulated in order to extract the Eigen frequencies, resonance modes, and expected quality factors. COMSOL Multiphysics is used for finite element analyses. Electromechanics physics under structural mechanics of MEMS module reveals the resonance characteristics even including the effects of spring softening by considering electric fields around the structural blocks.

3.2.1. Eigenfrequencies and Resonance Modes

Electromechanics interface of COMSOL combines structural mechanics and electrostatics in order to model the displacement of electrostatically excited structures. The resonator is modelled as a linear elastic material subject to external loads, deformation of which is described by Cauchy's equation. The interface solves Cauchy's equation by substituting the electromagnetic stress tensor to solve the forces, deformation and Eigen frequencies.

The 35 μm thick resonator (R#1) shown in Figure 3.2 was modelled on COMSOL Multiphysics, Electromechanics Interface and solved for the normal modes. For the sake of simplicity and computational costs, the parylene coating, bio-activation metals and damping were not included in the model. The model was meshed using free tetrahedral meshing. The aim was just to extract the natural frequencies and deformation behaviors of resonance modes. Because the resonator is actuated electrostatically via the lateral actuation electrode, only the lateral mode is shown here. The Eigen frequency was found as 300 kHz. The deformation of the mode is plotted in Figure 3.3. Notice that, the deformation is exaggerated in order to show the motion.
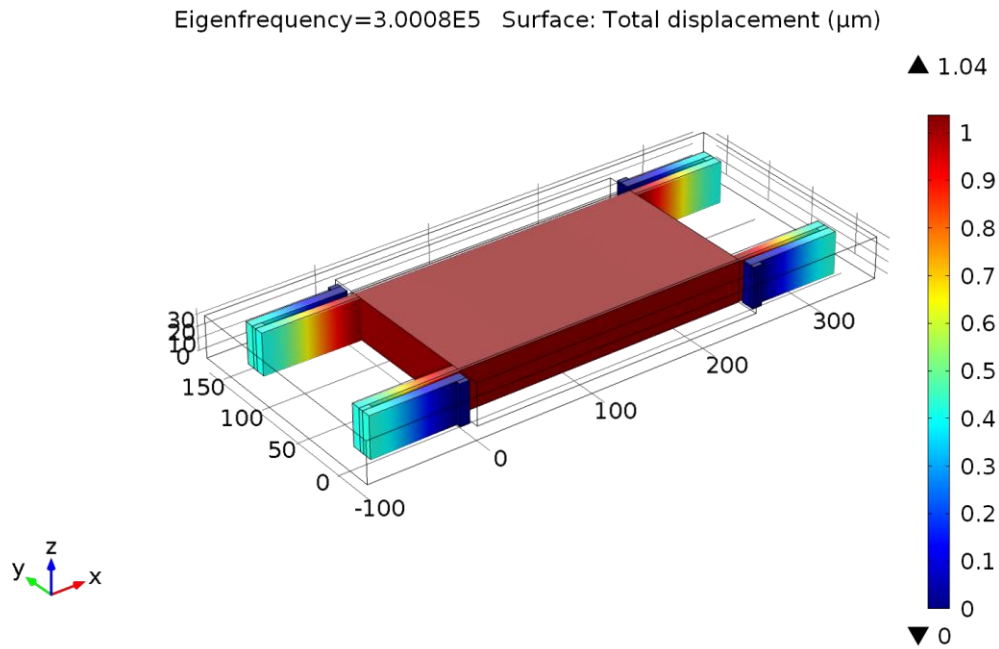
Figure 3.3 The lateral mode resonance mode extracted from the FEM analysis for R#1. The parylene coating, undercuts and fabrication errors, the bio-activation metals and damping were not included in the model.

The modal characteristics of the 10 μm thick resonator (R#2) was extracted similarly. The Eigen frequency was found as 299 kHz. The mode shape is not given because it is the same as R#1. Notice that the Eigen frequencies of R#1 and R#2 are very close. This is a result of ignoring materials other than Si such as parylene and gold. As the thickness decreases, the effect of added mass increases. Therefore, in real, the difference between the frequencies should be much more than 1 kHz. In addition, although the lateral mode seems to be the first mode for R#1, for R#2 it is the second mode. The first mode of R#2 is out-of-plane since the spring constant along z direction decreases with the device thickness and becomes comparable with that along x direction. To learn more on the resonance characteristics, a more detailed simulation was necessary. Thus, the fabrication errors, damping and parylene coating were included in the detailed model.

3.2.2. Damping and Quality Factor

In order to simulate real-time cases, the mechanical structure was modelled in detail. The fabrication errors due to DRIE structure etch was included in the model with an over etching of 0.1 μm in each sides of trenches. This changes the spring constants in

39

each directions and decreases the squeeze film damping. The bio-activation metals were included by just modelling the gold layer that is 0.3 µm thick. In order to decrease the computational costs (during the meshing of the blocks), the parylene coating was also added to the model as a 0.3 µm thick layer (similar to real case) only on the bioactive side of the blocks. In other words, the sidewall coatings were ignored during the modelling. Free triangular meshing was used on one of the cut-planes normal to z direction. Then the constructed meshes were swept for all domains in order to complete the 3D meshing of the constructed model. By this way, the thickness difference between the layers was compensated by sacrificing the mesh quality. The constructed model including the fabrication errors, parylene coating and bio-activation metals is shown in Figure 3.4
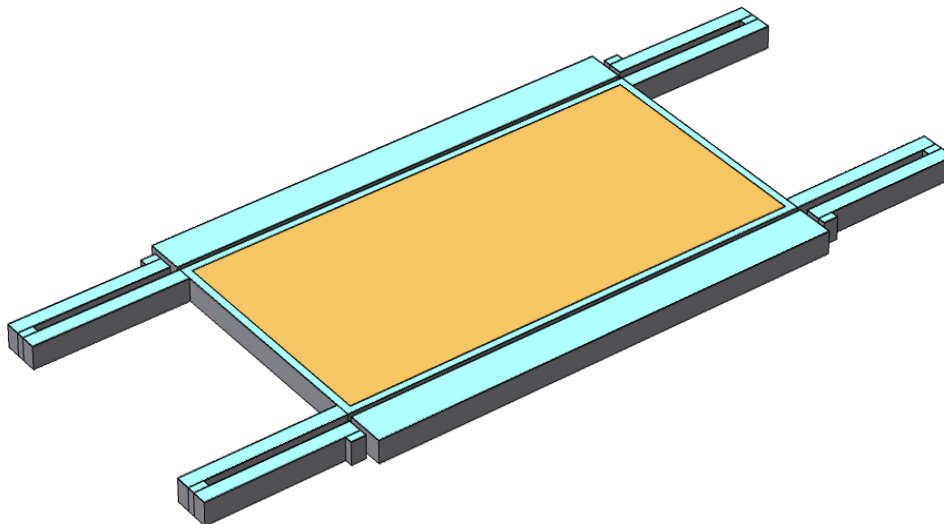
Figure 3.4 The detailed model of R#2. The thickness of Si layer is 10 µm. DRIE over-etching is modelled as 0.1 µm in each wall of trenches. Si, parylene and metal are shown with gray, cyan and gold respectively.

The viscous fluid damping [32], [58] acting on the resonator was modelled using boundary loads. Each damping factor was added as a force acting on the selected surfaces. For example, for the sidewalls along the direction of oscillation (y direction in the simulation), the dominant damping factor is squeeze film damping [32]. Similarly, for the top and bottom surfaces, which are along z direction, the dominating damping is drag force and slide film damping [32]. The damping factors included in the model are summarized in Table 3.2.

Table 3.2 Summary of simulating damping effects, forces and the loaded surfaces in the detailed model.

Damping factor	Effective surfaces	Force Equation
Squeeze film damping	Resonator gaps	$\beta\mu(t^3 l/x_0^3)v$
Drag force	Top, bottom	$\mu(16/3)wv$
Slide film damping	Top, bottom, side	$\mu(wl/\delta)v$

The simulation was solved for Eigen frequencies again. However, when compared with the basic models in Section 3.2.1, the solved Eigen frequencies have imaginary parts this time due to damping. Using the found Eigen frequencies for the mode of interest, the quality factor can be extracted by substituting the real and imaginary parts in Eq. (3.2-1):

$$Q = \frac{\text{Im}\{\lambda\}}{2\text{Re}\{\lambda\}} \tag{3.2-1}$$

where $\lambda = -2\pi jf$ and f is the solved Eigen frequency.

The effects of air damping was extracted from the models. For both thicknesses, the real part of the Eigen frequencies of lateral modes decreased as discussed in the previous section. This is a result of the added mass due to the parylene and metal layers, and due to the change in the spring constants because of fabrication errors. In addition to these, damping was modelled as a boundary load on the related surfaces, which also affected the solutions. The damping forces were included one by one for each surface of the model. Then, the Q-factors were calculated. Notice that, this was just an approximation in order to calculate the Q-factors. In order to analyze the damped system, one should use Fluid-Structure Interaction Interface and couple it with Electromechanics on COMSOL.

For R#1 damped in air, the lateral (and the first) Eigen frequency was found as 2.8523E5-1021j Hz and shown in Figure 3.5. The calculated Q-factor is ~140 by using Eq. (3.2-1). The mode and Eigen frequency are shown in Figure 3.5. For R#2, the lateral Eigen frequency was found as 2.6108E5-323.67j Hz and shown in Figure 3.6. The calculated Q-factor is ~403 for the air-damped model. Compared with the Eigen frequency found in simplified model, the damped Eigen frequency is closer to the analytical calculations.

Eigenfrequency=2.8523E5-1021i   Surface: Total displacement (μm)
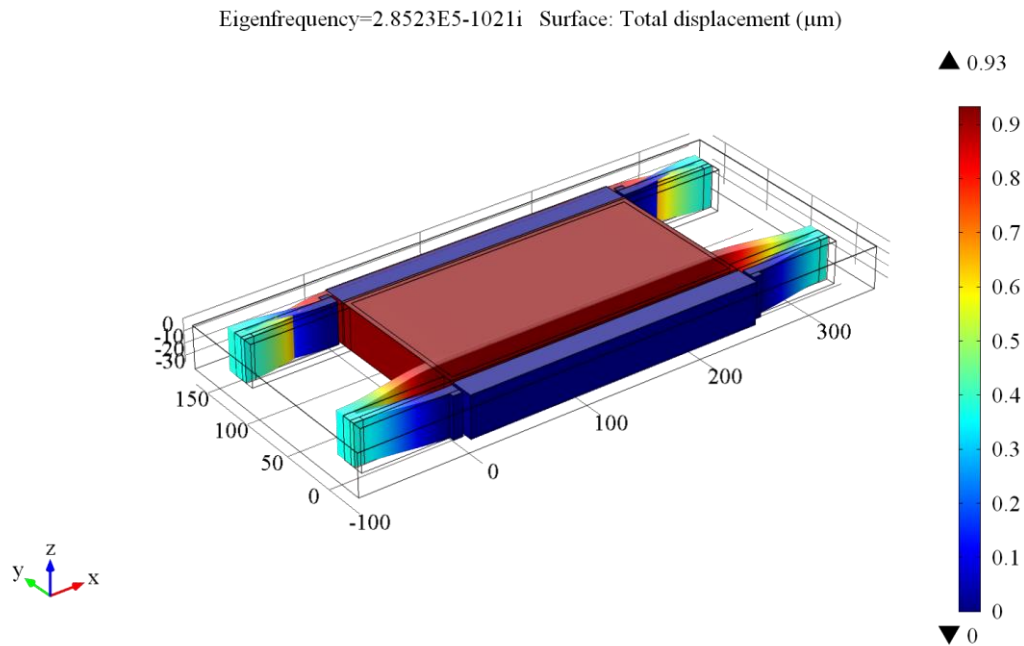
Figure 3.5 The first Eigen frequency and mode shape for R#1 for the air-damped model. Q=139.68. Notice that the displacement for all points on the proof mass is the same for the lateral mode shape. This proves that the lateral gravimetric resonators have linear spatial mass sensitivity.

Eigenfrequency=2.6108E5-323.67i   Surface: Total displacement (μm)
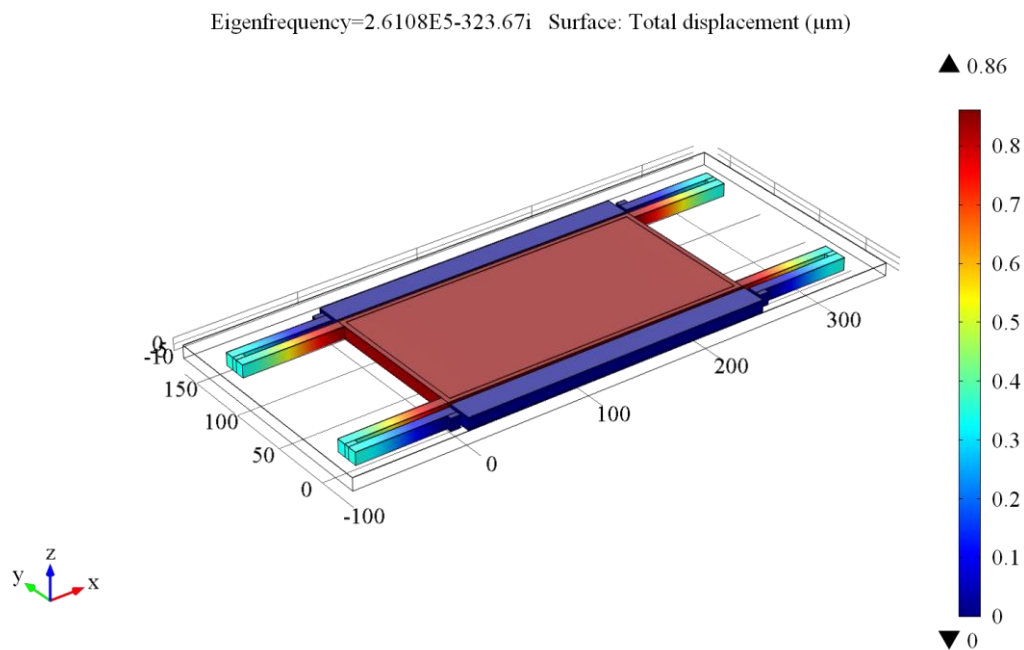
Figure 3.6 The lateral Eigen frequency and mode shape for R$2 for the air-damped model. Q=403.31. Notice that the lateral mode is the second Eigen mode when the thickness is 10 μm. The reason is the change in the stiffness of the folded beams. When the thickness is decreased, the spring constants in y and z directions become comparable, introducing an out-of-plane mode as the first Eigen frequency.

42

3.3. Summary

Design considerations for lateral gravimetric resonators are summarized in this chapter. First, the mechanical structure of the studied resonator is shown and briefly explained. Then, the resonance characteristics for different resonator parameters are calculated. In addition to the analytical results, results of COMSOL simulations for resonance modes and damping are presented. The calculations and simulation results are compared and summarized in Table 3.3. Notice that, the analytical calculations do not include the fabrication errors in sizes. Similarly, the simulation models are also simplified to decrease the computational cost and to save time while solving them.

Table 3.3 Comparison of analytical calculations and COMSOL results for the resonators.

ID	Analytical	Simplified FEM	Detailed FEM	
	f_0	f	f	Q_{air}
R#1	285.5 kHz	300 kHz	285.2 kHz	140
R#2	265.5 kHz	299 kHz	261.1 kHz	403

CHAPTER 4

FABRICATION

This chapter presents the problems with the previous generation fabrication methods (process flows) and the motivation for developing a new method for fabrication of the gravimetric lateral resonators. First, previous fabrication methods in [14], [40], [41] are introduced. The last one in [38], [42] is explained in detail. All of them include anodic bonding as a crucial fabrication step, which limits the possibilities and performance parameters of the resonators. These limitations and main disadvantages of anodic bonding are discussed and parylene bonding is proposed as a solution.

Before going into the fabrication of the lateral resonators, parylene bonding as a fabrication method is introduced in brief. The characteristics of the polymer as a bonding interface (and a structural layer) and possible effects on the application are stated with bonding and annealing experiments. The results of bulk parylene bonding experiments are compared with the literature and commented on.

Finally, *a new fabrication method utilizing parylene bonding* is proposed for fabrication of the gravimetric lateral resonators. The process flow of the method is given and the fabrication steps are explained with adequate details. A side effect of parylene bonding; i.e. parylene membrane formation is shown on the process flow and discussed. Optical microscope and SEM images of the fabrication steps are also provided in this chapter.

4.1. Previous Generation Fabrications and Problems

As briefly stated in Chapter 1, all of the previous generation fabrication methods had included at least one wafer level bonding as a process step [14], [38], [40]–[42]. Almost all of them proposed anodic bonding in order to bond the SOI wafer, on which

the resonators are structured, and the glass wafers, on which either recesses or microfluidic channels are etched.

Anodic bonding strongly connects silicon to glass or metals with a high yield by using electric field [59], [60]. It requires high electrostatic fields; hence, a high current flows through the wafers. Moreover, the interfacing surfaces of the wafers should be in atomic contact for bonding to take place [61]. Applied electrical potential (up to a few kilo-volts), temperature (to increase the electrical conductivity) and current limit during the bonding determines the process and the resulting bonding quality in terms of strength and bonding yield. The temperature adjustments were usually around 350ºC during the previous generation process flows.

For the fabrication of lateral gravimetric resonators, typically DRIE is used to structure the resonators on a SOI wafer. The buried oxide acts as an etch-stopping layer; thus, the thickness of the active layer determines the resonator thickness. Before the DRIE, the bio-activation metals and pad routings are structured on the SOI wafer using sputtering and wet etch (or liftoff) processes. Depending on the fabrication method, recesses and/or microfluidic channels are etched on a glass substrate and pad metallization is completed. In the earliest examples by Bayraktar and Eroğlu, the glass wafer was used just as a handle layer with recesses below the lateral resonators [40], [41]. Then, the wafers were anodic bonded to have an integrated structure. The microfluidic channels were structured with PDMS and plasma bonding was used to bond the channels with the resonators. However, the fabrication was too complex and expensive with a low bonding yield. This was the main reason why Töral and Kangül eliminated the PDMS for microfluidics and structured the microfluidic connections also on the glass wafer [38], [42]. In order to integrate the resonators with microfluidics, they were also using anodic bonding. Then, to release the resonators, the Si handle wafer of the SOI was being etched using DRIE. Last, the buried oxide was etched with BHF and the fabrication was completed with the dicing. In order for hydrophobicity, parylene was coated after the fabrication.

The last generation fabrication method was used by Kangül to fabricate the lateral gravimetric resonators [38]. The fabrication method was based on Töral's proposal

utilizing both anodic bonding of SOI and glass wafers, and fabrication of microfluidics on the glass wafer [42]. The process flow is shown in Figure 4.1.
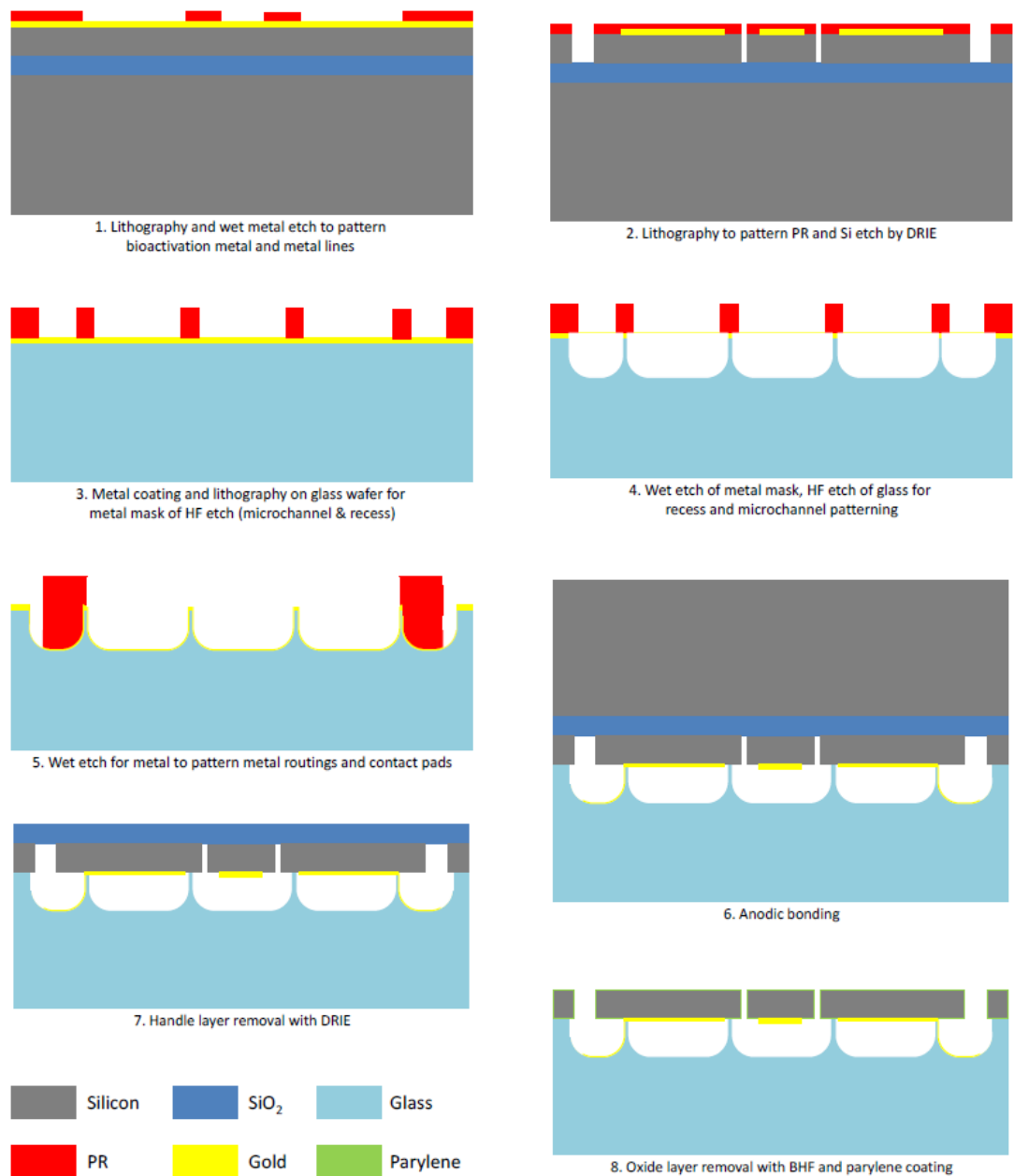
Figure 4.1 The last generation fabrication method utilizing anodic bonding as a fabrication step [38].

The main advantage of this fabrication method was the elimination of PDMS micromachining for microfluidics. The fabrication, especially the metallization of the devices, is easier compared to the earliest fabrication methods because the metallization is completed before the DRIE structuring. In other words, there is no further processing after releasing the resonators by handle layer removal. The recesses

and microfluidic channels can be etched in the same process step; thus, the fabrication cost also decreased.

During the fabrication, the SOI and glass wafers are being structured separately but in parallel. For the SOI processing, first the routing and bio-activation metals are coated by sputtering. Either wet etching or liftoff can be used to pattern the metals. For the last generation method, they preferred wet etching of the metals. Cr (30 nm) is sputtered as an adhesion layer for the Au (300 nm). After the patterning of the metals via wet etching, DRIE is used for structure etch to pattern the resonators and connection islands. A photoresist layer is used as the etching mask. Buried oxide acts as an etch-stopping layer; however, if the plasma time cannot be adjusted properly, DRIE notching can damage the resonators, folded beam springs and resonator fingers.

Processing of the glass wafer also starts with a metallization for masking the isotropic HF wet etching. The sputtered metal (30 nm Cr and 300 nm Au) is patterned with wet etching. The recesses and microfluidic channels are etched in HF. The etching time determines the thickness of the channels. Then, the masking metal is etched away. Pad routing metal layer is coated and patterned using metal sputtering and wet etching. During the Au sputtering, because of diffusion of Au particles, an additional Au etching may be necessary after Cr etching. Otherwise, the diffused layer of Au may short-circuit the actuation, sensing or DC electrodes of the resonators; or may cause additional resistive feedthrough.

In order to integrate the resonators with the microfluidics, the two wafers are anodic bonded. Then, the Si handle wafer of the structured SOI wafer is thinned using DRIE without any masks. The buried oxide stops the DRIE etching. After all the Si layer is etched away, the resonators are released with BHF etching of the buried oxide layer and by using an acetone-IPA-methanol release sequence. The release sequence prevents any stiction due to surface tensions during the water evaporation.

In order to make the resonators hydrophobic, after the fabrication finishes, a thin parylene layer is coated by using the Gorham process [62]. The additional parylene layer prevents any liquid leakage from the resonator gaps and decreases the squeezed film damping significantly. However, it also coats the microchannel walls and bio-

activation metals in addition to the resonator gaps, making the microfluidic channel hydrophobic, too. The coating is not controllable. Töral claimed that the bio-activation metals are not coated because parylene cannot penetrate into such deep through the micron sized gaps [42]. However, there is no experiment showing whether this claim was true or not. Later in this chapter, it will be shown that parylene can penetrate through the gaps even during a 35-µm SOI processing. Moreover, selective etching of the parylene coating is not possible because it is coated after the fabrication finishes.

During the tests with previously fabricated resonators, it is observed that the DC charging of the proof mass with the DC potential (tens of volts) causes electrolysis of the liquid inside the microfluidic channel. The reason was obviously the direct contact between the proof mass and the liquid inside. There was no insulation between the applied potential and the liquid. If the proof mass is coated with the parylene, then the bio-activation surface is also coated making the bio-activation of the resonators impossible. This is one of the most important problems of the previous methods.

Other than these, if any conductive particle is stuck in the gaps between the silicon connection islands or between the resonator gaps, the electrodes are short-circuited and the operation fails. There is no guarantee in the previous process flows that prevents these unexpected short circuits. Any Si particle due to the dicing or dusts can short the electrodes causing the operation failing and the characterization of the resonators impossible.

Another disadvantage of anodic-bonding based fabrication is that it is difficult to integrate the cell enrichment (separation) systems such as a DEP cell separator with the gravimetric resonant based cell detection system. An insulating layer is necessary to prevent direct contacts between the DEP medium and the DEP electrodes in a DEP based system, which was impossible with the previous generation fabrication methods. In addition, because anodic bonding requires direct atomic contact between the wafer surfaces, the close metal layers also prevents the bonding of glass and SOI wafers around the metal structures.

To summarize, although anodic bonding is a robust fabrication method increasing the bonding yield and decreasing the fabrication costs, there are still problems, which limit

the resonator performance and application possibilities. A fabrication method utilizing parylene bonding as the integration step can overcome most of the stated problems and disadvantages; thus opens up new horizons for future applications of the lateral resonators.

4.2. Solution: Parylene Bonding

As briefly discussed in the introduction, parylene is a biocompatible, chemically inert and hydrophobic polymer. It is widely used in MEMS fabrication as insulating and structural layers because it is cheap and easy to process [44]. Moreover, parylene allows low temperature bonding because it is an adhesive thermoplastic when heated [44], [49]. It is vapor-deposited as a thin film using the Gorham process without any liquid phase transition [62]. As it is a thermoplastic, the polymer chains can re-entangle, forming an adhesive bonding layer. Finally yet importantly, parylene bonding enables three-dimensional metal integration [48].

Parylene bonding solves most of the problems since using parylene as an intermediate layer; the coating step of the process flow is more controllable. First, selective etching is possible. Second, the thickness around the resonator gaps can be properly adjusted. Third, the glass microfluidic channels stay hydrophilic, as the walls are not coated with a layer of parylene. Forth, the gaps between the silicon islands are coated with a layer of insulating parylene, decreasing the risk of unexpected short circuits. Fifth, by using another layer of insulating thin film, it is now possible to insulate the flowing liquid from the DC applied proof mass (to prevent electrolysis of the liquid). Finally, it enables the integration of DEP based enrichment system with the gravimetric resonant based CTC detection system.

4.2.1. Parylene as a Bonding Interface

In order to ensure whether using parylene as a bonding interface is practical or not, the characteristics of the polymer should be analyzed at first. During the bonding process, the temperature is increased slightly, kept constant for a while and decreased again slightly. At the constant temperature, a force is applied vertically using a piston to bond the wafers. This process is very similar to an annealing except the force

application where the polymer is cured with temperature to enhance its properties. Mechanical and chemical characteristics change after the annealing, which may affect the performance parameters of the fabricated micro electromechanical device or the integrated circuit. It is reasonable to analyze these changes before practicing the fabrication of lateral gravimetric resonators.

Thermochemical analysis of the parylene thin film reveals the heat absorption properties such as the glass transition and melting temperatures. Previously, Kim and Najafi published their differential scanning calorimetry (DSC) analysis where they heated parylene over its melting temperature and recorded the heat absorption throughout the heating [43], [44]. They concluded that bonding should be a result of physical chain entanglements because there is no chemical reaction occurring during the whole process except the glass transition and the melting. They stated the temperatures between the glass transition and the melting as "bondable temperature range". The physical chain entanglement process proposed is shown in Figure 1.12. The glass transition and melting temperatures was reported as 109ºC and 303ºC [44].
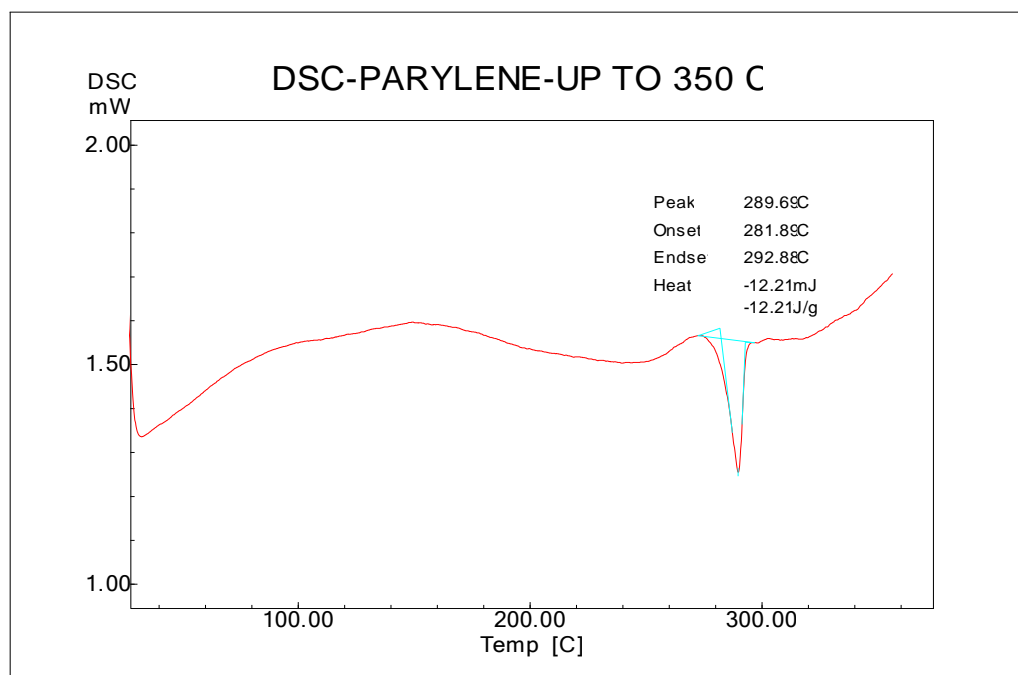
Figure 4.2 Thermochemical (DSC) analysis result for parylene thin film deposited at METU-MEMS.

Similar to the study in [43], in order to detect the bondable temperatures, a DSC analysis was conducted on the parylene-C thin films deposited at METU-MEMS

51

Center. Shimadzu DSC-60 is used during the analyses. 1 mg samples of the thin film were heated up to 350ºC and then cooled off to the room temperature at nitrogen atmosphere. Temperature rate and sampling frequency was adjusted as 10ºC/min and 1 Hz respectively. Several runs revealed that the melting temperature is at 289.7ºC as shown in Figure 4.2. On the other hand, there were no heat absorption peaks to detect the glass transition temperature clearly. Two different measurements (not shown here) with midpoints around 145ºC revealed that it is much more than 109ºC. This implies that the bondable temperature range was between ~145ºC and 290ºC.

Below the glass transition point, the entanglement of the parylene chains is not possible. Above the melting point, the polymer melts and flows, damaging the patterned structures and alignment of the wafers. When compared to the anodic bonding, the bonding should occur at lower temperatures. In addition, no electric field is required for bonding to take place. This implies that there will be no risk of metal burning or diffusing, and sparks that burn the silicon islands during the bonding step.
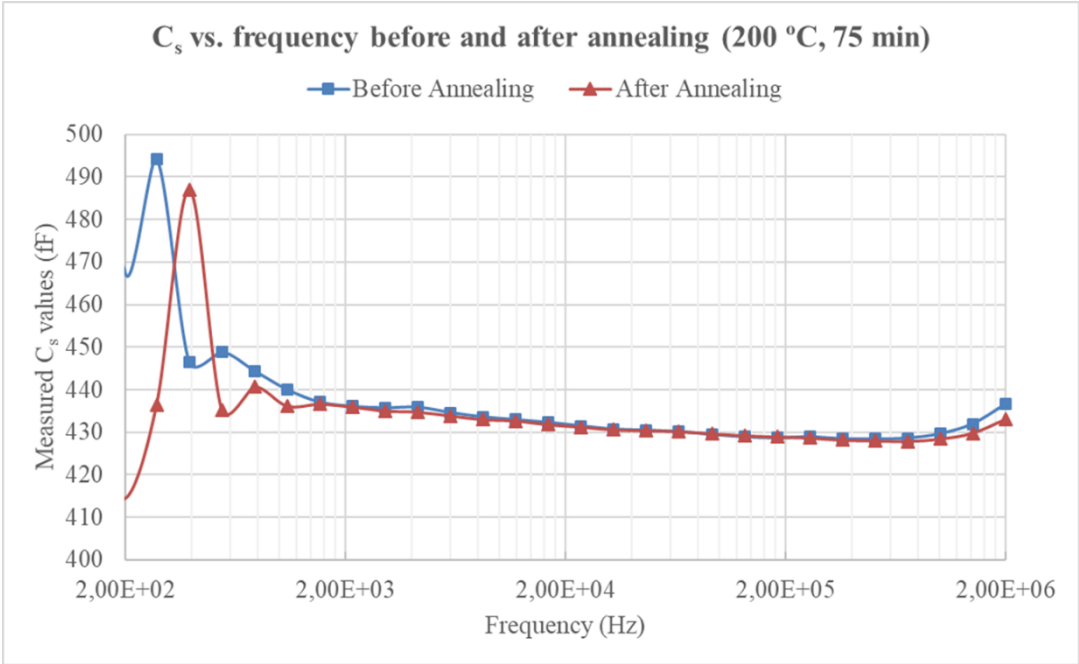
Figure 4.3 Serial capacitance measurements on the planar DEP electrodes. Blue and orange lines show the measurements before and after the annealing process respectively.

In addition to the thermochemical characteristics, the dielectric properties are also crucial for the application. To understand the effects of thermal bonding on the DEP performance of parylene, planar electrodes of a DEP chip are used. The serial

capacitance between the electrodes was measured using Agilent E4980 LCR meter before and after the annealing. The chip was annealed at 200ºC for 75 minutes after the first measurement. Figure 4.3 shows the serial capacitance between the planar DEP electrodes with respect to frequency, before and after the annealing. There is no significant difference between the two measurements, implying that the dielectric constant did not affect the DEP performance even though it changed. It is concluded that the thermal bonding process will not affect the DEP performance even after the integration of gravimetric detection system with the DEP based enrichment system. The details of this measurement is given in Appendix A.

The details of mechanical, chemical and physical properties of parylene-C after annealing are reported in [63]. It is stated that with the annealing, parylene films become softer with a slight decrease in the Young's modulus. In addition, the crystallinity of the polymer increases with the annealing temperature; meaning that the intermediate bonding layer will be more crystalized after the bonding. This implies that the bonding layer will be mechanically and electrically stable for longer times. The electrical insulation stays similar even after annealing at higher temperatures.

The hydrophobicity and the hydrophilicity of parylene are studied in [64] and [65] respectively. The bulk parylene (without any post processing) is found to be hydrophobic even at thicknesses around 100 nm [64]. It is stated that the hydrophobicity exponentially increases and saturates with increasing thickness of the parylene film. In addition to its being hydrophobic, by applying consecutive oxygen plasma, the film can be made hydrophilic [65]. The hydrophobicity recovers after a while even though it cannot reach its initial performance. This is important for the fabrication method proposed, as oxygen plasma is used to activate the interface surface before the thermal bonding step. On the other hand, it was previously reported with proper calculations that parylene indeed preserves its hydrophobicity enough that it can prevent liquid leakage from narrow slits (as much as 10 μm) [39].

4.2.2. *Bonding Trials and Comparison with the Literature*
Parylene intermediate layer bonding was first reported in 2003 by Kim and Najafi to transfer freestanding membranes at wafer-level [43]. They coated 381 nm thin parylene to each wafer and bonded them at 230ºC with a 800 N force for 30 minutes

under vacuum. The resulting tensile bonding strength was reported as 3.6 MPa. They discovered that the intermediate layer contracted during the bonding, implying the chain re-entanglements. They stated the major disadvantage of the technique as particle existence between the wafers as any particle significantly decreased the bonding yield.

In a later study by Kim and Najafi, they studied the characterization of parylene bonding and analyzed the environmental and chemical effects on bonding strength [44]. Accordingly, the bonding strength lasts for up to 2 years with a 7% deviation. Short time exposure to chemicals such as acetone, IPA, BHF or MF319 does not affect the bonding strength significantly. It is promising for the fabrication of the lateral gravimetric resonators as after bonding, several wet processes and lithography steps exist. The thickness does not significantly increases the bonding strength. They determined the minimum thickness as 381 nm, which is less than typical thickness previously used to coat the lateral gravimetric resonators. They were also the first to try the contact alignment of structured nonplanar surfaces for bonding.

Shu *et al.* reported single intermediate layer parylene bonding utilizing parylene to silicon bonding for the first time [47]. They compared their results with the double intermediate layer, parylene to parylene bonding and reported no significant difference in the bonding qualities. The bonding temperature was 230ºC with 1000N applied for 30 minutes under vacuum, and the resulting tensile bonding strength was 2.38 MPa.

Low temperature wafer bonding by using a single intermediate parylene layer was reported in detail by Çiftlik and Gijs [48]. They stated that the parylene-parylene interface at double layer bonding is the interface of fracture. Thus, they proposed to eliminate this interface to increase the bonding strength. They coated a Pyrex wafer with 10 μm parylene-C and bonded it to 4 different wafers that are (1) thermal oxide coated, (2) nitride coated and bare silicon (3) treated with oxygen plasma and (4) treated with CF_4 plasma. The bonding temperature was adjusted as 280ºC. A 7% reduction in parylene thickness was noted after bonding. Pull tests resulted a tensile bonding strength of 8.8 MPa for the parylene-silicon bonding where the bare silicon surface was treated with oxygen plasma.

54

Before proposing a fabrication method, a number of parylene bonding experiments were conducted at METU-MEMS Center, too. The aim was to learn the technique, to optimize the bonding conditions and to inspect the bonding yield before fabricating the lateral gravimetric resonators. In order for coating, a SCS PDS2010 parylene deposition system was used throughout the studies reported in this thesis. STS Multiplex RIE was used to pattern the parylene intermediate layer. For the bare bonding trials, no alignment was necessary, as there were no structures on the wafers. For the bonding, EVG501 wafer bonder was utilized in eutectic configuration to thermally-bond the two wafers by heating the intermediate parylene layer(s).

The bondable temperature range has been determined as ~145ºC to ~300ºC based on the DSC analyses. In order to determine the optimum bonding temperature, three discrete temperatures were tested during the trials: 150ºC, 200ºC and 250ºC. For all the experiments, the backsides of the wafers were covered with a dicing tape before the deposition of parylene to prevent parylene coating and to protect the bonding chuck from any parylene residuals during the thermal bonding process. The wafers were cleaned using acetone, IPA and DI water before the coating. Just before the bonding, the surfaces were activated using a short oxygen plasma (2 minutes at 300W, 0.2 Torr and 45ºC twice).

For the first trial, 4" glass and silicon wafers were coated with 1 μm parylene-C. Bonding took place at 150ºC, under 1 mTorr vacuum, with 1000N piston force for 1 hour. For the second trial, only the silicon wafer was coated with 1 μm thick parylene-C and the first bonding conditions were repeated. Figure 4.4 a) and b) shows the resulting bonding yields for the two trials completed at 150ºC. It was observed that not only particles on the bonding interface but also air bubbles trapped between the wafers were decreasing the resulting bonding yield.

In order to increase the bonding yield, the bonding temperature and the piston force were increased to 200ºC and 2000 N respectively. The wafers were bonded just after the coating and cleaning of the wafers again with a plasma activation at vacuum. The third and fourth trials were replicas of the first and the second trials in terms of film thicknesses on silicon (and glass) wafers. The resulting yields of the third and fourth bonding trials are shown in Figure 4.4 c) and d) respectively. The yield was increased.
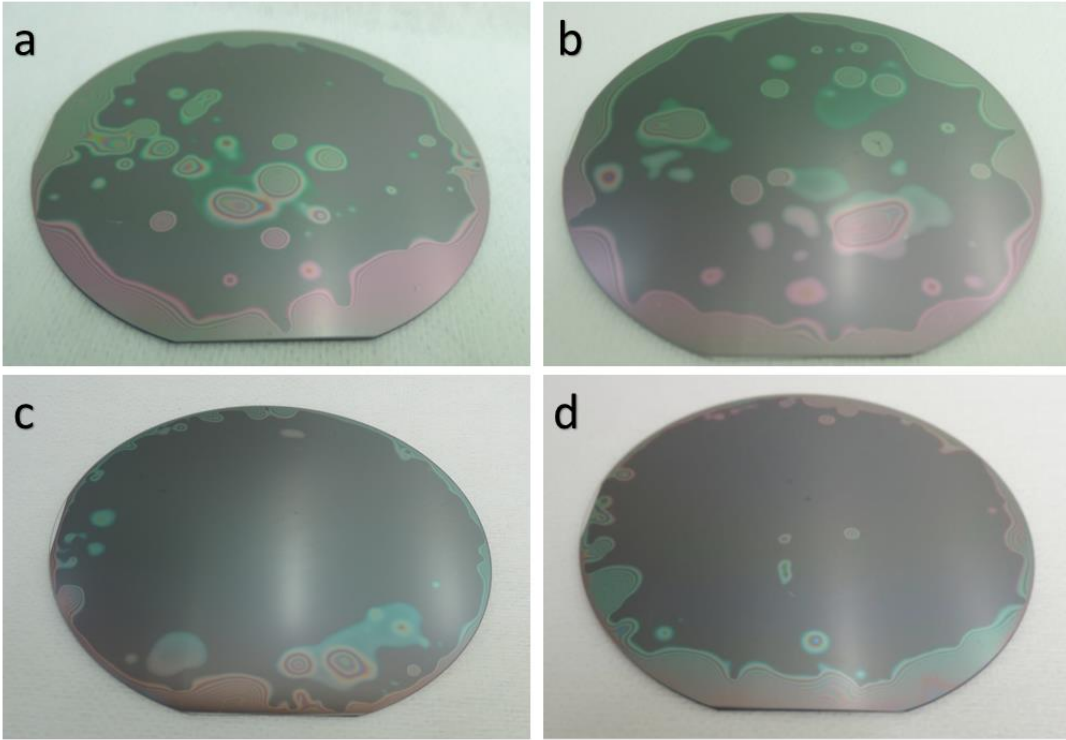
Figure 4.4 The resulting yields for a) the first b) the second c) the third and d) the fourth bonding trials.

In order to measure the bonding strengths of the four bonding trials, wafers were diced into 25 mm^2 square dies. Using a Dage 4000 Multipurpose Bondtester, a shear force is applied at an elevation corresponding to the top material's mid-thickness (650 µm). The force was increased gradually during the test until the wafers broke off. The maximum force just before the breaking was divided by the die area to calculate the shear bonding strength. The bonding strengths were measured between 13.75 MPa and 18.97 MPa. Table 4.1 lists the shear bonding strengths that are calculated for random dies around the bonded regions of the wafers. The strength measurement plots are given in Appendix B.

Table 4.1 Results of the shear force measurements for the trials and the average bonding strengths (in MPa).

Trial Number	1st Die	2nd Die	3rd Die	AVG.
1st Trial	10.7	20.2	18.5	16.4
2nd Trial	13.8	13.9	13.6	13.8
3rd Trial	18.2	16.5	-	17.4
5th Trial	18.1	19.9	-	18.9

The difference between double layer and single layer experiments could not be recognized from the measurements as also stated in [47]. Both conditions may equally be durable to tensile pulling and shear pushing forces. To coat the glass wafer would utilize hydrophobicity to the microfluidic channels, making the channel resistance the liquid see higher. In such a case, preventing liquid leakage from the resonator gaps is even more challenging for the CTC detection application. In addition, the interface of fracture was detected as the parylene-parylene bonding interface [48]. This is why it is decided to utilize the single intermediate layer parylene bonding for the fabrication of the resonators.

In order to inspect the effects at a higher temperature with a thinner intermediate layer, two additional experiments were conducted at 200ºC and 250ºC with 0.5 µm thin films coated on silicon wafers. This time, a 50ºC stepped heating was preferred and between each heating 5 minutes of vacuuming cycle was added. By doing so, it is aimed to eliminate the air trappings between the wafers. Even though the bonding recipe was adjusted for 1 mTorr vacuum pressure, it was observed that the chamber had been vacuumed down to 0.1 mTorr during the bonding process. The vertical piston force was 2000 N, and applied for 1 hour. The resulting yields for the fifth (at 200ºC) and the sixth (at 250ºC) bonding trials are shown in Figure 4.5 a) and b) respectively.
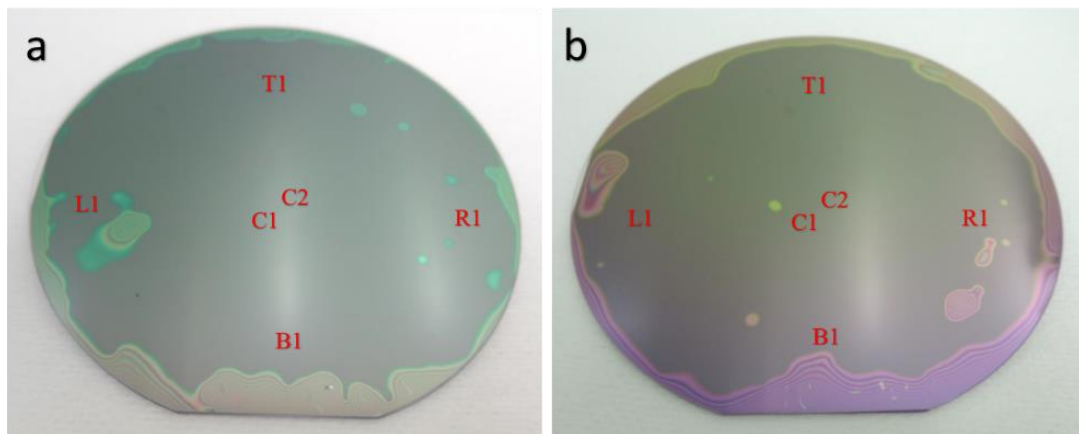
Figure 4.5 The resulting yields for a) the fifth bonding trial (single intermediate layer, at 200ºC) and d) sixth bonding trial (single intermediate layer, at 250ºC).

The yields are similar to the third and fourth trials. To compare the strengths, the wafers were also diced as 25 mm^2 dies. Figure 4.6 shows the shear force measurements during the strength tests for the sixth trial.
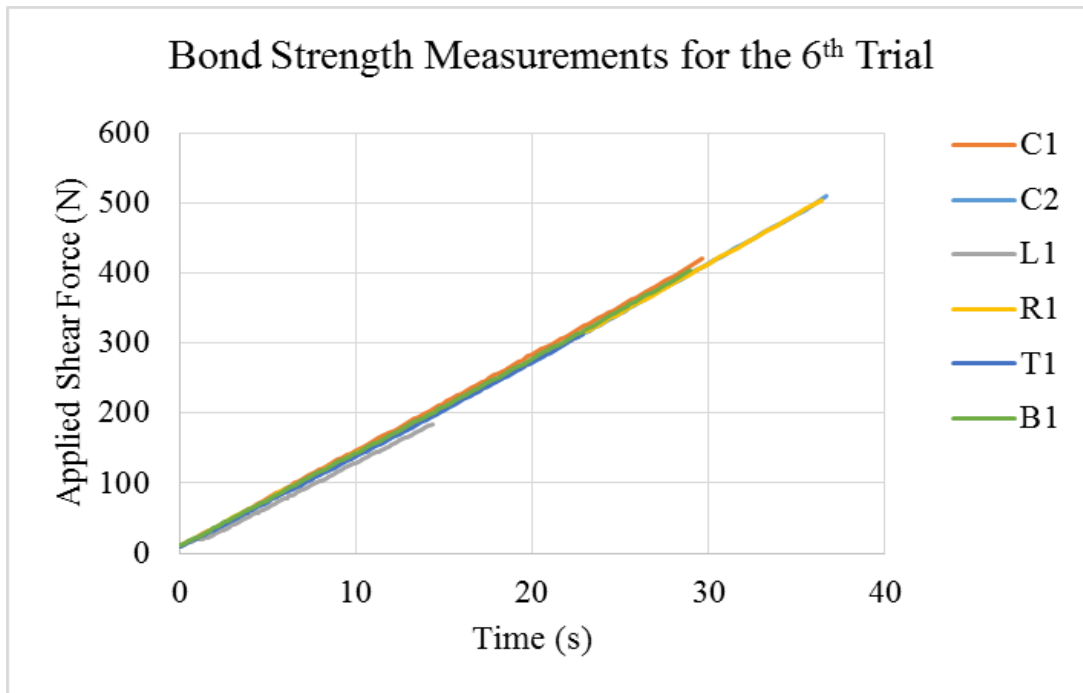
Figure 4.6 Shear strength measurements for the sixth bonding trial. Vertical axis shows the applied shear force until the die was broken. Horizontal axis shows the time it took before the die was broken.

The average bonding strengths were measured as 12.53 MPa and 15.58 MPa respectively for the fifth and sixth bonding trials. However, these include the dies from outer regions. In order to compare with the previous bonding trials, only the central dies can be taken into account. Table 4.2 lists the entire measurements in MPa from the fifth and sixth bonding trials. Notice that the place of the tested dies are shown on wafers in Figure 4.5. Although the central dies show similar strengths, the dies from the outer ring of the wafer differ in terms of the shear bonding strength for different temperatures. As the bonding temperature increases, the bonding gets stronger throughout the wafer from its origin to the outer edges. The change in color is most probably due to the difference in the final thickness of the intermediate parylene layers, and can be seen in Figure 4.5.

Table 4.2 Shear strength measurements on dies from the fifth and sixth bare bonding trials (MPa).

Trial	C1	C2	L1	R1	T1	B1	AVG.
5th Trial	19.2	16.9	9.3	8.5	11.8	9.6	12.5
6th Trial	16.8	20.4	7.4	20.2	12.5	16.1	15.6

Notice that, for all the bare bonding trials, the resulting shear strength deviates. This deviation is first due to the existence of defects at the bonding interface. Although number of such defects decreased with the optimizations, there was still some that could not be prevented, and decreased the bonding yield. Moreover, the bonding strength also deviates around the outer edges of the bonded wafers. This can be a result of the structure of the piston, applying vertical pressure during the thermal bonding.

Although the bonded wafers were characterized by their shear strengths during this thesis, it is still a good idea to compare the results with the literature, which had reported tensile strengths, and to comment on. A comparison of the shear bonding strengths with the literature is shown in Table 4.3. Only the average shear strength of the sixth bonding trial is compared because it will be used for the fabrication of the lateral gravimetric resonators from now on. During the bare bonding experiments, a promising strength and yield was achieved in order to propose a fabrication method for the lateral gravimetric resonators.

Table 4.3 Comparison of the measured bonding strengths with the literature (MPa).

Study	Technique	Details	Avg. Strength
This Study	Parylene to silicon	250ºC, 2000 N	**15.6, shear**
[43]	Parylene to parylene	230ºC, 800 N	3.6, tensile
[47]	Parylene to silicon	230ºC, 1000 N	2.4, tensile
[48]	Parylene to Pyrex	280ºC, 1000 mbar	8.8, tensile

4.3. Proposed Fabrication Method Utilizing Parylene Bonding

To solve the problems of the previous generation fabrications, which utilized anodic bonding, a new fabrication method based on parylene bonding is proposed. When compared to the previous generations, metal layers on the SOI active layer are completed via lift-off instead of wet etching techniques. This solves the risk of metal residuals before the DRIE structure-patterning step, which may cause needle-like silicon residuals on the active layer. In addition, anodic bonding is replaced with parylene bonding. Hence, the deposition of parylene is now controllable and selective etching is possible. Because of the additional insulating layer, unexpected short circuits due to silicon or metal particles are prevented. The metal layers do not diffuse

or burn because bonding takes place at lower temperatures and does not require high electric fields. In this section, details of the proposed fabrication method are explained.

4.3.1. Process Flow

Key steps of the proposed fabrication method are illustrated and briefly explained in Table 4.4. Lithography processes between the key steps are omitted in the illustrations of the process flow.

Table 4.4 Process steps of the parylene bonding based fabrication method for lateral resonators.

Step	Explanation	Cross-sectional illustration
S1	Metal (Cr/Au) patterning for bio-activation sites and electrical signal routings. Lift-off is preferred.	
S2	High-aspect-ratio DRIE structure patterning of resonators and silicon connection islands.	
S3	Parylene-C deposition (conformal) and selective etching of bioactive and contact sites by using RIE.	
G1	Metal (Cr-Au) sputtering and patterning for HF glass etching of microchannels. Wet etching is used.	
G2	HF glass etching of microfluidic channels and recesses; stripping of photoresist and metal masks.	
G3	Metal (Cr/Au) sputtering and patterning for electrical signal routings on glass.	
B1	Parylene bonding to integrate lateral gravimetric resonators and microfluidics. Wafers have to be aligned well before the bonding.	
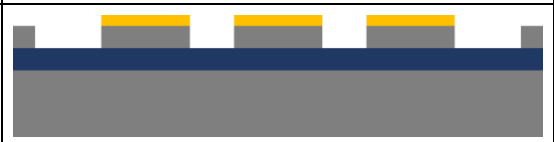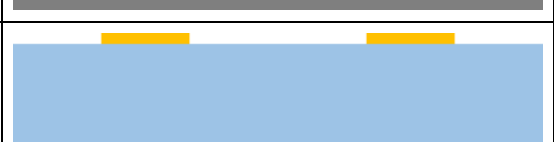
60
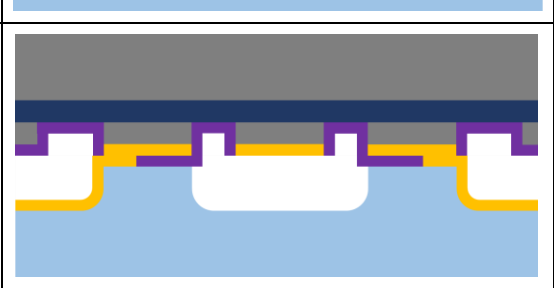
Table 4.4 – *continued*. Steps of the proposed fabrication method for lateral gravimetric resonators.

B2	Removal of the handle Si wafer of the SOI and wet etching of buried oxide. Parylene membrane formation is shown with the red-dashed circle.	
B3	Plasma removal of membranes. RIE is preferred because it is anisotropic. Caps on channel inlets and contact pads are detached from dies after dicing.	
	Silicon Oxide Cr-Au Parylene Glass	
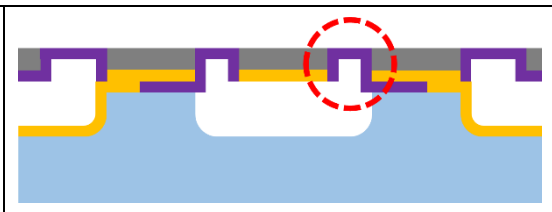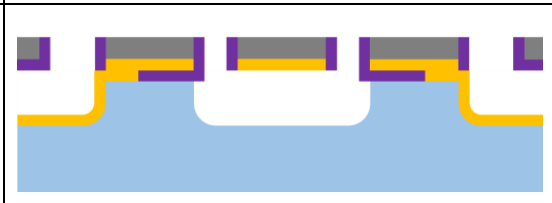
As in the previous generations, fabrication starts with metallization of the SOI and glass wafers (30 nm Cr and 300 nm Au). Both wafers are processed in parallel until the bonding step. For the SOI wafer, lift-off is used because any metal residue causes needle-like silicon residuals on the active layer, which may short-circuit the electrical routings after the fabrication (S1). Diffused Au layer cannot be completely etched by using wet etching. The bio-activation sites and electrical routings on the SOI active are shown in Figure 4.7.
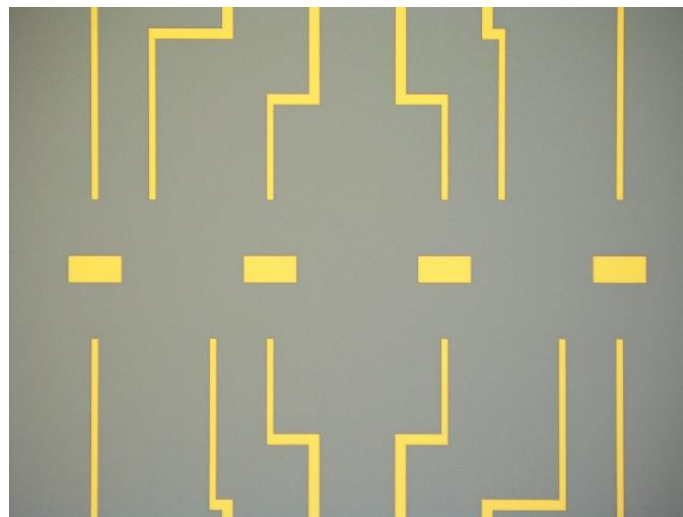
Figure 4.7 Metal bioactive sites and electrical signal routings on the SOI just after the lift-off step.

DRIE (Bosch process) is used for high-aspect-ratio etching of the resonators (S2). This is crucial in order to have orthogonal gaps and parallel capacitive plates between the resonator and actuation/sensing electrodes. A photoresist layer is spin-coated and

61

patterned for masking the DRIE plasma. Optical microscope image of patterned resonators and the silicon connection islands can be seen in Figure 4.8.
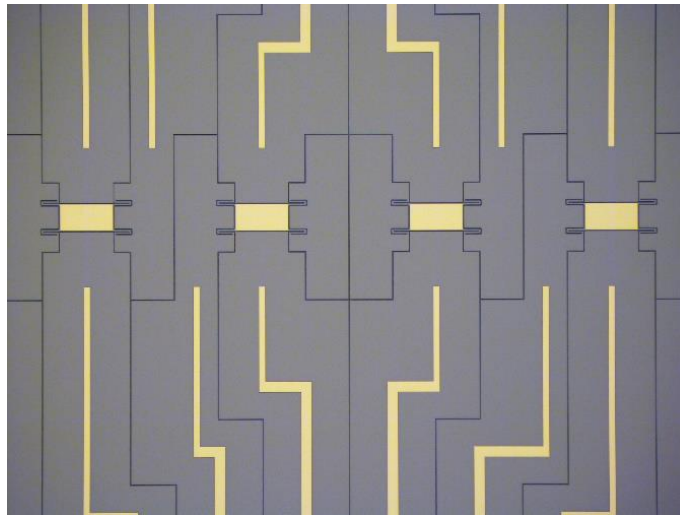
Figure 4.8 Lateral resonators and silicon connection islands are structured using DRIE dry etching process.

Parylene layer on the bio-activation sites and the contact sites (for connecting the electrical routings on the SOI and glass layers) is etched using RIE (S3). The timing is optimized for the parylene thickness although it is not crucial in this step. Metals and silicon substrate stops the plasma etching. Parylene openings are shown in Figure 4.9.
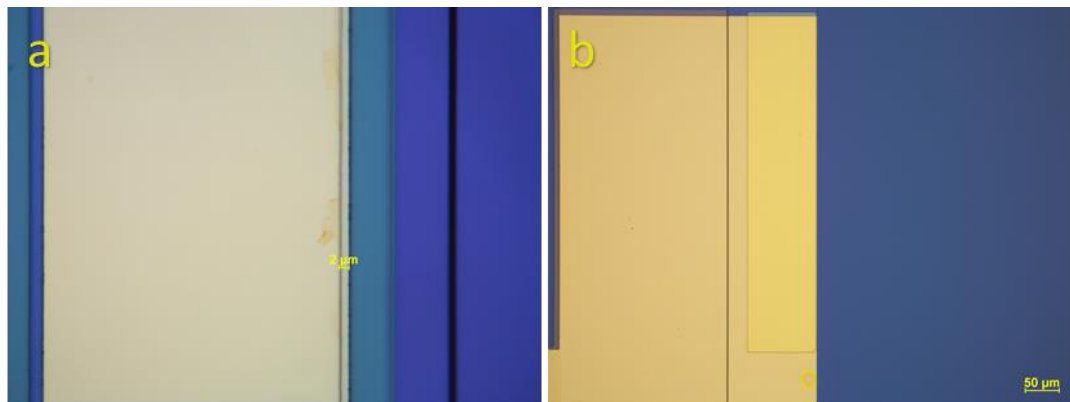
Figure 4.9 RIE is used to open the bio-activation metals (a) and the contact regions of the signal routing metals (b). The thin layer of polymer can be seen around the etched regions on (b) since light refracts.

Glass wafer is processed using exactly the same procedures as in the last generation fabrication method (G1-G3). The duration of the HF etch determines the channel heights. Because spin coating is not possible after channel etching, spray coating is

used to pattern the metal routings on the glass wafer. Because UV light cannot penetrate into the resist layer around the channel corners, a thin metal layer resides even after over-etching. Figure 4.10 shows the microfluidic channels and recesses that are etched on a glass wafer. The metal residuals can be seen around the edges and corners of the etched trenches.
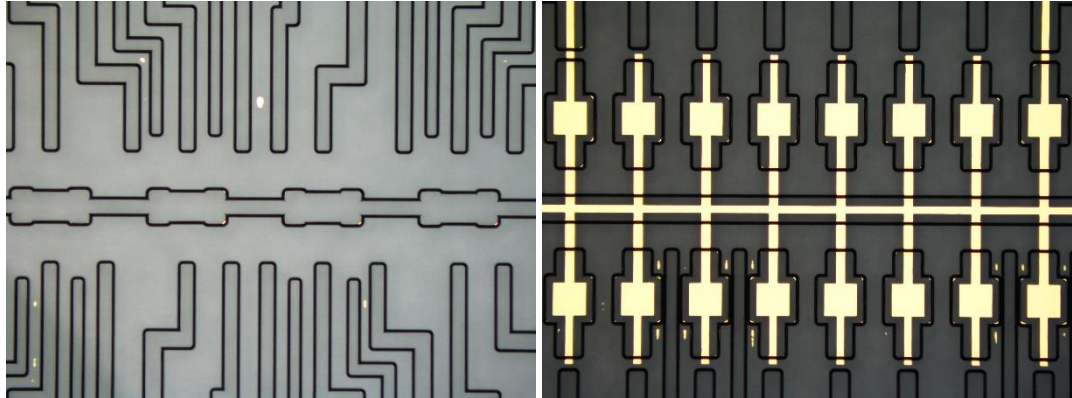
Figure 4.10 Processed glass wafers. Microfluidic channels/recesses and pad routing metals are shown.

Processed SOI and glass wafers are integrated using thermal bonding of the intermediate parylene layer (B1). The bonding chamber is vacuumed down to 1 mTorr during the 50ºC stepped heating of the chamber up to 250ºC. Between each heating step, the chamber is vacuumed for 10 minutes. Then, piston applies 1000 N vertical force on the aligned wafers for 1 hour. Finally, the chamber cools down to the room temperature. The detailed bonding recipe is given in Appendix C.

After the bonding, the silicon handle wafer of the SOI should be thinned and etched away. For the thinning, grinder can be used for the first few hundred micrometers instead of DRIE processing. Alternatively, one can thin and etch away the whole handle wafer using just the DRIE (B2). Then, the buried oxide is etched by using 1:5 BHF and the resonators are released after a standard acetone-IPA-methanol releasing procedure (B3).

Figure 4.11 shows a parylene-bonded wafer after the releasing step. Some of the active silicon layer of the SOI are broken because of the stressed oxide layer as can be seen. The optical microscope images of the microfluidics-integrated resonators photographed from the silicon side and the glass side are shown in Figure 4.12 and Figure 4.13 respectively.
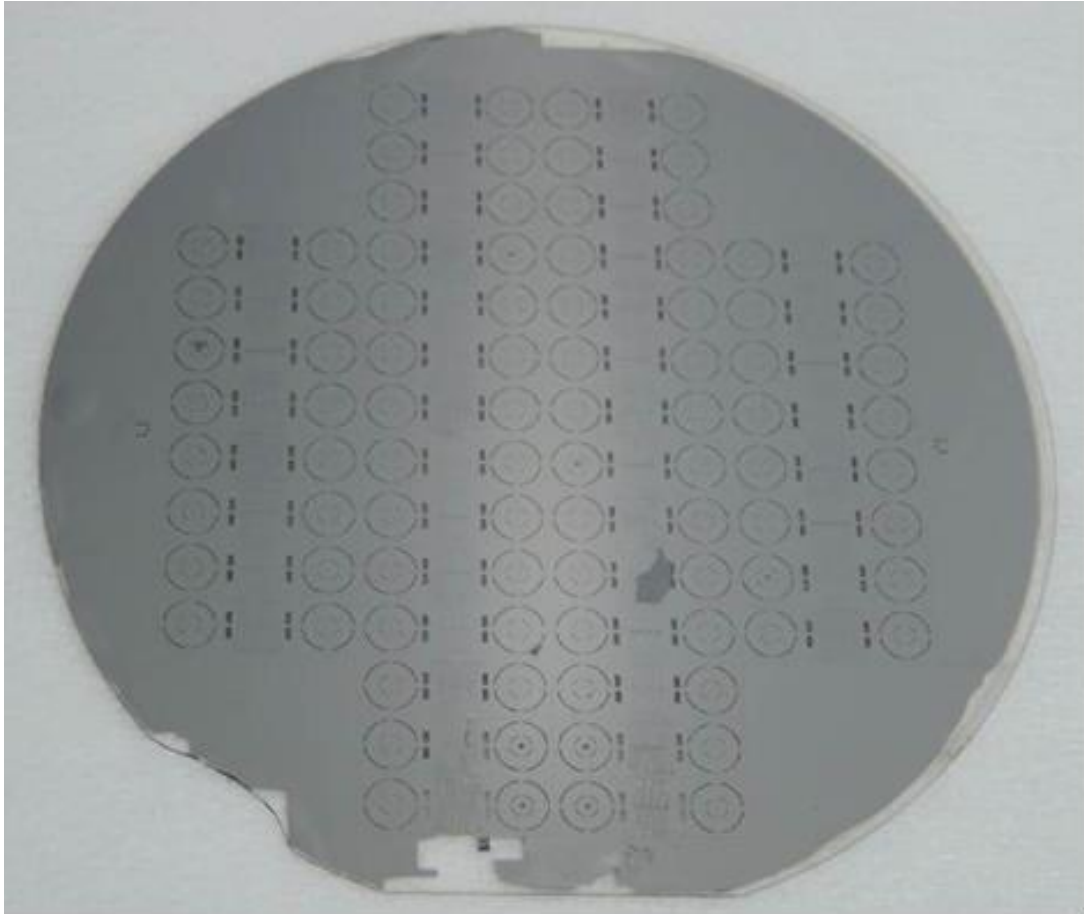
Figure 4.11 A parylene-bonded pair of SOI and glass wafers. On the SOI, lateral gravimetric resonators and channel inlet/outlets are structured using DRIE. On the glass, microfluidic channels and recesses are etched. Some parts of the active Si are broken during the DRIE etching.
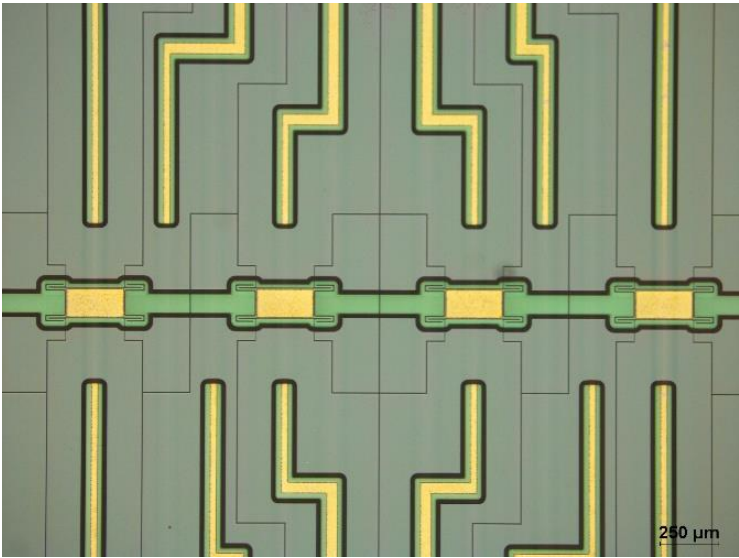
Figure 4.12 A resonator set and the microfluidic channel. Image was taken through the glass side.
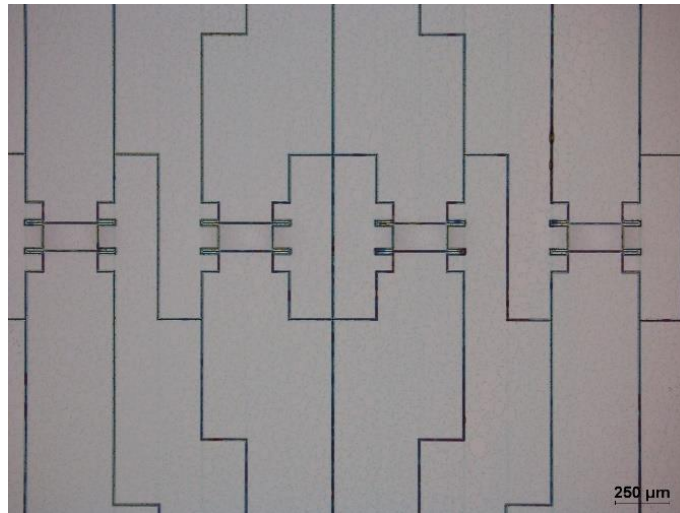
Figure 4.13 The same resonator set in Figure 4.12. Taken from the silicon side of the bonded wafer pair.

4.3.2. *Effects of Membrane Formation*

One disadvantage of parylene bonding is that during release, parylene membranes form between all the resonator gaps (B2). These membranes may increase the effective spring constant in each direction and disturb the mode of resonance. In order to predict its effects, the membranes were modelled between the gaps of R#1 (35 μm thick RCGS#2) via COMSOL Multiphysics by using Electromechanics interface. For simplicity, bio-activation metals and parylene coating on the resonator other than the membranes were not included in the model. It was solved for Eigen frequencies. The membranes and resonator were modelled as 0.5 μm and 35 μm thick respectively. No lateral resonance mode but torsional ones were observed. Moreover, as the size and location of the membranes change, the resonance frequency shifted proportional to the size.

Existence of a membrane between the gaps introduces additional spring to the system. This additional spring disturbs the symmetry in the model and cause the torsional movement even if the actuation is in the lateral direction. The simulation results for the excited resonance modes (Eigen frequencies) are shown in Figure 4.14.

In order to eliminate the mode-disturbing effect of parylene membrane formation, the formed membranes should be etched after the releasing step. To do so, an additional plasma etching can be used. Either isotropic oxygen plasma or anisotropic plasma such

65

as RIE or ICP can be preferred. In order to protect the hydrophobic layer preventing the liquid leakage, a directional process should be chosen, which is RIE or ICP. Previously, Temiz *et al.* reported a similar process to isolate the layers during the 3D integration via TSV [66]. RIE can be used without any mask after the releasing step.

Eigenfrequency=1.5935E6   Surface: Total displacement (µm)
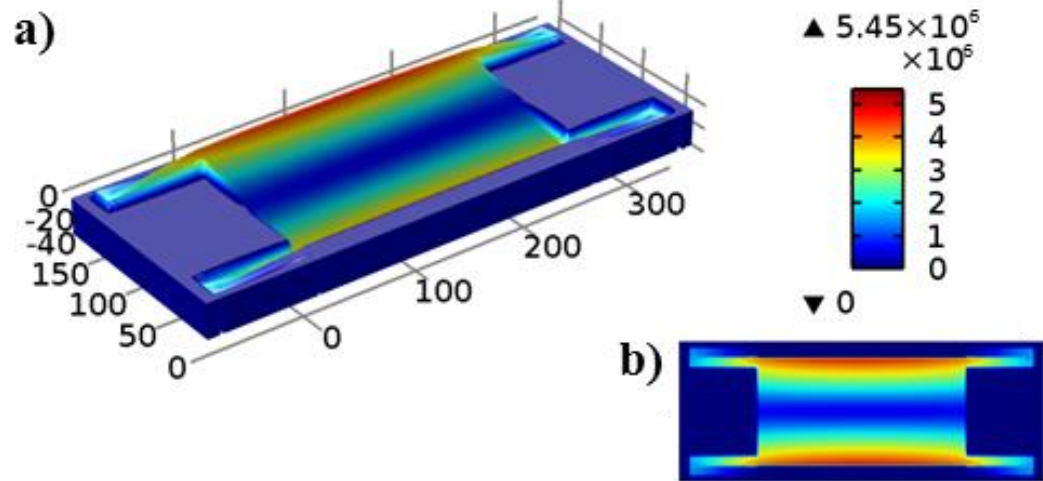
Eigenfrequency=6.2677E5   Surface: Total displacement (µm)
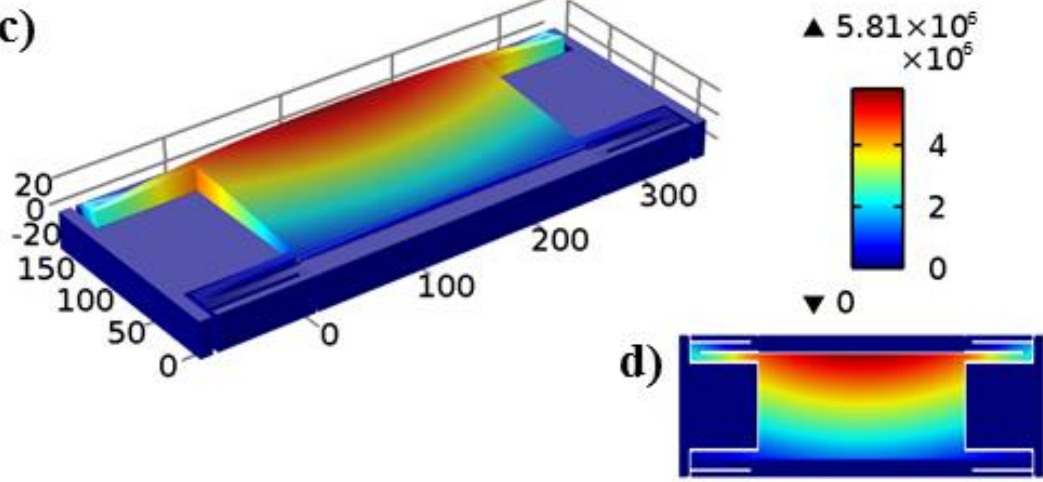
Figure 4.14 The excited natural resonance modes for two different membrane formations (0.5 µm). Both of the modes are torsional, and the motion is mostly out of plane. The membranes cover a), b) all the gaps and c), d) only one of the capacitive gaps (between the actuation electrode and the proof mass).

The optical microscope images show the membrane formation between the silicon blocks in Figure 4.15. The parylene membranes between the gaps seem greenish

because of refraction of the light. The membranes were also imaged by using SEM for further inspection as can be seen in Figure 4.16 and Figure 4.17.
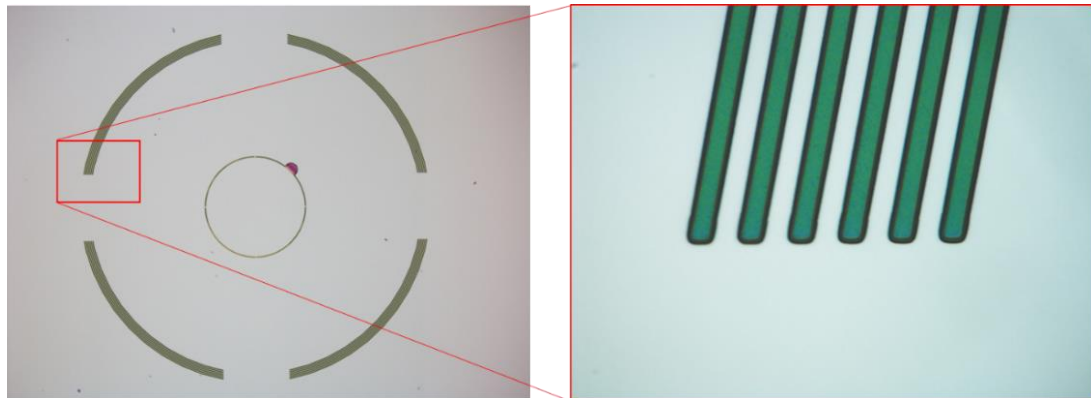
Figure 4.15 Optical microscope image of a microfluidic channel inlet. Parylene membranes between the silicon blocks are colorful and seem green because the light is refracted by the polymer layer.
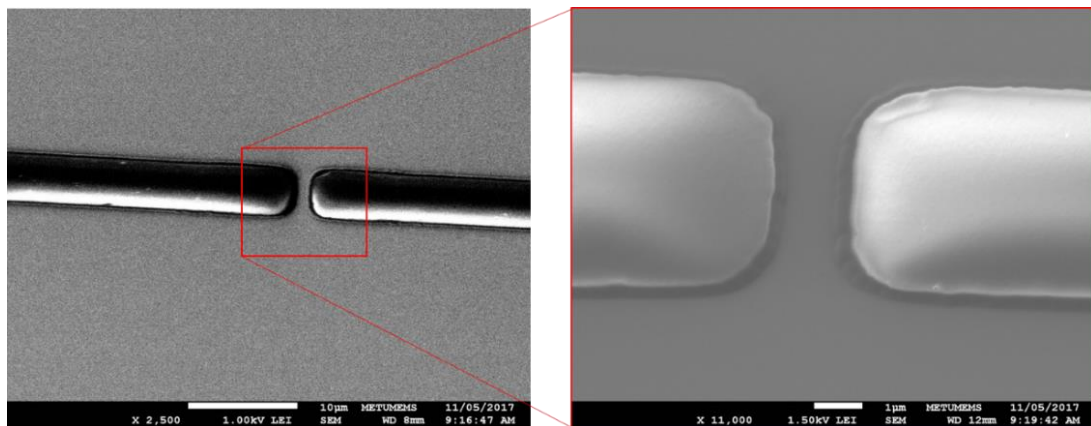
Figure 4.16 Parylene membranes between the silicon blocks shine in SEM images because of charging. The zooned image clearly shows that the parylene membranes are buckled up due to stress of the oxide.
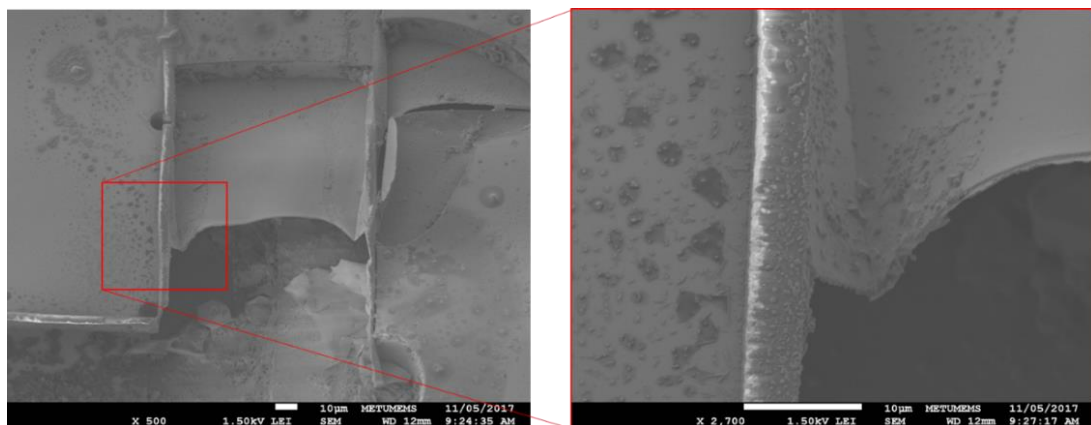
Figure 4.17 SEM image of a broken wafer. The membranes shine in both images. Because some silicon blocks are broken, the intermediate parylene layer and the sidewall coatings can also be seen.

67

After the RIE plasma etching of the membranes, optical microscope and SEM images of the gaps between the silicon blocks revealed that the membranes could be completely etched by an optimized RIE process. As shown in Figure 4.18, some membrane residual may exist after the RIE between the gaps if the process is not optimized for the thickness.
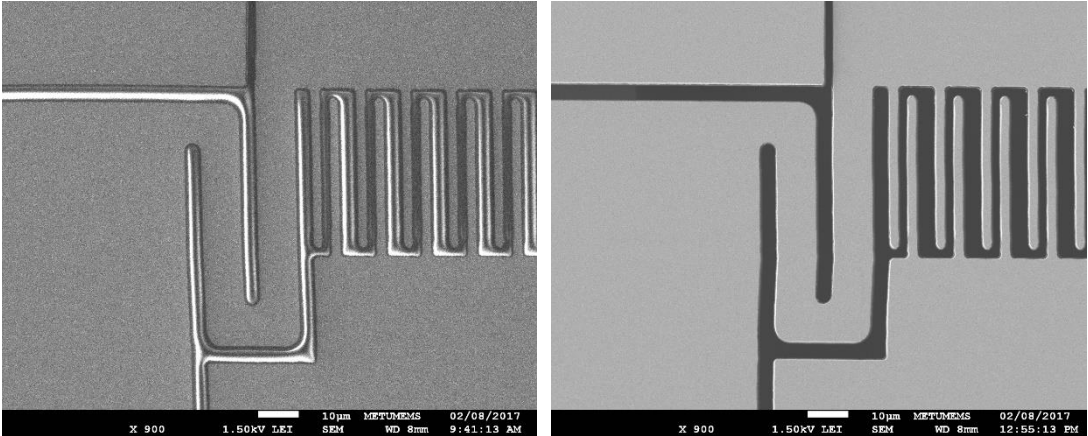
Figure 4.18 After parylene RIE, membranes were mostly eliminated throughout the parylene-bonded wafer. Before and after RIE of parylene membranes can be seen in the left and right SEM images respectively.
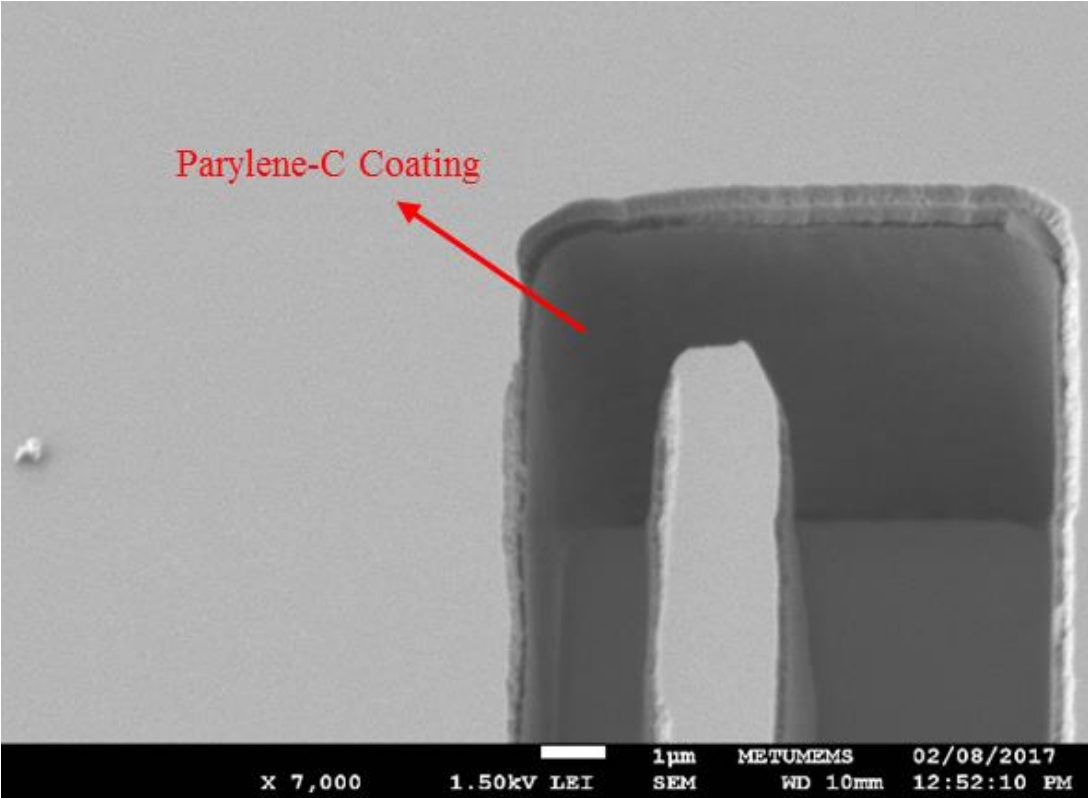
Figure 4.19 Sidewall coatings were not damaged during the RIE etching because it is highly directional.

A close-up SEM image in Figure 4.19 shows that the parylene sidewall coatings are protected during the RIE step for etching the membranes. The walls of the resonator are coated with the polymer. This ensures that the hydrophobicity will stay and liquid will not leak from the resonator gaps during the flow. The capacitance between the proof mass and electrodes increases. However, the gap becomes narrower; damping effects become more effective. Hence, the thickness should be optimized for the Q.

4.4. Summary

This chapter has started with a summary of the previous generation, anodic bonding based fabrication methods, addressing all the advantages and disadvantages of anodic bonding. The last generation process flow used by Töral [42] and Kangül [38] has been given and specific problems were discussed. Then, parylene bonding has been proposed as a solution to all addressed problems by stating all its advantages over anodic bonding. Parylene as an intermediate bonding layer has been discussed with a focus on specific needs of cell detection applications. The results of bare silicon to glass parylene-bonding trials have been given and compared with the previously reported results in the literature. Finally, a modified fabrication method utilizing parylene bonding has been proposed with a detailed process flow, and optical microscope and SEM images from fabrication of the resonators. Final form of a die, and microscope image of the resonators and microchannels are shown in Figure 4.20.
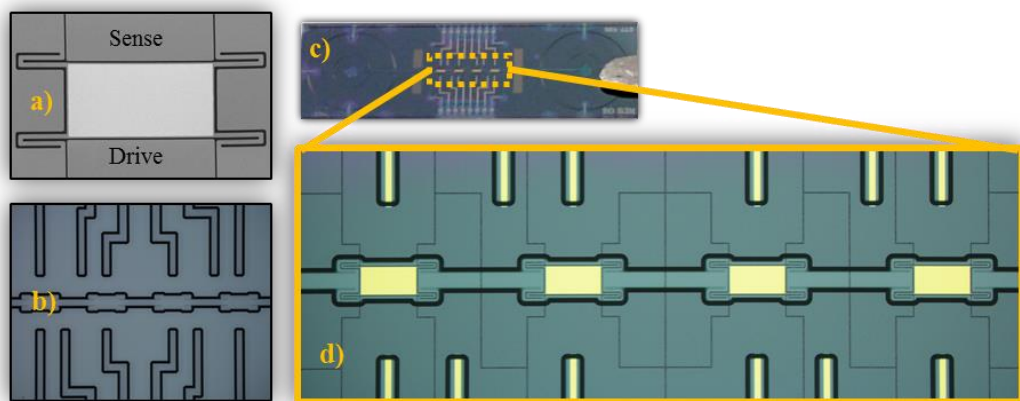
Figure 4.20 a) SEM image of R#1, b) microfluidic channels and recesses, c) one of the fabricated resonator dies and d) optical microscope image of the microfluidic-integrated lateral resonators.

69

CHAPTER 5

CHARACTERIZATION OF THE RESONATORS

This chapter presents the characteristics of the resonators, which were fabricated by using the proposed parylene bonding based method. In Section 5.1, the experimental test setup is introduced. Section 5.2 presents the in-air resonance characteristics of the fabricated devices one by one. Furthermore, the effects of parylene membrane formation are also shown experimentally. By using one of the fabricated resonators, mass of a micro-bead was weighed. Section 5.3 summarizes the experiment, and provides the comparison of calculated and measured mass sensitivities of the resonator. Finally, the liquid flow test results through the integrated microfluidic channels was given in Section 5.4.

5.1. Test Setup
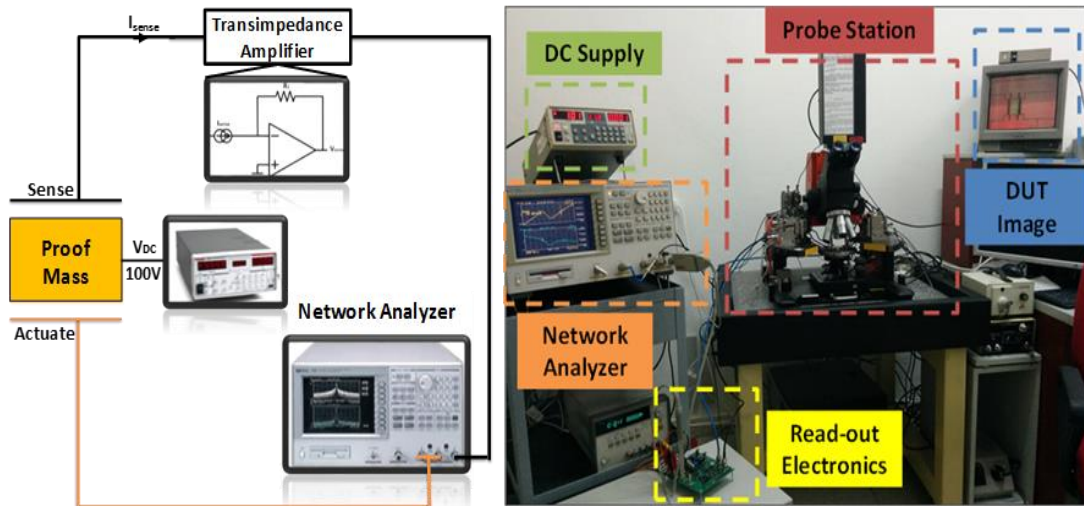
Figure 5.1 The experimental setup and schematic of the readout electronics used for measurements [67].

In order to actuate the resonators, and to sense the oscillation characteristics a dedicated experimental setup was used. The actuation signal was inputted from a network analyzer, which provides harmonic signals up to 15 dBm. A high voltage

supply was used to charge the proof mass and the read-out electronics were powered up by a DC voltage supply. In order to route the actuation, sensing and proof mass contacts, a probe station was used. The network analyzer recorded the frequency response of the device under test (DUT) while scanning a frequency range of interest, which includes the resonance frequency. The sensing current was amplified using a trans-impedance amplifier (TIA) and an active probe (1 MΩ). At the resonance frequency, depending on the quality factor of the resonance, a sharp or gradual peak in the magnitude response is seen. The experimental test setup is shown in Figure 5.1.

The read-out electronics was implemented using a TIA as explained in Section 2.2.1. In order to eliminate the feedthrough current, the crosstalk recordings between the actuation and sensing electrodes when there was no actuation were subtracted from the resonance characteristics. This method is equivalent to using a dummy resonator for differential sensing that is explained in 2.2.2 although it requires post processing of the resonance data. Notice that, in order to decrease the crosstalk, the probe station chuck, the interface electronics, the network analyzer and the DC supplies were common-grounded.

5.2. Resonance Characteristics

Frequency responses of the fabricated resonators were measured in air in order to detect their dry resonance characteristics. First, the proof mass was charged by applying 80 V so that it can displace with the AC actuation (0 dBm). The displacement current was recorded in the polar form for a frequency range including the resonance frequency. However, this recording includes the crosstalk between the actuation and sensing electrodes, and from the experimental setup itself. Then, as a result, the recording was repeated after the proof mass was grounded. In this way, the oscillation of the proof mass was prevented. This effect is also shown in Eq. (2.1-17). Grounding the proof mass makes the actuation force zero. Thus, the second recording only has the crosstalk. The feedthrough-free resonance characteristics can be plotted by subtracting the crosstalk data from the resonance recordings. All the results presented in this chapter were processed similarly, to eliminate the feedthrough current effects.

5.2.1. Effects of Parylene Membrane Formation

In order to examine the effects of the parylene membrane formation, a set of 35 μm thick RCGS#2 (R#1) were fabricated by using the proposed parylene bonding based fabrication method. However, the final step; i.e. RIE etching of the membranes (B3), was intentionally skipped. One of the resonators were characterized by using the explained test setup. No resonance was recorded around the expected resonance frequency. Thus, a larger frequency range was scanned. A resonance around 840 kHz was detected and recorded. The magnitude and phase responses of the characterized resonator are given in Figure 5.2. The resonance frequency and the quality factor were 839.6 kHz and 139.4 respectively. The result is in agreement with the claim in Section 4.3.2, which is the fact that the resonance frequency increases with the total size of the membranes between the resonator gaps. The increase in the resonance frequency is a sign of mode disturbance. In other words, a torsional movement was introduced with the existence of the membranes.
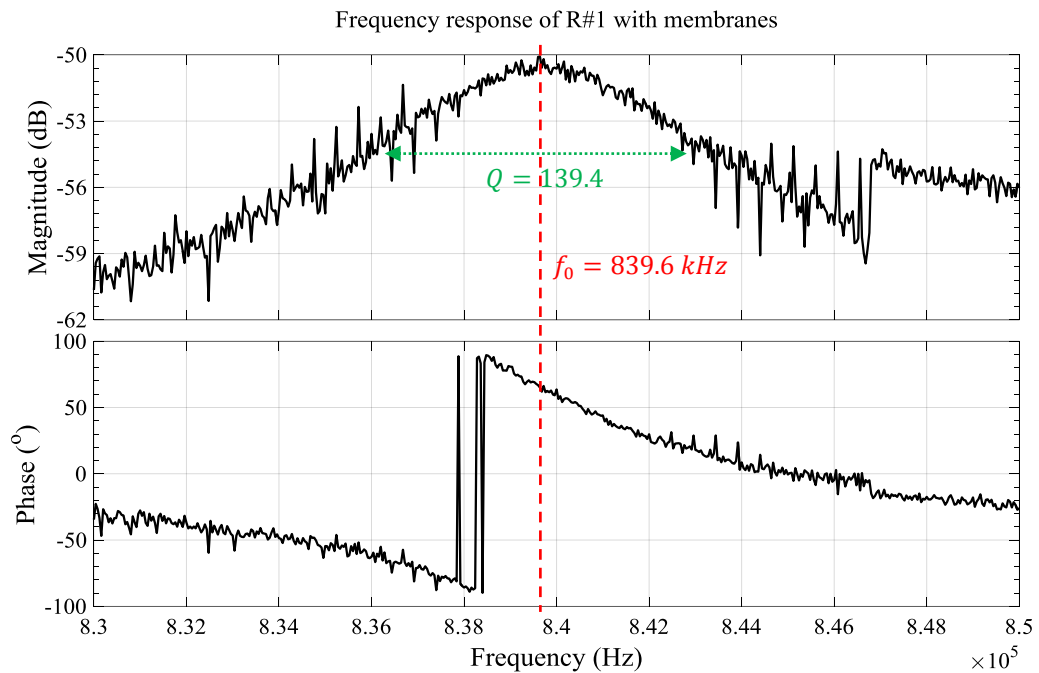
Figure 5.2 Magnitude and phase responses of R#1 before the formed parylene membranes being etched. The resonance frequency and the Q-factor are 839.6 kHz and 139.4 respectively [49]. The measurement is a bit noisy probably because of the membranes between the resonator gaps.

73

Notice that the increase in the resonance frequency and the mode disturbance are in parallel with the simulation results given in Section 4.3.2. In order to prevent the disturbance and to get the expected lateral resonance characteristics, the membranes had to be etched. The sidewall coatings should be protected in order to prevent liquid leakage into the resonator gaps during operation under a liquid flow through the micro-channels. In Chapter 4, it is already shown that RIE plasma etching can be used for removing the membranes without damaging the sidewall coatings.

5.2.2. *Etching the Membranes*

In order to etch the membranes, isotropic O_2 plasma was applied to the characterized resonator (R#1) without using any masks. After the membranes were etched, the characterization was repeated with the same resonator. The frequency response is plotted in Figure 5.3. The resonance frequency is 283.4 kHz, which is very close to the analytical calculations and the simulation results. The quality factor was calculated as 173.1.
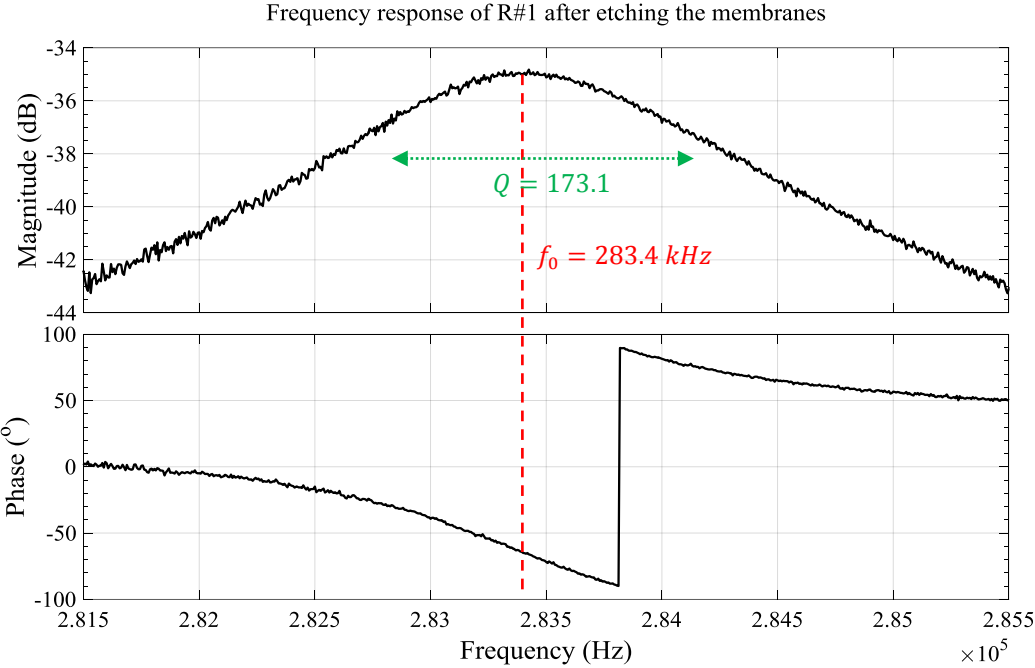
Figure 5.3 Magnitude and phase responses of R#1 after the membranes were etched by using isotropic O_2 plasma. The resonance frequency and the Q-factor are 283.4 kHz and 173.1 respectively [49].

74

5.3. Mass Sensing

One of the most important performance parameters is the mass sensitivity of the resonator for cell detection applications. In order to compare the performance of the fabricated resonators, a 10 µm thick RCGS#2 (R#2) was fabricated. When there was no attached mass, the resonance characteristics were recorded as a reference. The magnitude and phase responses in air are plotted in Figure 5.4. The reference resonance frequency was recorded as 258.05 kHz, which is similar to both the analytical calculations and FEM simulations. The quality factor was calculated as 430.1, which is very close to the simulation results.
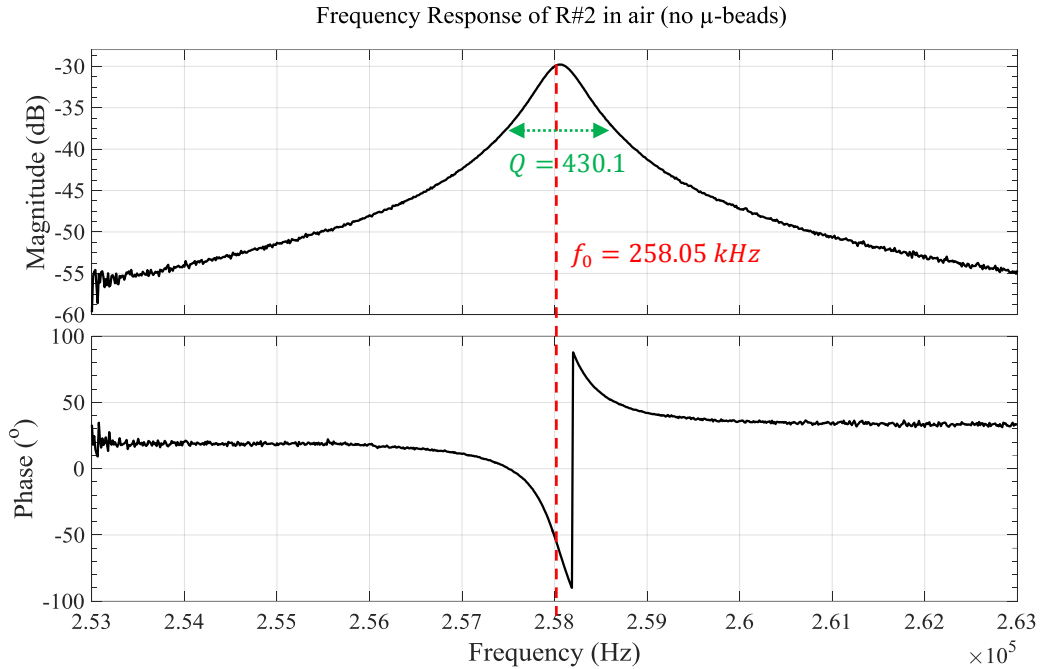
Figure 5.4 The reference frequency response of the R#2 for lateral gravimetric mass sensing experiments. The resonance frequency is 258.05 kHz and the quality factor is 430.1.

Mass sensitivity is the ratio of the minimum detectable mass to the minimum detectable frequency shift. In order to calculate the mass sensitivity, Eq. (2.1-34) should be divided by Eq. (2.1-33). The theoretical mass sensitivity can be estimated as in Eq. (5.3-1):

$$(\nabla m / \nabla f)_{min} \approx 2m/f_0 \qquad (5.3\text{-}1)$$

The theoretical mass sensitivity for R#1 was calculated as 5.89 pg/Hz by substituting the mass of the proof mass and the measured resonance frequency. During the calculations, the fabrication errors and the mass of the spring beams, parylene and metal coating were ignored for simplicity.

For the mass-sensing experiment, a 10-µm bead (Polysciences Polybead® Dyed Yellow Microparticles) was loaded on the proof mass by using one of the probes of the probe station. First, 35 µl of diluted µ-bead solution was dropped on the resonator die. After the drop evaporated, one of the µ-beads on the Si surface was loaded on the proof mass using the probe manipulator. The mass of a µ-bead was calculated as 788 pg for a mean radius of 5.6 µm. The mean radius value was taken from the package information. Figure 5.5 shows the resonator before and after the µ-bead was loaded.
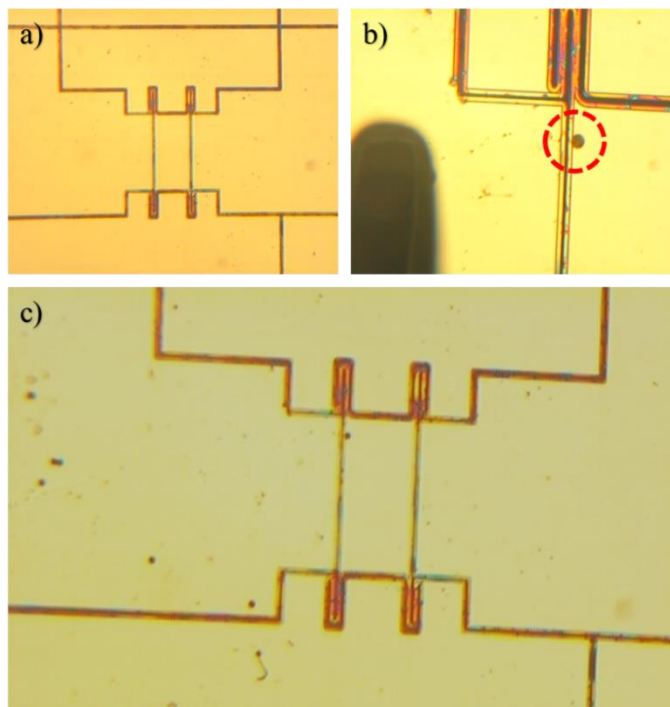
Figure 5.5 a) The resonator (R#1) used for the gravimetric mass sensing experiment, b) Loaded µ-bead on the proof mass and the probe needle that is used to move the µ-bead, c) the resonator (µ-bead loaded).

After the µ-bead was loaded, the resonance characterization was repeated to record the shift in the resonance frequency. The magnitude and phase responses of the resonator with a µ-bead loaded on it are plotted in Figure 5.6. The resonance frequency was recorded as 257.90 kHz, implying a decrease in the resonance frequency as expected. The quality factor was calculated as 429.8, which is almost equal to the unloaded case.

As the damping due to the µ-bead binding is not significant in air, this was also an expected result. However, if a µ-bead or a cell is attached to the proof mass under a liquid flow, the damping will decrease the quality factor as estimated in [14].

Frequency Response of R#2 in air (1 µ-bead loaded)
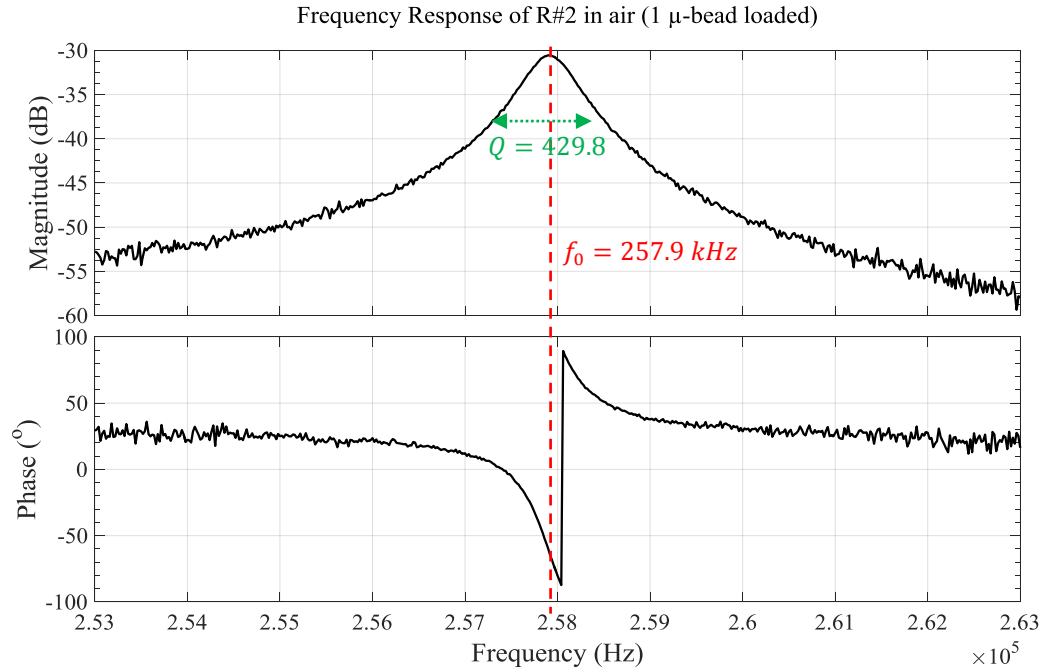
Figure 5.6 The requency response of the R#2 after the immobilization of 1 µ-bead. The resonance frequency is 257.90 kHz and the quality factor is 429.8. There is a decrease of 150 Hz in the frequency.

Frequency shift in resonance frequency due to attachment of the µ-bead
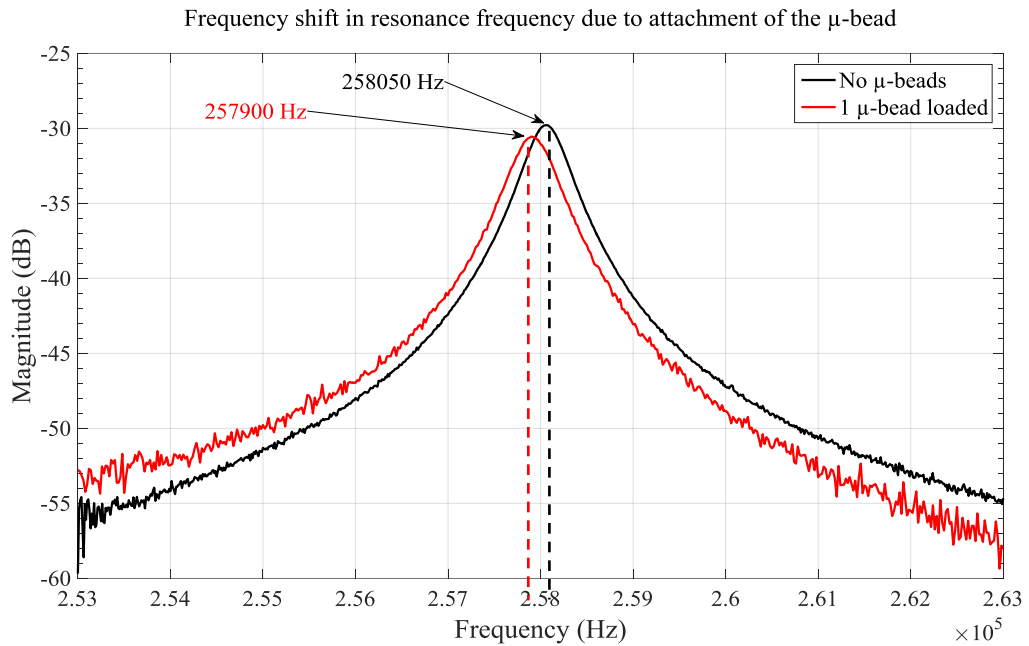
Figure 5.7 Comparison of the magnitude responses of R#1, before and after the µ-bead was loaded.

77

The measured mass was calculated as 883.5 pg by multiplying the calculated theoretical mass sensitivity with the shift in the resonance frequency. The difference is not only due to the ignored mass and due to fabrication errors during calculation of the mass sensitivity, but also because of the deviation in the diameter of the μ-bead. The comparison of the magnitude responses for the unloaded and loaded cases is plotted in Figure 5.7.

5.4. Liquid Flow Tests
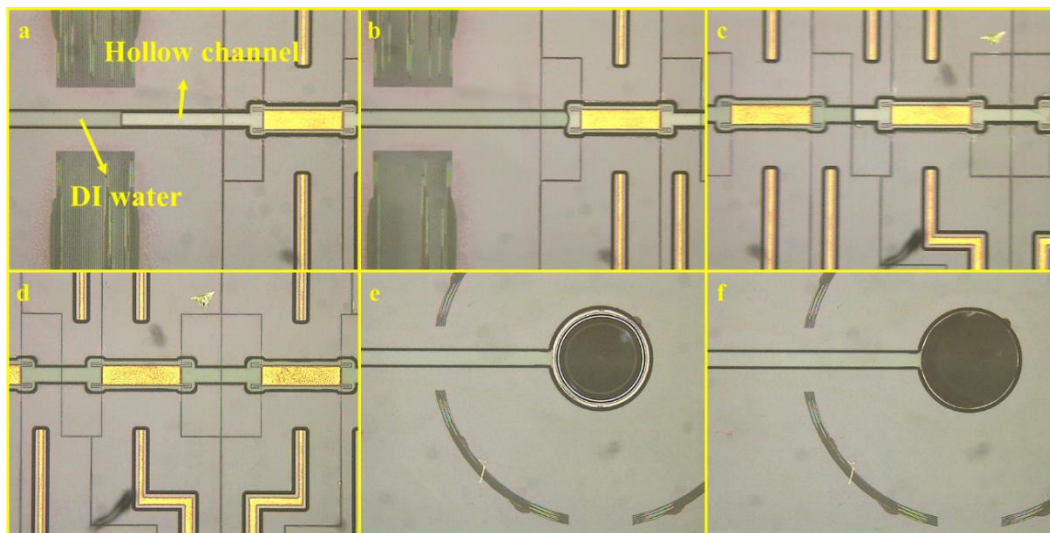
Figure 5.8 Snaps taken from the liquid flow test recordings. a) Laminar flow was observed as expected. b,c) Flowing DI water stops for a while at each DRIE trench. d) There is no leak observed inside the microfluidic channel. e) The outlet of the microfluidic channel before and after it was filled with the DI water. The images were recorded through the glass side of the die using an inverted microscope.

In order to test the liquid flow, DI water was pumped into the microfluidic channel of one of the fabricated resonator dies (0.5 μl/min). A LabSmith syringe pump and a fused silica tubing were used to adjust the flow rate and to connect the microfluidics. Laminar flow characteristics were observed during the filling of the channel and liquid flowing. The flowing liquid stopped at each DRIE trench on the Si channel wall, acting similarly as the passive microfluidic valves. Throughout the filling of the channel and the continued flowing, no leakage from the channel walls and the resonator gaps was observed. This implies that the parylene bonding could be used to integrate micromechanical systems with microfluidics. Snaps taken from the recordings during the filling of the microfluidic channel are given in order in Figure 5.8. DI water and

the hollow channel are marked as a guide for eyes to understand the flow characteristics. Notice that the resonator has a different proof mass length than RCGS#2 although the width and thickness are the same.

5.5. Resonance Characterization under a Liquid Flow

In order to record the resonance characteristics when there is liquid inside the microfluidic channel, the measurements were repeated for the liquid-filled sample. The flow was stopped intentionally due to limitations of the used experimental setup. No resonance peaks were observed neither around the expected frequency nor for a wider frequency range because the response was noisy. The fluid not only increases the capacitive feedthrough with its dielectric constant larger than that of the air, but also introduces a resistive feedthrough current. The feedthrough current and the additional noise suppress the output current of the sensor, making sensing even more challenging. To get the resonance, the second harmonic characterization method can be used to eliminate the feedthrough and noise in the fundamental tone. In addition, the resonator designs can be updated to provide larger current output with a decreased capacitive feedthrough.

5.6. Summary

In this chapter, the characteristics of the parylene-bonded lateral gravimetric resonators are presented. The effects of parylene membranes on the resonance characteristics, which are also inspected with simulation modules in Chapter 3, are experimentally recorded and compared with the simulation results. Then, as a proof of concept, weighing of a commercial μ-bead and comparison with the expectations are shared and done. The measured resonance frequencies and quality factors for R#1 and R#2 are compared with the analytical expectations and the simulation results is given in Table 5.1.

Table 5.1 Comparison of the measurements with the calculations and simulation results.

ID	Analytical	Simplified FEM	Detailed FEM		Measurements	
	f_0	f	f	Q_{air}	f	Q_{air}
R#1	285.5 kHz	300 kHz	285.2 kHz	140	283.4 kHz	173.1
R#2	265.5 kHz	299 kHz	261.1 kHz	403	258.1 kHz	430.1

The liquid flow through the microfluidic channels and resonance characterization under a liquid flow are discussed. It is concluded that the fabricated sensors are ready for operation under liquid flow; however, enhancements should be performed in order to suppress the resistive and capacitive feedthrough currents and to detect the sensing (output) current of the resonators. Specifically, the second harmonic characterization method could enhance the elimination of the feedthrough and the resonators should be redesigned to increase the current gain that is proportional with the displacement of the proof mass.

CHAPTER 6

CONCLUSIONS & FUTURE WORK

The main objective of this study is to develop a novel fabrication method utilizing parylene bonding for fabricating lateral gravimetric resonators that are integrated with microfluidics in order to enable real-time rare cell detection applications.

The research performed and the findings in this thesis can be summarized as follows:

- Parylene bonding has been selected and studied as an alternative to anodic bonding, which has been used to fabricate lateral gravimetric resonators previously. The thermal, chemical and dielectric properties of parylene have been inspected. Parylene-C has been preferred as intermediate bonding layer because it is chemically inert, becomes thermoplastic (adhesive) at lower temperatures and shows stable dielectric performance.

- Several experiments showed that parylene bonding is suitable for fabricating robust, microfluidic-integrated micromechanical structures. However, there are several void sources such as air bubbles and dust when compared to anodic bonding. Eutectic configuration has been used to perform parylene bonding. This might cause inefficient heating of the polymer, decreasing the bonding quality especially around the outer edges for the bonded wafer. In order to heat the polymer more efficiently, microwave heating could be preferred.

- A novel method utilizing parylene bonding has been proposed for fabricating lateral gravimetric resonators by modifying previously used anodic bonding based methods. One major disadvantage of the proposed method is the formation of membranes between the resonator gaps, which causes torsional oscillation of the proof mass. An additional RIE step solves the problem. If the

plasma etching is optimized for the membrane thickness, the mode disturbance is prevented. Alternatively, the membranes can be etched before the bonding.

- The fabricated resonators acted as expected both by the analytical calculations and by the simulation models. However, the mechanical gain of the resonators are not sufficient to suppress the feedthrough current. In order to increase the output (sensing) current for real-time detection, the resonators should be redesigned to increase the current without worsening the damping effects. Damping increases with the thickness of the hydrophobic parylene between the resonator gaps. On the other hand, thinner parylene intermediate layers may decrease the bonding quality.

- Liquid flow tests through the microfluidic channels prove that the bonding withstands to liquid flow and there are no leakages observed around the bonding interfaces. In addition, parylene really prevents leakage through the resonator gaps. However, because of the increased feedthrough when there is a liquid inside the microfluidic channel, the sensing current cannot be detected by using methods based on the fundamental tones. Either the second harmonic characterization could be used to suppress the feedthrough or the resonators could be redesigned to decrease the coupling between electrodes and to increase the mechanical current.

Related future work on the topic can be summarized as:

- In order to increase the bonding quality, microwave heating of the polymer during the thermal bonding could be performed. This method has been reported in [45]; however, there was no suitable wafer bonding system to experimentally test the technique. If it is possible to modify an available wafer bonding system for the technique, it could increase the bonding quality in terms of strength and yield.

- The membrane etching could be performed before the bonding. By doing so, the additional parylene RIE could be eliminated. However, a shorter wavelength UV exposure may be necessary for the lithography because it is

82

challenging to align the masks and to develop the photoresists around the narrow resonator gaps. The development of the photoresist should be optimized carefully because etch-rates for the deep trenches would decrease due to the decreased substrate (attack) area.

- The mechanical current gain could be enhanced by modifying the resonator designs. Thicker substrates and comb drives increase the capacitance between the proof mass, and actuation and sensing electrodes. However, the thicker the resonators are, the more the oscillation is suppressed by the damping forces. In addition, comb drives increase the squeeze film damping. Hence, a great care should be taken designing the resonators.

- In order for real time detection, the resonators should operate under a liquid flow. To balance the micro-channel fluidic resistances around the resonator gaps, air-trapping method can be used as proposed in [14]. PDMS caps can be utilized. Alternatively, parylene micro-caps could be transferred using parylene micro-molding method based on thermal bonding of parylene [68].

- The second harmonic characterization method could be used to suppress the feedthrough current. Although this method eliminates the feedthrough current in the fundamental tone at the sensing (output) electrode, additional feedthrough from the interface electronics should also be eliminated by careful IC/PCB design.

- Bio-activation protocols should be used to activate the metal surface on the proof mass to selectively catch and immobilize the circulating tumor cells. Real-time quantification of the target cells is possible if the resonators can be characterized when there is a liquid inside the microfluidic channel. Notice that, the cell binding would introduce an additional nonlinear damping to the micromechanical system.

- By using the proposed fabrication method, other MEMS devices such as microfluidic mixers and micro-valves can be fabricated. In addition, as shown in this thesis, fabrication of freestanding membranes is also possible.

- The proposed fabrication method could enable newer applications. The restoration of the shear deformation could be analyzed. A shear force that is smaller than the breakage force could be applied similarly as in bonding tests for a period of time and the displacement could be tracked. The flexibility and restoration could open new ways for nano/micro assembly and MEMS packaging applications.

REFERENCES

[1] I. Bars and J. Terning, *Extra Dimensions in Space and Time*. Springer Science & Business Media, 2009.

[2] "Earth Fact Sheet." [Online]. Available: https://nssdc.gsfc.nasa.gov/planetary/factsheet/earthfact.html. [Accessed: 24-Jul-2017].

[3] "Tallest man - living | Guinness World Records." [Online]. Available: http://www.guinnessworldrecords.com/world-records/tallest-man-living. [Accessed: 24-Jul-2017].

[4] M. L. Turgeon, *Clinical Hematology: Theory and Procedures*. Lippincott Williams & Wilkins, 2005.

[5] "Planck length in m - Wolfram|Alpha Results." [Online]. Available: http://m.wolframalpha.com/input/?i=Planck+length+in+m. [Accessed: 24-Jul-2017].

[6] R. P. Feynman, "The value of science," *Engineering and Science*, vol. 19, no. 3, pp. 13–15, 1955.

[7] "Status of the MEMS Industry 2017," *i-micronews*. [Online]. Available: https://www.i-micronews.com/report/product/the-status-of-the-mems-industry-2017.html. [Accessed: 24-Jul-2017].

[8] A. Folch, *Introduction to BioMEMS*. CRC Press, 2016.

[9] P. Potdar and N. Lotey, "Role of circulating tumor cells in future diagnosis and therapy of cancer," *Journal of Cancer Metastasis and Treatment*, vol. 1, no. 2, p. 44, 2015.

[10] K. Pantel, R. J. Cote, and Ø. Fodstad, "Detection and Clinical Importance of Micrometastatic Disease," *J Natl Cancer Inst*, vol. 91, no. 13, pp. 1113–1124, Jul. 1999.

[11] P. Mehlen and A. Puisieux, "Metastasis: a question of life or death," *Nat Rev Cancer*, vol. 6, no. 6, pp. 449–458, Jun. 2006.

[12] D. Wirtz, K. Konstantopoulos, and P. C. Searson, "The physics of cancer: the role of physical interactions and mechanical forces in metastasis," *Nat Rev Cancer*, vol. 11, no. 7, pp. 512–522, Jun. 2011.

[13] M. T. Gabriel, L. R. Calleja, A. Chalopin, B. Ory, and D. Heymann, "Circulating Tumor Cells: A Review of Non–EpCAM-Based Approaches for Cell Enrichment and Isolation," *Clinical Chemistry*, vol. 62, no. 4, pp. 571–581, Apr. 2016.

[14] A. T. Çiftlik, "Design and Implementation of a Dielectrophoretic Separator and a Gravimetric Detector for MEMS Based Cytometry Applications," M.S. thesis, Middle East Technical University, Ankara, Turkey, 2008.

[15] M. Brown and C. Wittwer, "Flow Cytometry: Principles and Clinical Applications in Hematology," *Clinical Chemistry*, vol. 46, no. 8, pp. 1221–1229, Aug. 2000.

[16] "Types of Luminescence." [Online]. Available: https://www.tf.uni-kiel.de/matwis/amat/admat_en/kap_5/advanced/t5_2_4.html. [Accessed: 24-Jul-2017].

[17] Z. Altintas, *Biosensors and Nanotechnology: Applications in Health Care Diagnostics*. Wiley, 2018.

[18] E. Engvall and P. Perlmann, "Enzyme-Linked Immunosorbent Assay, Elisa," *The Journal of Immunology*, vol. 109, no. 1, pp. 129–135, Jul. 1972.

[19] "Epithelial Cell Adhesion Molecule: More than a Carcinoma Marker and Adhesion Molecule - ScienceDirect." [Online]. Available: http://www.sciencedirect.com/science/article/pii/S0002944010619724#bib6. [Accessed: 24-Jul-2017].

[20] R. Bashir, "BioMEMS: state-of-the-art in detection, opportunities and prospects," *Advanced Drug Delivery Reviews*, vol. 56, no. 11, pp. 1565–1586, Sep. 2004.

[21] M. M. G. Grafton, T. Maleki, M. D. Zordan, L. M. Reece, R. Byrnes, A. Jones, P. Todd, J. F. Leary, "Microfluidic MEMS hand-held flow cytometer," presented at the Microfluidics, BioMEMS, and Medical Microsystems IX, 2011, vol. 7929, p. 79290C–79290C–10.

[22] A. Ozcan and E. McLeod, "Lensless Imaging and Sensing," *Annual Review of Biomedical Engineering*, vol. 18, no. 1, pp. 77–102, 2016.

[23] A. Ozcan and U. Demirci, "Ultra wide-field lens-free monitoring of cells on-chip," *Lab Chip*, vol. 8, no. 1, pp. 98–106, Dec. 2007.

[24] W. H. Coulter and W. R. Hogg, Apparatus and method for measuring a dividing particle size of a particulate system. Google Patents, 1971.

[25] R. Liu, W. Waheed, N. Wang, O. Civelekoglu, M. Boya, C. Chu, A. F. Sarioglu, "Design and modeling of electrode networks for code-division multiplexed resistive pulse sensing in microfluidic devices," Lab on a Chip, 2017.

[26] G. Vona, A. Sabile, M. Louha, V. Sitruk, S. Romana, K. Schütze, F. Capron, D. Franco, M. Pazzagli, M. Vekemans, B. Lacour, C. Brechot, P. Paterlini-Brechot, "Isolation by size of epithelial tumor cells : a new method for the immunomorphological and molecular characterization of circulatingtumor cells," Am. J. Pathol., vol. 156, no. 1, pp. 57–63, Jan. 2000.

[27] S. Nagrath, L. V. Sequist, S. Maheswaran, D. W. Bell, D. Irimia, M. R. Smith, E. L. Kwak, S. Digumarthy, A. Muzikansky "Isolation of rare circulating tumour cells in cancer patients by microchip technology," Nature, vol. 450, no. 7173, pp. 1235–1239, Dec. 2007.

[28] S. Subhashini and A. V. Juliet, "CO_2 Gas Sensor Using Resonant Frequency Changes in Micro-Cantilever," in Computer Networks & Communications (NetCom), Springer, New York, NY, 2013, pp. 75–80.

[29] A. Gupta, D. Akin, and R. Bashir, "Single virus particle mass detection using microresonators with nanoscale thickness," Appl. Phys. Lett., vol. 84, no. 11, pp. 1976–1978, Mar. 2004.

[30] T. P. Burg, M. Godin, S. M. Knudsen, W. Shen, G. Carlson, J. S. Foster, K. Babcock, S. R. Manalis, "Weighing of biomolecules, single cells and single nanoparticles in fluid," Nature, vol. 446, no. 7139, pp. 1066–1069, Apr. 2007.

[31] E. Aydın, M. Kangül, F. Gökçe, Ö. Zorlu, and H. Külah, "A novel characterization method for MEMS based electrostatic resonators for Q enhancement and feedthrough current elimination," in 2016 IEEE SENSORS, 2016, pp. 1–3.

[32] M. Kangül, E. Aydın, F. Gökçe, T. Toral, O. Zorlu, and H. Külah, "Design of a Resonator-on-Microchannel (RoM) for Gravimetric Detection Applications in Liquid Environment," Procedia Engineering, vol. 168, pp. 506 – 509, 2016.

[33] E. Bayraktar, D. Eroglu, A. T. Ciftlik, and H. Kulah, "A MEMS based gravimetric resonator for mass sensing applications," in 2011 IEEE 24th International Conference on Micro Electro Mechanical Systems (MEMS), 2011, pp. 817–820.

[34] D. Eroglu and H. Kulah, "Quality Factor Enhancement of Lateral Microresonators in Liquid Media by Hydrophobic Coating," Journal of Microelectromechanical Systems, vol. 20, no. 5, pp. 1068–1070, Oct. 2011.

[35] S. Sang, Y. Zhao, W. Zhang, P. Li, J. Hu, and G. Li, "Surface stress-based biosensors," Biosensors and Bioelectronics, vol. 51, pp. 124 – 135, 2014.

[36] J. Lee, W. Shen, K. Payer, T. P. Burg, and S. R. Manalis, "Toward Attogram Mass Measurements in Solution with Suspended Nanochannel Resonators," Nano Lett., vol. 10, no. 7, pp. 2537–2542, Jul. 2010.

[37] S. Olcum, N. Cermak, S. C. Wasserman, K. S. Christine, H. Atsumi, K. R. Payer, W. Shen, J. Lee, A. M. Belcher, S. N. Bhatia, S. R. Manalis "Weighing nanoparticles in solution at the attogram scale," PNAS, vol. 111, no. 4, pp. 1310–1315, Jan. 2014.

[38] M. Kangül, "MEMS Based Resonant Mass Sensors with Feedthrough Current Elimination for In-Liquid Cell Detection Applications," M.S. thesis, Middle East Technical University, Ankara, Turkey, 2015.

[39] H. Yu, Y. Chen, P. Xu, T. Xu, Y. Bao, and X. Li, "μ-'diving suit' for liquid-phase high-Q resonant detection," *Lab Chip*, 2016.

[40] E. Bayraktar, "Design and Implementation of a MEMS Based Gravimetric Detector for Cytometry Applications," M.S. thesis, Middle East Technical University, Ankara, Turkey, 2010.

[41] D. Eroğlu, "Development of a Resonant Mass Sensor for MEMS Based Cell Detection Applications," M.S. thesis, Middle East Technical University, Ankara, Turkey, 2012.

[42] T. B. Töral, "Development of a High Yield Fabrication Process for MEMS Based Resonant Mass Sensors for Cell Detection Applications," M.S. thesis, Middle East Technical University, Ankara, Turkey, 2014.

[43] H. S. Kim and K. Najafi, "Wafer bonding using parylene and wafer-level transfer of free-standing parylene membranes," in *TRANSDUCERS, Solid-State Sensors, Actuators and Microsystems, 12th International Conference on, 2003*, 2003, vol. 1, pp. 790–793 vol.1.

[44] H. Kim and K. Najafi, "Characterization of low-temperature wafer bonding using thin-film parylene," *Journal of Microelectromechanical Systems*, vol. 14, no. 6, pp. 1347–1355, Dec. 2005.

[45] H. Noh, K. Moon, A. Cannon, P. J. Hesketh, and C. P. Wong, "Wafer bonding using microwave heating of parylene intermediate layers," *J. Micromech. Microeng.*, vol. 14, no. 4, p. 625, 2004.

[46] D. P. Poenar, C. Iliescu, M. Carp, A. J. Pang, and K. J. Leck, "Glass-based microfluidic device fabricated by parylene wafer-to-wafer bonding for impedance spectroscopy," *Sensors and Actuators A: Physical*, vol. 139, no. 1–2, pp. 162–171, Sep. 2007.

[47] Q. Shu, X. Huang, Y. Wang, and J. Chen, "Wafer bonding with intermediate Parylene layer," in *9th International Conference on Solid-State and Integrated-Circuit Technology, 2008. ICSICT 2008*, 2008, pp. 2428–2431.

[48] A. T. Ciftlik and M. A. M. Gijs, "Low temperature Pyrex/silicon wafer bonding via a single intermediate parylene layer," in *Solid-State Sensors, Actuators and Microsystems Conference (TRANSDUCERS), 2011 16th International*, 2011, pp. 366–369.

[49] F. Gökçe, E. Aydın, M. Kangül, T. B. Töral, Ö. Zorlu, Ö. Şardan-Sukas, H. Külah "A parylene bonding based fabrication method for gravimetric resonant based MASS sensors," in *2017 19th International Conference on Solid-State Sensors, Actuators and Microsystems (TRANSDUCERS)*, 2017, pp. 1195–1198.

[50] "PARA TECH: Parylene Properties for Parylene C, N, D Variants." [Online]. Available: http://www.parylene.com/specifications-properties.php. [Accessed: 04-Aug-2017].

[51] A. T.-H. Lin, J. Yan, and A. A. Seshia, "Dynamic response of water droplet coated silicon MEMS resonators," in *Ultrasonics Symposium (IUS), 2009 IEEE International*, 2009, pp. 669–672.

[52] O. Brand, I. Dufour, S. Heinrich, and F. Josse, *Resonant MEMS: Fundamentals, Implementation, and Application*. John Wiley & Sons, 2015.

[53] X. Zhang and W. C. Tang, "Viscous air damping in laterally driven microresonators," in Proceedings IEEE Micro Electro Mechanical Systems An Investigation of Micro Structures, Sensors, Actuators, Machines and Robotic Systems, 1994, pp. 199–204.

[54] W. Ye, X. Wang, W. Hemmert, D. Freeman, and J. White, "Air damping in laterally oscillating microresonators: a numerical and experimental study," *Journal of Microelectromechanical Systems*, vol. 12, no. 5, pp. 557–566, Oct. 2003.

[55] W.-C. Chuang, H.-L. Lee, P.-Z. Chang, and Y.-C. Hu, "Review on the Modeling of Electrostatic MEMS," *Sensors*, vol. 10, no. 6, pp. 6149–6171, Jun. 2010.

[56] M. Gologanu, C. G. Bostan, V. Avramescu, and O. Buiu, "Damping effects in MEMS resonators," in *Semiconductor Conference (CAS), 2012 International*, 2012, vol. 1, pp. 67–76.

[57] T. R. Albrecht, P. Grütter, D. Horne, and D. Rugar, "Frequency modulation detection using high- Q cantilevers for enhanced force microscope sensitivity," *Journal of Applied Physics*, vol. 69, no. 2, pp. 668–673, Jan. 1991.

[58] M. Bao, Analysis and Design Principles of MEMS Devices. Elsevier, 2005.

[59] G. Wallis and D. I. Pomerantz, "Field Assisted Glass- Metal Sealing," *Journal of Applied Physics*, vol. 40, no. 10, pp. 3946–3949, Sep. 1969.

[60] Daniel I Pomerantz, *Anodic bonding*. Google Patents, 1965.

[61] T. R. Anthony, "Anodic bonding of imperfect surfaces," *Journal of Applied Physics*, vol. 54, no. 5, pp. 2419–2428, May 1983.

[62] W. F. Gorham, "A New, General Synthetic Method for the Preparation of Linear Poly-p-xylylenes," *J. Polym. Sci. A-1 Polym. Chem.*, vol. 4, no. 12, pp. 3027–3039, Dec. 1966.

[63] R. P. von Metzen and T. Stieglitz, "The effects of annealing on mechanical, chemical, and physical properties and structural stability of Parylene C," *Biomed Microdevices*, vol. 15, no. 5, pp. 727–735, Oct. 2013.

[64] L. Wei, P. Parhi, E. A. Vogler, T. M. Ritty, and A. Lakhtakia, "Thickness-controlled hydrophobicity of fibrous Parylene-C films," *Materials Letters*, vol. 64, no. 9, pp. 1063–1065, May 2010.

[65] T. Trantidou, T. Prodromakis, and C. Toumazou, "Oxygen plasma induced hydrophilicity of Parylene-C thin films," *Applied Surface Science*, vol. 261, pp. 43–51, Nov. 2012.

[66] Y. Temiz, C. Guiducci, and Y. Leblebici, "Post-CMOS Processing and 3-D Integration Based on Dry-Film Lithography," *IEEE Transactions on Components, Packaging and Manufacturing Technology*, vol. 3, no. 9, pp. 1458–1466, Sep. 2013.

[67] M. Kangül, E. Aydin, F. Gökçe, Ö. Zorlu, and H. Külah, "Analysis and Elimination of the Capacitive Feedthrough Current on Electrostatically Actuated and Sensed Resonance-Based MEMS Sensors," *Journal of Microelectromechanical Systems*, vol. PP, no. 99, pp. 1–7, 2017.

[68] H. Noh, K. Moon, A. Cannon, P. J. Hesketh, and C. P. Wong, "Wafer bonding using microwave heating of parylene intermediate layers," *J. Micromech. Microeng.*, vol. 14, no. 4, p. 625, 2004.

APPENDIX A

SERIAL CAPACITANCE MEASUREMENTS ON A PLANAR DEP ELECTRODE TO UNDERSTAND THE EFFECTS OF THERMAL BONDING ON PARYLENE DIELECTRIC PROPERTIES

In order to understand whether dielectric performance of Parylene-C intermediate layer is affected from the thermal bonding process, a DEP chip was used. The DEP chip has planar interdigitated electrodes under a thin parylene isolation layer (~0.5 µm). The particles or cells flow through a parylene microfluidic channel on the electrodes, where they face a DEP force caused by the fringing electric field between the planar electrodes. The schematic illustration of the DEP chip and the optical microscope image of the electrodes are given in Figure A.1.
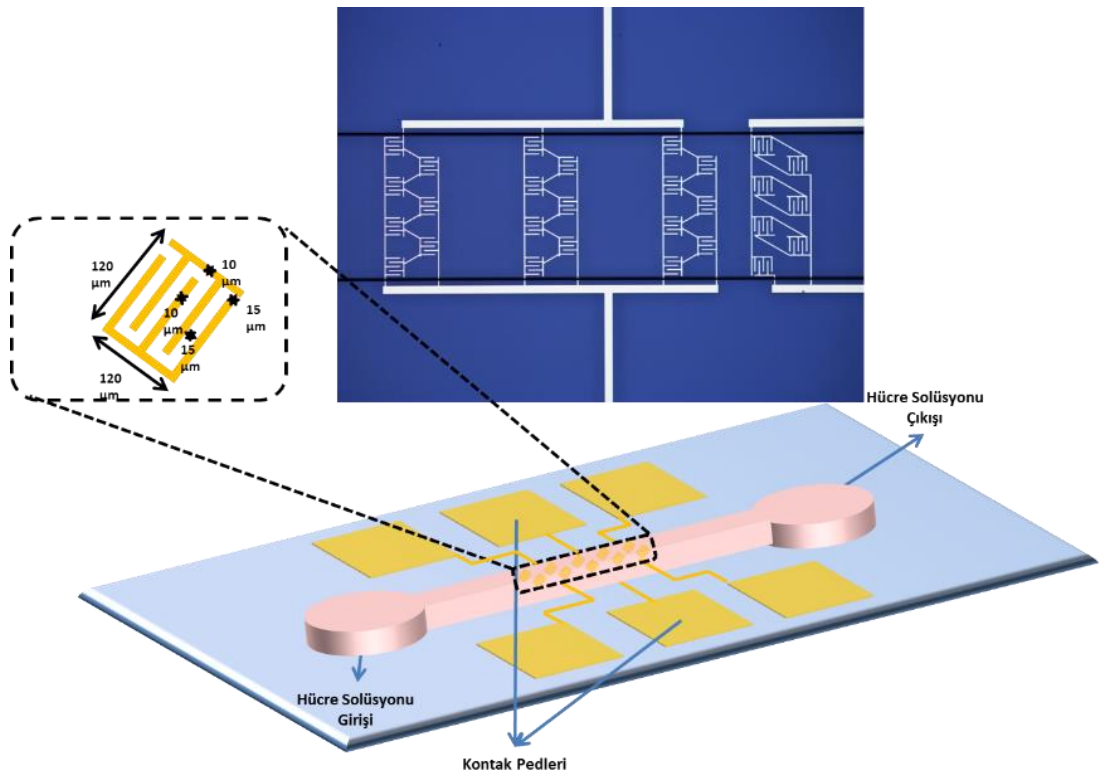

Figure A.1 The illustration of the DEP chip and the optical microscope image of the DEP electrodes.

The serial capacitance of one of the DEP electrodes were measured before and after replicating the thermal steps of the bonding process. First, the test chip was taped and wire-bonded to a ceramic package in order to eliminate the feedthrough capacitances caused by cabling. Then, the package was annealed at 200ºC for 75 minutes, which is very similar to the thermal steps of a parylene-bonding recipe. After the chip cooled down to the room temperature, the serial capacitance was measured by using an Agilent E4980 LCR Meter. In order to minimize the parasitic effects, a PCB and BNC connectors were used. Both short circuit and open circuit corrections were made during the measurements. The LCR measurement setup is shown in Figure A.2.
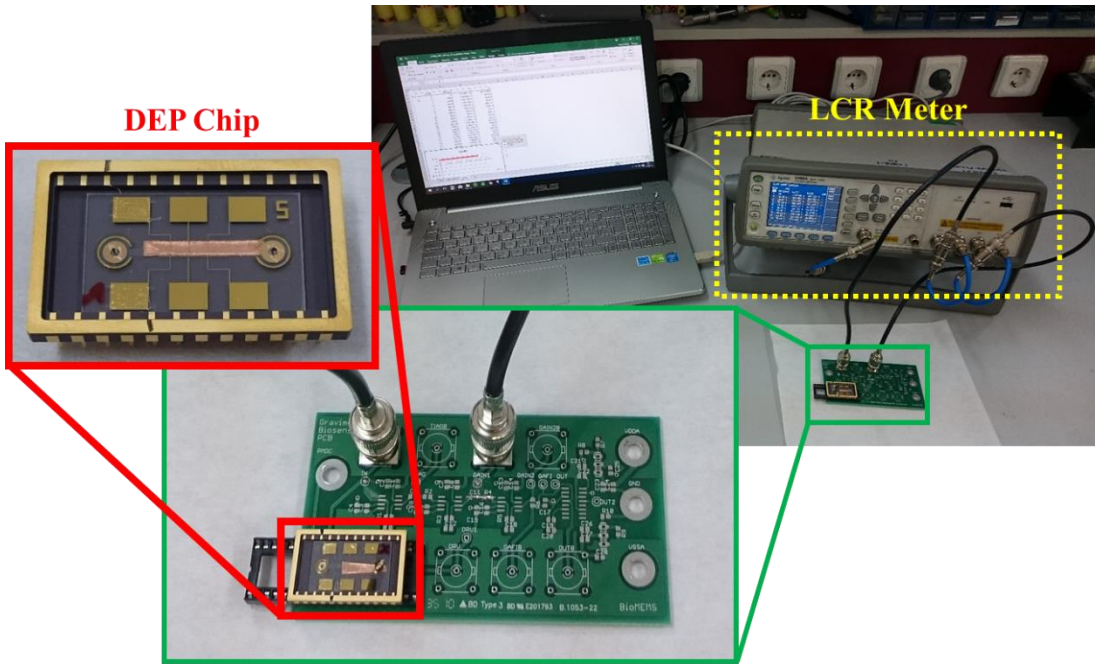

Figure A.2 The measurement setup, PCB with BNC connections and DEP chip taped on a ceramic package.

The serial capacitance between the planar DEP electrodes were measured for a frequency range between 200 Hz and 2 MHz, for both before and after the annealing. The measurements are given in Figure 4.3, in Chapter 4. Although there is a small difference around lower frequencies, the measured capacitance after the annealing follows a similar trend with the initial measurements. The measurements are almost the same before and after the annealing, implying that the DEP performance would not be affected from the thermal changes during parylene bonding.

APPENDIX B

BONDING STRENGTH MEASUREMENTS OF BARE
SILICON-GLASS PARYLENE BONDING TRIALS

In order to measure the bonding strengths of the bare trials, the bonded wafers were diced as 25 mm^2 square dies. In order to measure the bonding strengths of the four bonding trials, wafers were diced into 25 mm^2 square dies. Using a Dage 4000 Multipurpose Bondtester, shear force was applied at an elevation corresponding to the top material's mid-thickness (650 µm). The force was increased gradually during the test until the wafers broke off. The applied force and the displacement of the Si on glass were recorded with respect to time. The applied shear force vs. time plots for each of the trials are given here.

Notice that, for each of the line graphs, the maximum force recorded just before the breakage was divided by the initial contact area; i.e. 25 mm^2, to calculate the shear bonding strength. However, because the silicon had been sliding over the glass with the applied force, the actual contact area was smaller than the initial area. Thus, the calculated bonding strength represents an engineered approximation.

Table B.1 The details of the bare silicon-glass bonding experiments.

Bonding Trial	Intermediate Layers	Thickness of Layers (µm)	Temperature (ºC)	Piston Force (N)
1st	double	1	150	1000
2nd	single	1	150	1000
3rd	double	1	200	2000
4th	single	1	200	2000
5th	single	0.5	200	2000
6th	single	0.5	250	2000

The details of the bare bonding experiments are given in Table B.1. Note that, for all the trials, the bonding chamber had been vacuumed down to 1 mTorr before the

heating started. The vacuum level had hit down to 0.1 mTorr during the bonding process as shown in Appendix C. Moreover, piston force had been applied for 1 hour for each of the trials.
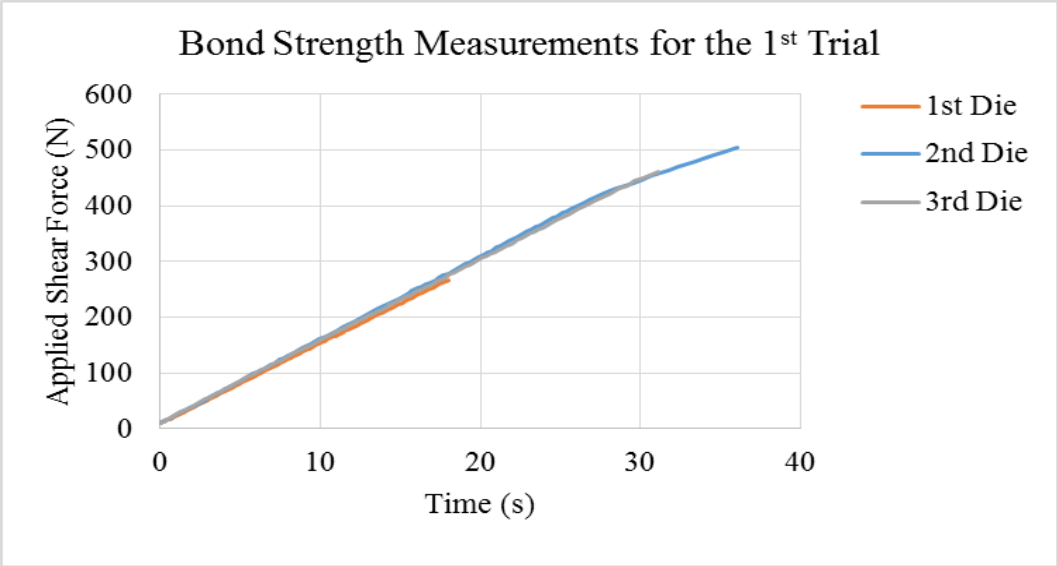

Bond Strength Measurements for the 1st Trial

Figure B.3 Applied shear force vs. time until the breakage for dies of the 1st bonding trial. Notice that the 1st die had broken earlier than the others. For the 3rd die, the slope decreases after ~30s. The maximum applied force just before the breakage of the dies for the 1st, 2nd and 3rd dies are 267 N, 503 N and 462 N respectively. Average shear strength was calculated as 16.4 MPa by arithmetic averaging.
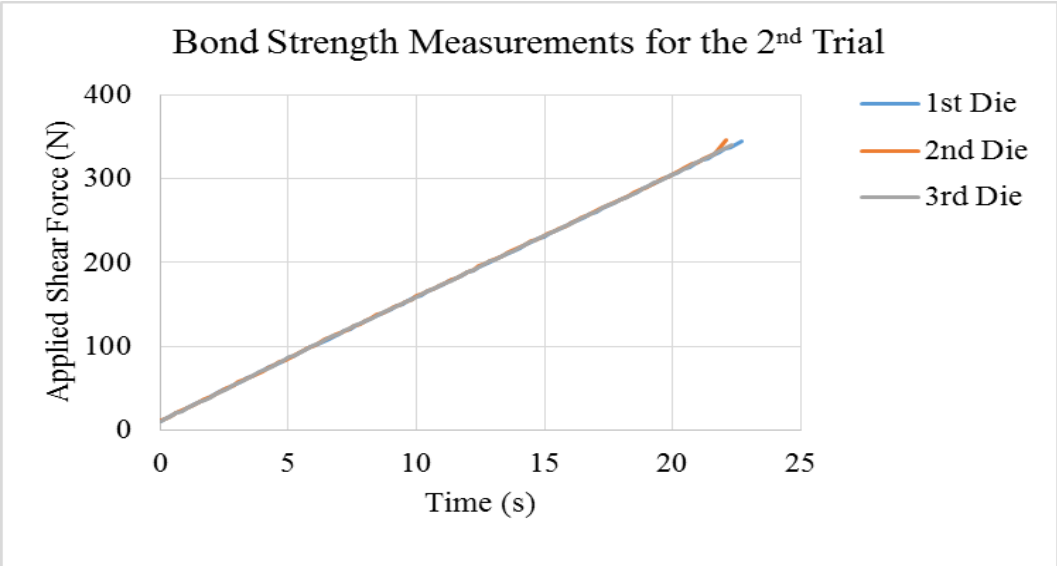

Bond Strength Measurements for the 2nd Trial

Figure B. 4 Applied shear force vs. time until the breakage for dies of the 2nd bonding trial. The maximum applied force just before the breakage of the dies for the 1st, 2nd and 3rd dies are 345 N, 347 N and 339 N respectively. Average shear strength was calculated as 13.75 MPa by arithmetic averaging.
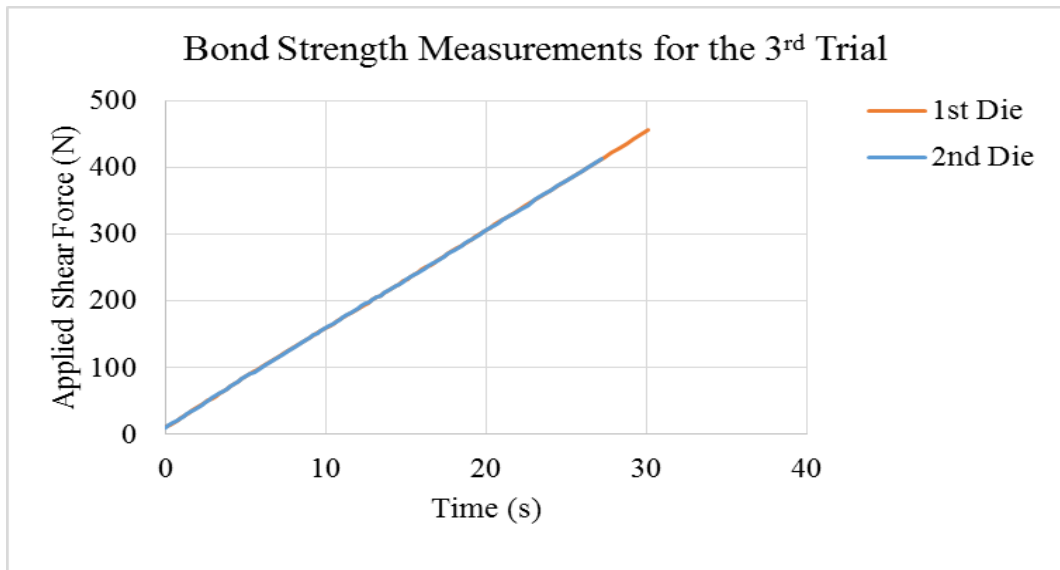
Figure B.5 Applied shear force vs. time until the breakage for dies of the 3rd bonding trial. The maximum applied force just before the breakage of the dies for the 1st and 2nd dies are 455 N and 413 N respectively. Average shear strength for the trial was calculated as 17.36 MPa by arithmetic averaging.

Figure B.6 Applied shear force vs. time until the breakage for dies of the 4th bonding trial. The maximum applied force just before the breakage of the dies for the 1st and 2nd dies are 450 N and 498 N respectively. Average shear strength for the trial was calculated as 18.97 MPa by arithmetic averaging.
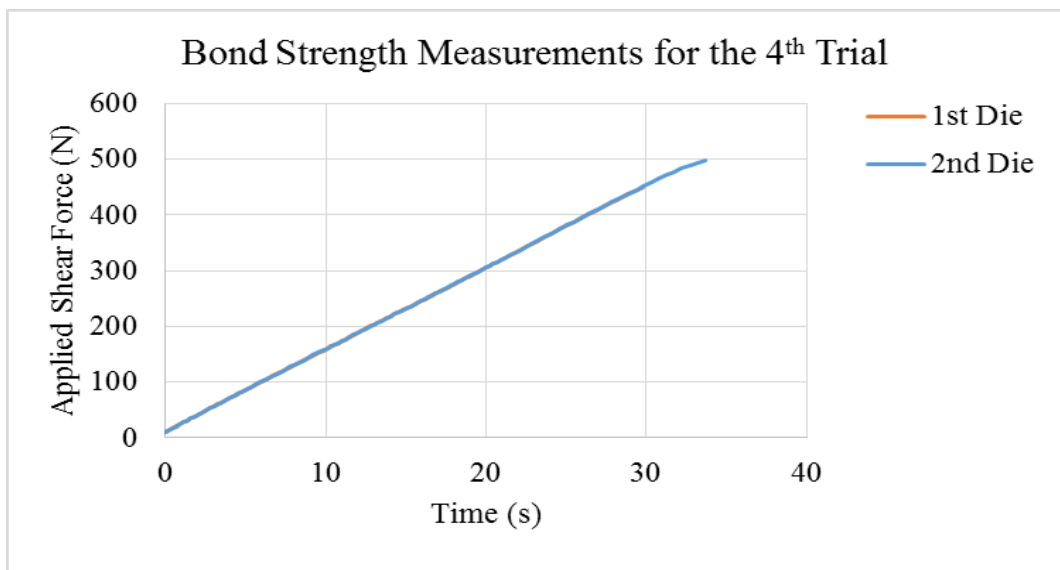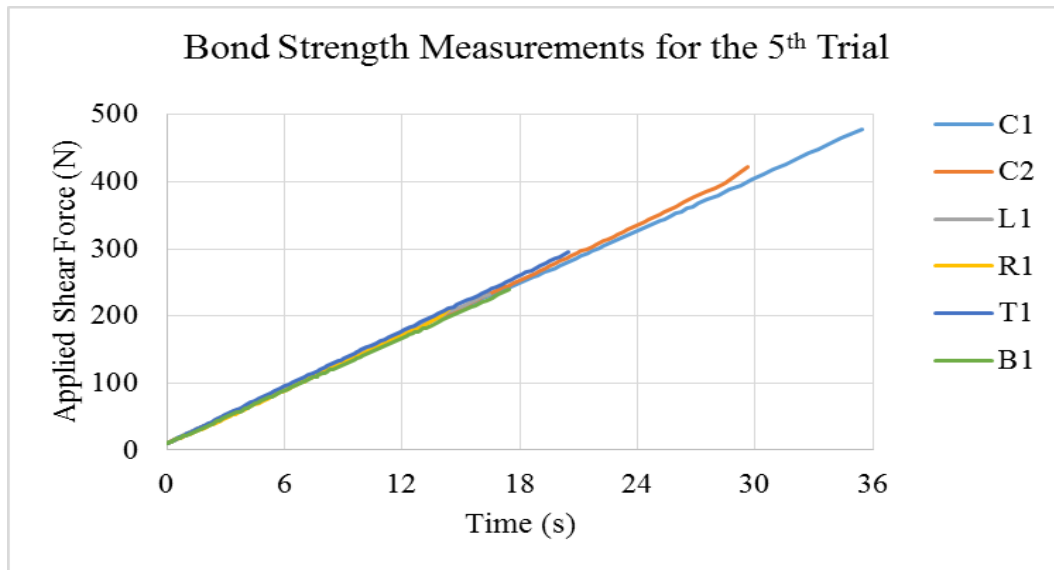
Figure B.7 Applied shear force vs. time until the breakage for dies of the 5th bonding trial. The maximum applied force just before the breakage of the dies for C1, C2, L1, R1, T1 and B1 are 479 N, 423 N, 231 N, 212 N, 295 N and 239 N respectively. Average shear strength for the trial was calculated as 12.53 MPa by arithmetic averaging.

The sixth trial, the measurements of which are plotted in Figure 4.6, had shown a strength distribution that is more uniform when compared with the others. Although still a bit weaker than the center, the outer regions of the wafer were also strong; meaning a wafer level quality of the bonding. In addition to these, the additional vacuuming steps between each step of the heating had eliminated the air bubbles during the bonding and increased the bonding yield. These were the main reasons why the bonding recipe of the sixth trial is preferred for the fabrication of the lateral gravimetric resonators.

The details of the bonding recipe is given in Appendix C.

APPENDIX C

DETAILS OF THE OPTIMIZED PARYLENE BONDING RECIPE

The detailed recipe of the optimized bonding recipe is given in Table C.2. The intermediate steps are not shown in the recipe. Note that, just before the bonding, the wafers should be cleaned and dehydrated. Then, the bonding surfaces should be activated using oxygen plasma. Finally, they should be aligned using a mask aligner. Also, notice that, the wafers are contact aligned for this bonding recipe.

Table C.2 The detailed bonding recipe for EVG501 Wafer Bonding System.

Step	Details	Value
Pump on	High vacuum	
Wait	Pressure	1.00E-03 Torr
Wait	Time	0:10:00
Heating		50 ºC
Wait	Time	0:05:00
Heating		100 ºC
Wait	Time	0:05:00
Heating		150 ºC
Wait	Time	0:05:00
Heating		200 ºC
Wait	Time	0:05:00
Heating		250 ºC
Wait	Time	0:30:00
Piston down		2000 N
Wait	Time	1:00:00
Piston up		
Cooling		50 ºC